Development and application of coupled THM solvers to estimate rock failure events from laboratory to field scales

Dissertation

zur

Erlangung des Doktorgrades (Dr. rer. nat.)

der

Mathematisch-Naturwissenschaftlichen Fakultät

der

Rheinischen Friedrich-Wilhelms-Universität Bonn

vorgelegt von

Thomas Heinze

aus

Gießen

Bonn 2014

Angefertigt mit Genehmigung der Mathematisch-Naturwissenschaftlichen Fakultät
der Rheinischen Friedrich-Wilhelms-Universität Bonn
am Steinmann-Institut für Geologie, Mineralogie und Paläontologie

1. Referent: Prof. Dr. Stephen A. Miller, University of Neuchatel, Swiss
2. Referent: Prof. Dr. Nikolaus Froitzheim, Universität Bonn

Tag der Promotion: 30.06.2015
Erscheinungsjahr: 2015

Abstract

In this thesis I present a theoretical and numerical model to simulate complex fluid-rock interactions with a poro- elasto- plastic rheology, multi- phase flow and heat transport (THM- model). Goal of this work is to improve existing approaches fundamentally by elaborating a better, dynamic rheological model as well as developing tools to improve the comparison between simulation and observations on field and laboratory scale.
This work contains the derivation and implementation of a two- surface plastic damage model, a method to detect a numerical analog for acoustic emissions in rock samples and a simulation of earthquake swarms in western bohemia. The developed damage model outnumbers existing approaches in terms of a realistic reproduction of experimental measurements and will be usefull for future simulations of drained and undrained rock deformations. Especially if the rock is subjected to cyclic load or pore pressure, damage effects are essential. In fluid- rock systems this can often be the case due to temporarily increasing and decreasing fluid pressure. Reoccurring, fluid-driven earthquake swarms and stimulation of geothermal fields with hydrofracturing are examples for this. Acoustic emissions (AE) and (micro-) seismic events contain important information on a very local range which can not be resolved by other measurement techniques. On the other hand, there is no physical property directly related to AE. In this work I present a straightforward mechanism to obtain a proxy for acoustic emissions during a numerical simulation which agrees very well with laboratory measurements. The same mechanism can be extended to field scale for detecting and localizing earthquakes. I present an application of this method to the 2008 earthquake swarm in West- Bohemia (Czech Republic). Using the developed method I am abel reproduce the localization, temporal evolution and magnitude distribution of the original earthquake catalog.
The projects examined in this thesis are suitable over a wide range of use cases. Industrial applications like geothermal energy or CO_2 sequestration can profit from presented methods and natural phenomena like earthquake swarms can be examined in more detail. Several aspects of this work are not even limited to geoscience and can be helpful in other subjects like material science and civil engineering. To validate and enable a reasonable usage of the theoretical model a numerical implementation is presented for all developed models.

Zusammenfassung

In dieser Arbeit präsentiere ich ein theoretisches und numerisches Model zur Beschreibung komplexer Wechselwirkungen zwischen Gestein und Flüssigkeiten. Ich verwende dabei eine poro- elasto- plastische Rheologie, Mehr- Phasen- Fluide und Wärmetransport (THM- Model). Ziel der Arbeit ist es existierende Modelle zu verbessern, indem ein vollständiges, dynamisches rheologisches Model ausgearbeitet wird und Methoden entwickelt werden, um einen besseren Vergleich zwischen Simulation und Feld- und Labormessungen zu ermöglichen.
Diese Arbeit beinhaltet die Herleitung eines plastischen Schadensmodel, eine Methode um ein numerisches Analogon für akustische Emissionen in Gesteinsproben zu finden und eine Simulation eines Erdbebenschwarms in West- Böhmen. Ein realistisches Schadensmodel is besonders dann von Bedeutung, wenn Belastungen zyklisch stattfinden. In Gesteins- Flüssigkeits Systemen kann das vorkommen durch ansteigenden und abnehmenden Fluiddruck. Etwa wiederkehrende, fluid- getriebene Erdbebenschwärme oder die Stimulation eines Gebietes durch Hydrofracturing sind Beispiele dafür. Akustische Emissionen (AE) und (mikro-) seismische Ereignisse geben Informationen über sehr lokale Spannungszustände, die durch andere Messungen nicht zugänglich sind. Gleichzeitig sind jedoch gerade AEs nicht direkt mit einer physikalischen Größe verknüpft. In dieser Arbeit entwickle ich eine Methode um eine physikalische und numerische Entsprechung für diese Emissionen zu finden. Mit Hilfe der gleichen Methode bin ich auch in der Lage die örtlich- zeitliche sowie die Magnituden- Entwicklung des 2008 Erdbebenschwarms in Böhmen zu reproduzieren. Die enwickelten Methoden haben eine Vielzahl an Anwendungen. Sowohl industrieler Art, etwa für geothermische Anlagen oder zur Speicherung von CO_2 im Untergrund, als auch zur Beschreibung natürlicher Erscheinungen wie Erdbebenschwärme. Einige Aspekte dieser Arbeit sind nicht auf die Geowissenschaften begrenzt, sondern können auch in verwandten Wissenschaften wie der Materialkunde oder dem Bauingenieurwesen Verwendung finden. Um die entwickelten Methoden zu testen und eine realistische Anwendung zu ermöglichen sind alle entwickelten Methoden in ein numerisches Model eingebettet.

Contents

Chapter 1

Motivation

Interactions between fluids and rocks play a crucial role at various natural phenomena like volcanic systems, mud volcanoes, earthquake swarms and aftershock sequences. For example experimental observations and an analytical model of the 1997 Umbria- Marche seismic sequence show that aftershocks can be triggered by intrusion of fluid pressure in a fault zone. A seal of inpermeable rock separates a high pressured,supercritical fluid source, from hydrostatic pressure above the seal. Breaking the seal leads to a propagating pressure pulse along the fault triggering aftershocks along its way (Miller et al. [2004]). At vulcanic activity the involvment of fluids is obvious. In 2006 the mud vulcano Lusi in North east Java errupted with mud and gas covering wide ranges (Mazzini et al. [2007]). Again field obersvations and physical models suggest that through fault slip deeply derived fluids intrude the fault and mix with an preexisting hydrothermal system feeding the eruption (Lupi et al. [2013]). Also driven by deeply derived fluids are earthquake swarms like for example in central europe in the Egger rift system (Fischer et al. [2014]) or the Matsushiro earthquake swarm in Japan (Cappa et al. [2009]). In both cases overpressured CO_2 arrises from the upwelling mantle, probably connected with magmatic activity, and intrude into a fault zone where they trigger earthquake swarms. Swarms are characterized by many events with small and middle sized magnitude without a main shock.

Due to the increasing demand of fuels in the last decade industrial applications utilizing hydrofracturing, which means breaking the rock by injecting high pressured fluids, brought new impulses into this field of research and opened it to the public. Hydrofracturing for shale gas recovery got a massive boost in the US, pilot projects of CO_2 sequestration started in Europe and geothermal power plants were installed all over the world, to name just some of recent applications. In these stimulation processes engineers increase the intrinsic permeability of the host rock by injecting high pressure fluid, mostly water or CO_2, through one or more boreholes up to a depth of 4 to 5 kilometers. Typical wellhead pressures can be up to 300 bars. The intrinsic permeability is normally very low, $k = 10^{-16}\ m^2$ or less, and the pores are not well enough connected for a decent fluid flow (Häring et al. [2008]). The high fluid pressure generates (micro-)fractures in the rock and increases permeability. In fractures the permeability can be higher by several magnitudes than the intrinsic

permeability of the intact host rock. Therefore fracture networks are the primary fluid flow channels. The geometry of fracture networks depends for example on heterogenities, anisotropy, stress state, loading history and can be very complex over various scales.

When (micro-) fractures are generated, seismic activity can be noticed and measured at the surface. In most cases the released energy is too small so it can not be noticed without scientific equipment. A high number of events with rather small amplitude can be observed while no clear main- and aftershock sequence can be identified (Häring et al. [2008]). At many industrial sites like the Deep Heat Mining Project in Basel, the Cooper Basin in Australia, the geothermal exploration site in Soultz-sous- Forets in France and in the Geysers in the USA, on the other hand higher seismic magnitudes than expected occurred. These events concerned residents and administrations as well as caused minor damage at buildings. Beside the forthright costs, a temporarly or permenent shut-down of the industrial production increased financial costs. This happened for example for a stimulated gas field in Oklahoma in 2011 (Holland [2011]) and the extraction site of shale gas in Lancashire/Blackpool in England where several earthquakes since April 2011 have occurred during hydro-fracturing (dePater and Baisch [2011]). Tectonic unstable regions have an increased risk for higher seismic energy release but also in regions with very few natural seismicity, earthquakes with a moment magnitude around 4 can be caused.

Many shale gas fields are located near to populated areas and for cost- efficient geothermal energy the power plant need to be close to the customer. A better understanding of the processes during fluid- rock interactions is needed to enable a save and reliable energy production for the future as well as to explain natural geodynamical phenomena.

Research in this field goes back to the 1940's with the initial work of Von Terzaghi, who showed experimentally that failur of a porous skeleton filled with fluid depends on the effective stress, which is the total stress minus the fluid pressure inside the pore space (von Terzaghi [1936]). This approach was found to be usefull predicting the failure of many types of soils and rocks. M.A. Biot generalized the theory and his equations build the basics for continuum poro- elasticity (Biot [1941]). Poro-elasticity describes the dilational response of rock due to increased pore pressure as well the draining of the rock during compression.

If a solid body is stressed above its elastic limit, which is called the yield point, the deformation becomes irreversible. It is also called plastic deformation. Common models to estimate the yield point are fore example given by Mohr- Coulomb or Drucker- Prager yield functions. Besides the stress state, plastic flow also depends on material properties like cohesion, angle of internal friction and angle of dilatancy. In enhanced models these values vary depending on the loading history. An popular example of such models are the cohesion weakening - frictional strengthening models (CWFS) which reduce cohesion and increase friction during plastic deformation (Hajiabdolmajid et al. [2002]). Plastic deformation is connected to generating (micro-) fractures in which the cohesion vanishes. On the other hand the friction increases with an increasing number of fractures. Generating voids also effects the elastic properties of the sceleton. This degradation of elastic properties is commonly

refered to as damage (Kachanov [1958]). Several approaches of different complexity exist in literature to estimate the degradation effect. Many input is coming from enigneering applications as damage is especially obvious for complex loading histories involving changes between dilation and compression.

Often the fluid involved has a different temperature than the rock. In industrial applications mainly cold fluid is induced in a hot host rock. In geothermal systems water of around 20°C is induced in a reservoir with a rock temperature of around 180°C (Häring et al. [2008]). Supercritical CO_2 emerging from the mantle on the other hand is significantly hotter than the rock of the crust. Rock and fluid expand with heat and contract by decreasing temperature. If they can not deform freely additional stresses are add to the preexisting stresses. In a first approach this can be covered by a thermo- elastic model (Tian [2013]).

As more complex the model becomes, analytical solutions can not be obtained anymore. Therefore computer models are utilized to gain realistic forecasts and a depper understanding of real world phenomena and applications. Since the 1990's various computer programms exist to simulate fluid-rock interactions. Many of the early programms are retired and were not adopted to modern computer architectures. There also exist various small internal simulation tools of several academic working groups. Most cited is the simulation framework FLAC which is developed and maintained by the Itasca consulting group, Inc. (Itasca consulting group [2012]). It covers elastic and plastic deformation of geo-materials, focussing on engineering mechanics. It is utilizing finite differences and an explicit scheme to calculate solutions for various problems and covering many popular theoretical models. More advanced features like thermal stresses and fluid dynamics are available through extra packages. It offers a wide range of adjustments its own command language. Due to its comerical character the source code is not available and an analyze of its calculations is therefore not possible. Also any optimisation like parallel computation or personal adjustments are not possible. FLAC can be coupled with TOUGH, which is a library including functions and equations of state for multi-phase, multicomponent fluid flow, including transport of media, density flow and heat (Rutqvist et al. [2002]). Other libraries focussing on fluid and transport flow are SHEMAT (Simulator for HEat and MAss Transport) and Pflotran (Clauser [2003], Lichtner et al. [2013]).

A different approach is taken by CSMP++, a finite element platform to simulate physical processes in environments with a complex geometry (Matthäi et al. [2007]). It is freely available as a binary, access to the source code is possible with agreement of the ETH Zürich. While CSMP includes various complex physical and numerical approaches, it is a rather complex tool with backdraws in spatial resolution and time necessary for computation. Remeshing and other numerical tools enable high spatial resolution in the region of interest but also increase the need of computational power. It is therefore less common outside of its developing institutes.

Also still active in development and very broad in its included features is OpenGeosys (Kolditz et al. [2012]). It includes a graphical user interface for pre- and postprocessing and is also freely available. It is developed and maintained by various german and international universities and institutions. Newest developments focus

on fluid flow and chemical reactions between rock and fluid but it also contains advanced mechanical models. Overall it is a feature rich, complex finite- element program, which is also rather demanding in its computational power. The code SLIM3D is also based on finite elements but utilizes a visco- elasto- plastic rheology (Popov and Sobolev [2008]). This enables the simulator to solve for lithospheric deformations or plume rising problems as well. On the other hand, it fells short in brittle mechanics as shear bands can only be generated by introducing initial weak zones.

In this thesis I develop a theoretical and numerical model to simulate the deformation of rock in response to loading and pore pressure over various scales with an advanced rheological model. One phase as well as multiphase fluid flow is considered, depending on the problem. Also heat transfer can be calculated as well as deformation and stress it causes. The final model includes therfore thermal, pressure and mechanics (THM- model). The model is capable to calculate dynamic fracture generation and fracture growth as well as non-linear behavior in rock and fluid flow. From the numerical side I use a staggered finite difference grid and an explicit time solution for the dynamics. The simulator is enabled for parallel computing to secure short computational times while using a high spatial and temporal resolution. Results are compared to experimental or field observations.

This thesis is organized in five chapters. In the first chapter I give a brief introduction in the theoretical and numerical background and a summuray of the scientific articles. In the second chapter an advanced damage model is introduced which utilizes a two- surface approach for the yield- and damage function. Special attention is paid to the numerical implementation and algorithmic structure. The following third chapter introduces a method to determine and locate acoustic emissions inside a specimen. Hydrofracturing on laboratory scale is considered and numerical results are compared with experimental data. In the fourth chapter the earthquake swarm sequences of 2008 along the Eger rift fault plane are simulated by adapting the algorithm developed in chapter three to field scale. The last chapter presents conclusion of this thesis and an outlook towards future research possibilities.

This cumulative thesis is organized as a series of papers submitted to international journals. Each one of the chapters two to four is a complete article. As a result of this structure, there is some repetition of the physical model and the used methods. The papers included in this thesis are a further development of the basic physical and numerical model I developed as part of my masters degree at the University of Bonn (Germany) in 2012. The main results of my master thesis are summarized in a scientific article as well and a copy of this submitted scientific paper is provided in the appendix.

1.1 Theoretical Background

The mechanics of rock and soil can be adopted from general solid mechanics. In this section I present basic theories and equations utilized in further parts of this thesis. The aim of this work is the simulation of rock and fluid behavior. Nevertheless many of the presented and developed models are not limited to this application.
The behavior of material under load is divided into different stages. The linear elasticity model based on Hooke's law is the most simple approach to describe reversible deformation. For porous media von Terzaghi's effective stress hypothesis and the model developed by Biot are the equivalent governing equations. Thermal contraction and expansion can also lead to elastic stresses. Beyond the elastic domain, plastic deformation starts. Based on the perfect plastic model more realistic results can be obtained including hardening- softening and damage behavior. Heat and fluid flow are no key aspects of this work but included in the final model. Therefore a short explanation will be provided as well. Further details on the basic rheological models can be found in Jaeger et al. [2007] and Davis and Selvadurai [2002].

1.1.1 Poro-elasto-plastic Model

1.1.1.1 Poro-elasticity

In solid body mechanics it is more common to use stresses than forces. Stress σ is defined as force acting over an area. Normal stresses σ_{ii} perpendicular to the area are separated from tangential shear stresses σ_{ij}. In this work stresses are assembled in the Cauchy stress tensor, which is symmetric. The cartesian coordinate system can be rotated towards the principal stresses σ_k with $k = 1, 2, 3$. In principal directions shear stresses vanish and only the three principal stresses remain normal to each other. Due to rotation the trace does not change, therefore

$$I_1 = \sigma_1 + \sigma_2 + \sigma_3 = \sigma_{xx} + \sigma_{yy} + \sigma_{zz} \tag{1.1}$$

which is the first invariant of the tensor. Using $\sigma' = \sigma - \frac{1}{3}\delta_{ij} I_1$, the deviatoric stress σ' is defined as the part of the stress which is not connected to volume change. Further invariants of the stress tensor can be defined in cartesian as well as principal directions,
Based on Newton's second law it can be derived for a two- dimensional solid body in $x-$ and $y-$ direction:

$$\begin{aligned} \frac{\partial v_x}{\partial t} &= \frac{1}{\rho} \cdot \left(\frac{\partial \sigma_{xx}}{\partial x} + \frac{\partial \sigma_{xy}}{\partial y} \right) \\ \frac{\partial v_y}{\partial t} &= \frac{1}{\rho} \cdot \left(\frac{\partial \sigma_{xy}}{\partial x} + \frac{\partial \sigma_{yy}}{\partial y} + \rho g \right) \end{aligned} \tag{1.2}$$

where ρ is rock density, v is displacement, g gravitational acceleration and t time.
Following the definition of the stress tensor the symmetric infinitesimal strain tensor ϵ is defined with displacement u:

$$\epsilon_{ij} = \frac{1}{2} \cdot \left(\frac{\partial u_i(\vec{x},t)}{\partial x_j} + \frac{\partial u_j(\vec{x},t)}{\partial x_i} \right) \tag{1.3}$$

The relationship between stress and strain is given by Hooke's law $\sigma_{ij} = E_{ijkl} \cdot \epsilon_{kl}$ with the elasticity tensor E which depends on the elastic properties, for example the first Lame constant λ and shear modulus G. The time derivative of Hooke's law gives the governing equations for elastic deformation:

$$\begin{aligned} \frac{\partial \sigma_{xx}}{\partial t} &= (\lambda + 2G) \cdot \frac{\partial v_x}{\partial x} + \lambda \cdot \frac{\partial v_y}{\partial y} \\ \frac{\partial \sigma_{yy}}{\partial t} &= (\lambda + 2G) \cdot \frac{\partial v_y}{\partial y} + \lambda \cdot \frac{\partial v_x}{\partial x} \\ \frac{\partial \sigma_{xy}}{\partial t} &= G \cdot \left(\frac{\partial v_x}{\partial y} + \frac{\partial v_y}{\partial x} \right) \end{aligned} \tag{1.4}$$

Von Terzaghi defined effective stresses as (von Terzaghi [1936]):

$$\sigma_{tot,ij} = \sigma_{eff,ij} + \alpha \cdot p\delta_{ij} \tag{1.5}$$

where p is pore pressure, the Kronecker Delta and α is the Biot coefficient, which is usually around 0.8 for porous rock. All derivations above are therefore valid for porous rocks if total stresses are used. Notice that pore pressure only acts along normal directions.
Considering fluid intrusion in a drained host rock also leads to a change of elastic properties. Gassmann showed that the bulk module changes with fluid saturation while the shear modulus remains constant (Gassmann [1951]). He derived empirical equations depending on the fluid pressure, porosity and mineral decomposition of the rock.
Using the Gassmann equation Rice and Cleary expanded the model of Biot using the Skempton coefficient B instead of the Biot coefficient (Biot [1941], Rice and Cleary [1976]):

$$2\ G\epsilon_{ij} = \sigma_{ij} - \frac{\nu}{1+\nu}\sigma_{kk}\delta_{ij} + \frac{3(\nu_{undr} - \nu)}{B(1+\nu)(1+\nu_{undr})}p\delta_{ij} \tag{1.6}$$

Besides pore pressure pertubations also temperature changes can alter the stress state. When rock undergoes a temperature change, e.g. because its pore space is filled with warmer material, it will change its volume. Thermal strains can be calculated most simple by

$$\epsilon_T = -\beta(T - T_0) \tag{1.7}$$

The thermal strain is negative if the temperature is increased, assuming that the body expands. The coefficient of thermal expansion β is normally larger than 0 if the material expands under heat. We can also define the temperature change

$$\theta = T - T_0 \tag{1.8}$$

If the body is locked and can not deform freely the strains cause stresses. These thermal stresses can be derived from the strains but only act in normal directions and have therefore no shear component. Using the vector $I = (1, 1, 0)$ the stresses can be calculated together with the elastic stresses due to load:

$$\sigma = E\epsilon_e + \beta EI\theta \tag{1.9}$$

1.1.1.2 Theory of Plasticity

The elastic and plastic regions are separated by the yield function f. Whenever $f \leq 0$ the stress state is below the critical state and the body deforms elastically. If $f = 0$ then the body is in the plastic domain. I will use the Mohr- Coulomb criteria for shear and the Griffith yield criteria for tensile failure.

$$f_t = \tau - \sigma_m - \sigma_t \tag{1.10}$$
$$f_s = \tau - \sigma_m \cdot \sin\phi - c \cdot \cos\phi \tag{1.11}$$
$$f = max(f_t, f_s) \tag{1.12}$$

Here is σ_t tensile strength, ϕ angle of internal friction, c cohesion, τ stress deviator and σ_m mean stress. τ and σ_m can also be interpreted in terms of Mohr's circle (see figure 1.1).

$$\begin{aligned} \tau &= \sqrt{\frac{(\sigma_{xx} - \sigma_{yy})^2}{4} + \sigma_{xy}^2} \\ \sigma_m &= \frac{\sigma_{xx} + \sigma_{yy}}{2} \end{aligned} \tag{1.13}$$

Typical values for cohesion and friction angle, as well as for elastic properties can be found in literature, for example in Jaeger et al. [2007] or Schön [2011].
The total strain can be calculated as the sum of elastic and plastic strain. The plastic strain rates with the following rule:

$$\dot{\epsilon_p} = 0 \; if \; f < 0 \; or \; f = 0 \; and \; \dot{f} < 0 \tag{1.14}$$
$$\dot{\epsilon_p} = \lambda^p \frac{\partial q}{\partial \sigma} \; if \; f = 0 \; and \; \dot{f} = 0 \tag{1.15}$$

Here is q the flow rule which describes the plastic behavior and λ^p a plastic multiplier. The plastic multiplier can be derived with the requirements $f = 0$ and $\dot{f} = 0$. I use non-associated flow rules for tensile and shear failure (Vermeer and de Borst [1984]).

$$q_t = \tau - \sigma_m \tag{1.16}$$
$$q_s = \tau - \sigma_m \cdot \sin\psi \tag{1.17}$$

where ψ is the angle of dilatancy.

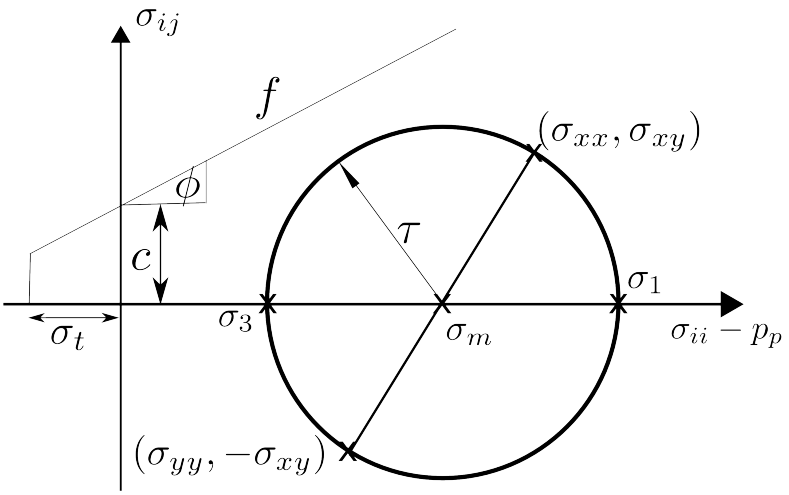

Figure 1.1: Two dimensional Mohr's Circle with maximum and minimum principal stress σ_1 and σ_3, normal stresses σ_{xx} and σ_{yy} and shear stress σ_{xy}. The Mohr's circle is defined by radius τ and midpoint σ_m. The Mohr- Coulomb yield function f is defined by cohesion c, friction angle ϕ and the tensile cut-off σ_t. The Mohr's circle visualizes any stress state of a plane oriented to the principal directions (modified from Vermeer and de Borst [1984]).

The model derived so far is known as perfect- plastic. It is a first approach to simulate irreversible behavior but extensions need to be made for a more realistic model and to achieve a comparison with experimental measurements (cf 1.2). The model is advanced by considering all three plastic parameters (ϕ, c, ψ) not constant but changing them in dependence of plastic deformation.
I mobilize these parameters in dependence of a the effective plastic stress $\bar{\epsilon}_p$, which is a common choice (e.g. Vermeer and de Borst [1984], Salari et al. [2004], Hajiabdolmajid et al. [2002]).

$$\bar{\epsilon}_p = \sqrt{\frac{2}{3}\dot{\epsilon_p}^T \cdot \dot{\epsilon_p}} = \sqrt{\frac{2}{3}\left(\dot{\epsilon}_{p,1}^2 + \dot{\epsilon}_{p,2}^2\right)} \tag{1.18}$$

The cohesional weakening - frictional strengthening (CWFS) model considers the vanishing of cohesion through micro- fracturing and an increased roughness due to a rearranging of grains (Hajiabdolmajid et al. [2002]). The model I use in this work follows the derivation given in Vermeer and de Borst [1984] (see figure 1.2).
For frictional hardening the mobilized friction angle ϕ^* follows:

$$sin\phi^* = sin\phi_0 \cdot \begin{cases} \left(\gamma_f + (1.0 - \gamma_f) \cdot 2.0 \cdot \frac{\sqrt{\bar{\epsilon}_p \cdot \epsilon_f}}{(\bar{\epsilon}_p + \epsilon_f)}\right) & if\ \bar{\epsilon}_p < \epsilon_f \\ 1 & if\ \bar{\epsilon}_p \geq \epsilon_f \end{cases} \tag{1.19}$$

The friction hardening coefficient γ_f determines the initial portion of the maximum internal friction angle ϕ_0. The rate of hardening is determined by ϵ_f.
The drop in cohesion follows:

$$c\left(\bar{\epsilon}_p\right) = c_0 \cdot \left(1 - \gamma_c \cdot exp\left(-\left(\bar{\epsilon}_p/\epsilon_c\right)^2\right)\right) \tag{1.20}$$

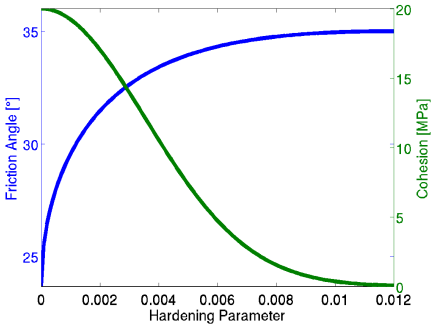

(a) Cohesional weakening and frictional hardening in dependence of the hardening parameter

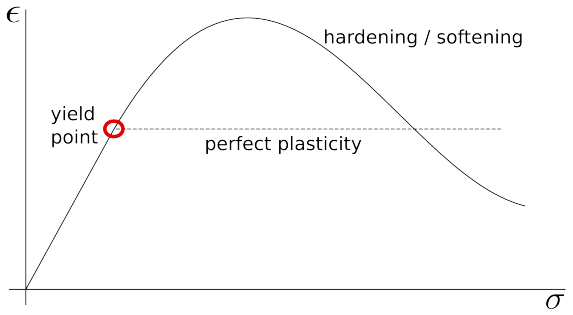

(b) Stress- strain response curve for a CWFS model and a perfect plastic model.

Figure 1.2: Dynamical changes of cohesion and internal friction angle for the described cohesional weakening - frictional strengthening model (CFWS) with respect to the hardening parameter. Minimum friction angle is 70% of the maximum friction angle of 35°. Cohesion vanishes completely. Right figure shows the influence of the CWFS model on the stress- strain curve. The maximum load increases and a stress drop occurs at macroscopic failure. The perfect plastic model instead remains at yield stress. Experimental data can for example be found in Wawersik and Fairhurst [1970].

The cohesion softening coefficient γ_c determines the residual cohesion value as a fraction of the initial cohesion c_0. The rate of weakening is controlled by ϵ_c similar to ϵ_f for frictional hardening. Common values for a maximum friction angle are around 50° and the drop in cohesion around 70% but depend on the rock type. The values of ϵ_c and ϵ_f are around some percentage of deformation. In most cases $\epsilon_f > \epsilon_c$ (cf e.g. Vermeer and de Borst [1984], Hajiabdolmajid et al. [2002], Liu et al. [2012]).
The introduction of hardening changes the plastic multiplier λ^p which contains a so-called hardening module h during active hardening. The hardening module inhibits the dependency of the yield function with respect to the hardening parameter.
Usually the angle of dilatancy ψ is mobilized as well towards ψ^* in dependence of the mobilized friction angle and scaled with the friction angle of constant volume (Vermeer and de Borst [1984]).
Damage describes the degradation of elastic properties (Kachanov [1958]). It has contributions of elastic and plastic strains but itself is a history variable (Chiarelli et al. [2003]). Deformation and allocation of the grains as well as the generation of micro- voids lead to a change in elastic properties (Shao et al. [1998]). Mathematically a damage operator $D \in [0; 1]$ describes this behavior by $E_d = (1-D) \cdot E_0$. Here is E_0 the undamaged elastic operator and E_d the damaged one (Kachanov [1958], see figure 1.3). Cycling experiments are a common way to demonstrate the damage evolution. In these experiments the sample undergoes several loading and unloading cycles. As damage evolution progress during loading the unloading paths vary each time because the elastic parameters decline.
Two main approaches exist to physically describe this behavior. One uses the effective stress model. It assumes that deformation of a body can be calculated independently of the damage operator. Only the stresses which cause the deformation are

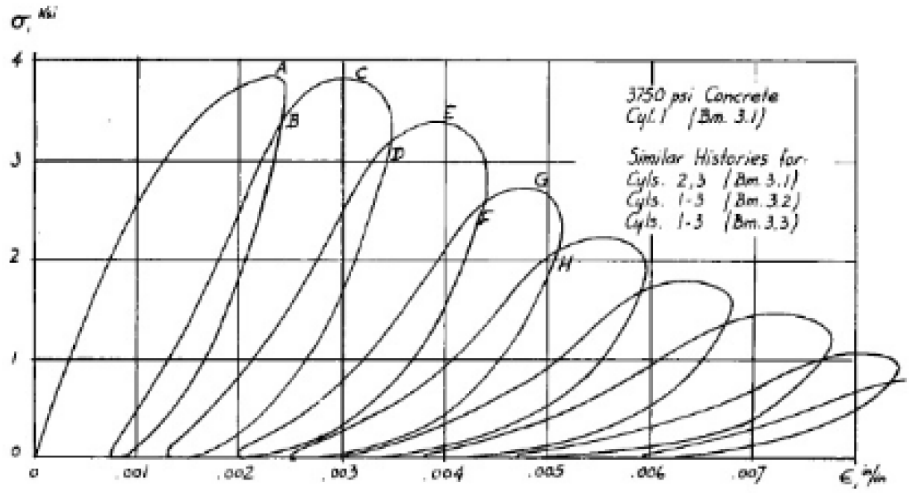

Figure 1.3: Experimental stress- strain curve of a concrete specimen during cyclic loading, taken from Sinha et al. [1964]. Slopes of the loading and unloading curves decrease with increasing strain showing damage growth.

corrected. In these models elasto- plastic deformation is decoupled from damage evolution. Damage can be calculated using different methods, e.g. a damage-equivalent strain (Peerlings et al. [1998], Omidi and Lotfi [2010]) or a damage- surface model (Voyiadjis and Taqieddin [2009]). These models can be rather straight forward to implement (e.g. Taqieddin and Voyiadjis [2009]). The other approach does not need the effective stress model but considers a fully coupled two- surface approach (e.g. Shao et al. [1998], Chiarelli et al. [2003], Salari et al. [2004], Carol et al. [2001]). A yield surface and a damage surface are considered and deformation depends on both. These models are rather cumbersome to implement and often simplifications are utilized to improve runtime and stability of the algorithm. In chapter 2 we will present a physical and numerical two- surface model developing an algorithm able to avoid usual numerical issues occurring within a fully coupled system.
Independent of the chosen approach, thermodynamically consistent models can be derived and observations at field and laboratory scale can be reproduced (e.g. Chiarelli et al. [2003], Wu et al. [2006], Omidi and Lotfi [2010], Omidi et al. [2013], Peerlings et al. [1998]).

1.1.2 Fluid Flow

1.1.2.1 Pressure diffusion

The evolution of fluid pressure in a porous medium can be described with a diffusion equation.
Starting with conservation of mass (Dagger [1997]):

$$\frac{d}{dt}\left(\phi\rho\right) + \nabla\left(\rho v\right) = 0 \tag{1.21}$$

where t is time, ϕ porosity, ρ density and v is Darcy velocity. With the chain rule

this equation can be simplified:

$$\frac{1}{\rho}\frac{\partial \rho}{\partial P}\dot{P} + \frac{1}{\phi\rho}\nabla(\rho v) = 0 \tag{1.22}$$

In porous media different compressibilities have to be considered (Zimmerman [1991]). Besides compressibility of fluid β_f also pore space varies with fluid pressure P.

$$\beta_f = -\frac{1}{\rho}\frac{\partial \rho}{\partial P} \tag{1.23}$$

$$\beta_\phi = -\frac{1}{\phi}\frac{\partial \phi}{\partial P} \tag{1.24}$$

Darcy's equation relates fluid flux with pressure gradient for porous media by introducing permeability k and viscosity η

$$v = -\frac{k}{\eta}\nabla P \tag{1.25}$$

If neglecting source and sink terms, the pressure diffusion is given by

$$\frac{\partial P}{\partial t} = \frac{1}{\phi(\beta_f + \beta_\phi)}\nabla\left(\frac{k}{\eta}\nabla P\right) \tag{1.26}$$

In geological settings the permeability can vary over a large range. Many authors consider it as stress and pressure dependent (e.g. Miller et al. [2004], Carcione and Tinivella [2001], Rutqvist et al. [2002], Latham et al. [2013], Bai et al. [1997], Min et al. [2004]). This has also be shown in experimental studies (Blöcher et al. [2009]). Different studies (e.g. Miller et al. [2004], Carcione and Tinivella [2001]) use an exponential function of permeability in dependence of the normal stress σ_n.

$$k = k_0 \cdot exp^{\left(-\frac{\sigma_n}{\sigma_0}\right)} \tag{1.27}$$

where k_0 is permeability at zero stress, σ_0 is a scaling constant and σ_n can be expressed with maximal and minimal principal stresses σ_1, σ_3 and dip angle θ:

$$\sigma_n = \frac{\sigma_1 + \sigma_3 - 2P}{3} + \frac{\sigma_1 - \sigma_3}{2} \cdot \cos(2\theta) \tag{1.28}$$

Also some authors chose permeability in dependence of a stress dependent porosity (Rutqvist et al. [2002], Min et al. [2004]):

$$\phi = \phi_r + (\phi_0 - \phi_r) \cdot \exp(a \cdot \sigma_n) \tag{1.29}$$

$$k = k_0 \exp[c \cdot (\phi/\phi_0 - 1)] \tag{1.30}$$

where ϕ_0 and k_0 are porosity and permeability at zero stress, ϕ_r is a residual value, a and c are constants.
Besides pressure and stress dependency, permeability can increase rapidly by several orders of magnitude if new fractures are generated (Mitchell and Faulkner [2008]).

Generally, fractures can have significant higher permeability than intact host rock. For fractures pressure dependency of permeability can even be increased in comparison to intact host rock.

1.1.2.2 Two phase flow of water and air

The single phase flow model can be extended considering multiple phases like fluid and gas phase. In the following we will consider a mixture of water and air and assume the phases to be immiscible, isothermal and neglect phase transition. The subscripts $\alpha = w, a$ will indicate water and air phase respectively.
We will start with the conservation of mass but now considering saturation S of each phase (Dagger [1997]):

$$\frac{d}{dt}\left(\phi \rho_\alpha S_\alpha\right) + \nabla\left(\rho_\alpha v_\alpha\right) = 0 \tag{1.31}$$

We perform similar calculations than for the single phase flow, using the definitions for compressibilities and the generalized Darcy velocity v. These phase dependent Darcy velocity includes a phase permeability k_α which varies between 0 and 1 additionally to the intrinsic permeability k_0.

$$v_w = -\frac{k_w \cdot k_0}{\mu_w} \nabla P_w \tag{1.32}$$

Phase permeabilities depend on saturation and can be calculated using the model of vanGenuchten [1980] (see figure 1.4), which show very good agreement with experimental data (Cropper et al. [2011]):

$$\begin{aligned} k_w &= \sqrt{S_w}\left(1 - \left(1 - S_w^{\frac{1}{m}}\right)^m\right)^2 \\ k_a &= \left(1 - S_w\right)^2 \cdot \left(1 - S_w^{\frac{2+3m}{m}}\right) \end{aligned} \tag{1.33}$$

with m and n as constants.
We introduce phase mobility λ:

$$\lambda_\alpha = \frac{-k_\alpha \cdot k_0}{\mu_\alpha} \tag{1.34}$$

The saturation for each phase are coupled because $S_w + S_a = 1$ needs to be valid for all times. We also introduce capillary pressure p_c using again the model of vanGenuchten [1980]. We can then chose water pressure and water saturation as primary variables.

$$P_c = P_a - P_w = \left(S_w^m - 1\right)^{-n} \cdot P_r \tag{1.35}$$

In this model n is a parameter, which usually varies around 3. The second parameter m can be determined using $m = 1 - \frac{1}{n}$. Parameter P_r is a scaling factor for capillary pressure, so that $P_c/P_r \approx 10$ (Cropper et al. [2011]).

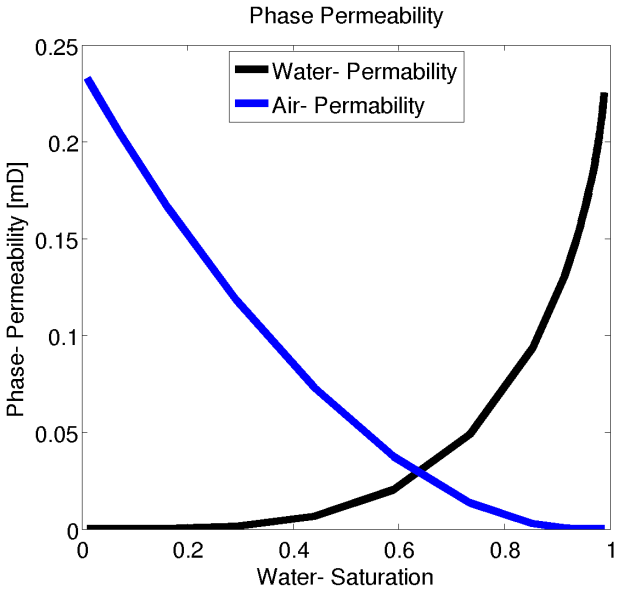

Figure 1.4: Phase permeability calculated with the model of vanGenuchten [1980] in dependence of the water saturation. For a drained case water permeability is zero and increases with increasing saturation towards the intrinsic permeability. Permeability of air phase decreases simultaneously.

Two strongly coupled, parabolic differential equations exist for the two primary variables S_w, P_w, which is called the Pressure- Saturation formulation. It is not limited to homogeneous systems and converges towards one phase flow for saturation close to 1 (Helmig [1997]).

$$\begin{aligned} \nabla\left(\lambda_w \nabla P_w\right) &= \phi\left(S_w c_w \frac{\partial P_w}{\partial t} + \frac{\partial S_w}{\partial t}\right) \\ \nabla\left(\lambda_a \nabla\left(P_c + P_w\right)\right) &= \phi\left(\left(1 - S_w\right) c_a \frac{\partial\left(P_c + P_w\right)}{\partial t} - \frac{\partial S_w}{\partial t}\right) \end{aligned} \tag{1.36}$$

To decouple the equations we assume the air to be infinitely mobile, which means the air reservoir is infinitely large and air can moves freely. The air pressure is under this assumptions constant over the whole domain and can be chosen as the zero reference (Richards [1931]). The capillary pressure becomes $P_c = -P_w$ and the Richards equation remains.

$$\frac{\partial P_w}{\partial t} = \frac{1}{\phi\left(S_w \cdot c_w + C\left(P_w\right)\right)} \nabla\left(\lambda_w \nabla P_w\right) \tag{1.37}$$

with capacity $C\left(P_w\right) = \frac{\partial S_w}{\partial P_w}$, which is defined by equation 1.35.

1.1.2.3 Heat Transport

The fundamentals of heat transport in a porous media are described by the conservation of energy. I use a so called non-local approach in which I calculate fluid- and

rock temperature separately. Heat is exchanged over the contact surface depending on the material properties. Several values here have to be estimated as they are difficult to determine in laboratory and almost impossible to estimate on field scale. Especially contact area A and overall hear transfer coefficient h suffer from this inaccuracy and have to be estimated for highly fractured reservoirs (Shaik et al. [2011]).
We determine heat transfer Q as:

$$Q = hA\ (T_f - T_r) \tag{1.38}$$

where T is temperature of fluid f and rock r. This transfer term is equal to the source or sink term in the conservation of energy. Note that different signs for the transferred heat need to be used between fluid and rock respectively. Heat transport in the solid is described by a diffusion equation.

$$\frac{\partial T_r}{\partial t} = \frac{\kappa_r}{(1-\phi)\rho_r c_{pr}} \nabla^2 T_r + \frac{1}{(1-\phi)\rho_r c_{pr}} Q \tag{1.39}$$

where ϕ is porosity, κ_r thermal conductivity, ρ density and c_{pr} heat capacity (Bejan [2013]). The heat of the fluid is limited to the pore space but also considers an advection term with Darcy velocity v.

$$\frac{\partial T_f}{\partial t} = \frac{\kappa_f}{\phi\rho_f c_{pf}} \nabla^2 T_f - \frac{1}{\phi\rho_f c_{pf}} Q - \nabla(vT_f) \tag{1.40}$$

This model is limited to a saturated environment and neglects phase changes which could occur if temperature exceeds given limits for the materials. We also consider non additional heat sinks or sources. This could easily be done by adding extra terms but is out of scope for the use case in this work.

1.1.3 Numerical Implementation

The resulting set of equations of the derived theoretical model is way to complex to be solved analytically. Therefore numerical simulations are used to obtain results for specific cases and scenarios. In this section I will shortly explain the numerical scheme used for this work.
I use finite differences with a staggered grid described in Saenger et al. [2000] and Cruz- Atienza and Virieux [2004] as well as explicit time stepping (Virieux [1986]). Simplified, this staggered grid can be thought as three grids, each one shifted half a grid step in reference to the other (see figure 1.5). The sizes of the grid are one point less in each dimension in comparison to the further one. The largest grid is used to calculate the total stresses. Besides the total stresses also fluid pressure and temperature are defined on these grid points. The next one is the velocity grid. So velocity and displacement are defined on this grid. The smallest grid is identical with the outermost total stress grid but has two grid points less in each dimension. It is the effective stress grid. On this grid the effective stresses are defined but also most of the other variables like yield function, hardening parameter etc.

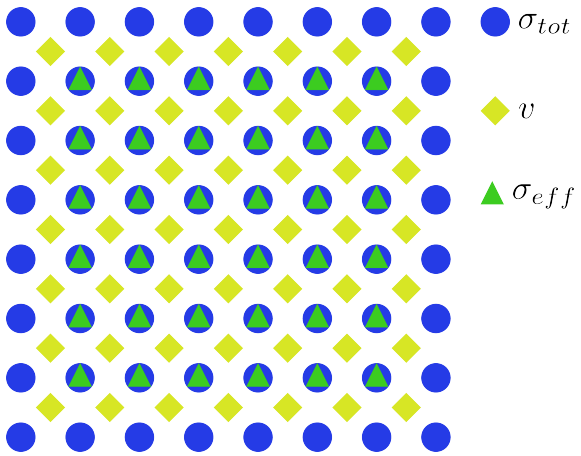

Figure 1.5: Symbolic sketch of the used staggered grid. Three grids are used and shifted to each other by half the grid site. Blue dots for the outermost total stress grid, yellow boxes for the velocity grid and green triangles for the effective stress grid. Each grid is one grid point less in each direction than the next one. Boundary conditions only need to be applied in the total stress grid. See also Saenger et al. [2000].

The used staggered grid has several advantages. First of all the structure of the staggered grids enables a straightforward building of the differentials. The differentials are build symmetrically in all directions. The number of involved grid points for each differential depends on the chosen order of the Taylor approximation in the finite difference derivation. I use second and fourth order (Cruz- Atienza and Virieux [2004]). The discretized formulation of the equations can be found in Virieux [1986] and Rozhko [2007]. Also the chosen grid only needs boundary conditions for the variables defined on the outermost grid. These can be overwritten, if needed, by additional boundary conditions for the velocity. This is for example useful if a no-slip boundary is applied.
The staggered grid is very suitable for parallelization with distributed memory. Several developed algorithms presented in this work need high computational power and a small spatial and temporal resolution. Both increase the runtime of the simulation. Therefore the load is distributed over several cores and nodes. Most simulations were performed using the KRYPTON cluster of the Geodynamics Group of the Steinmann Institute, University of Bonn. This cluster consists of 8 nodes with 6 cores each. I achieved the best results, meaning shortest runtime of a simulation, using a hybrid parallelization. Parallelization techniques can roughly be separated in shared and distributed memory. In a shared memory environment all involved CPU (central processing unit) cores access the same physical memory but each core only executes its own spatial domain. I use openMP as a command tool for shared memory parallelization. The advantage hereby is that the spatial decomposition is down by openMP itself, depending on the capacity and workload of the available cores. The disadvantage of this method is the need for common physical memory which means for the KRYPTON cluster that openMP can only be used inside of each node distributing over the six available cores.
To communicate between separated nodes with distributed memory I use openMPI.

It is a message passing interface (MPI). Each node sends and receives information it needs from the other nodes via messages. Here the mentioned benefit of the used staggered grid becomes evident. Due to the staggered grid only variables on the outermost grid need to be communicated between nodes as all other values can be derived from there. Hence, message length is short and the algorithm only needs to communicate once during calculation of each time step. Communicating between nodes can be a bottleneck during simulation and therefore needes to be efficient. The grid itself enables a good parallelization. Also to be efficient a fast connection between the nodes need to be established which is the case at the KRYPTON cluster using Infiniband. In opposite to openMP, openMPI needs a predefined spatial separation for each node. As load balance is required for best performance a separation in 4 spatial domains for the MPI processes is the most suitable for a two-dimensional simulation.
Hybrid parallelization describes the combination of both: Using openMPI to communicate between separated nodes and openMP for parallelization within each node. In total these results in 24 threads executing in parallel, employing 4 nodes with 6 cores each (see figure 1.6). With this setup most of the presented results could be a achieved in hours.

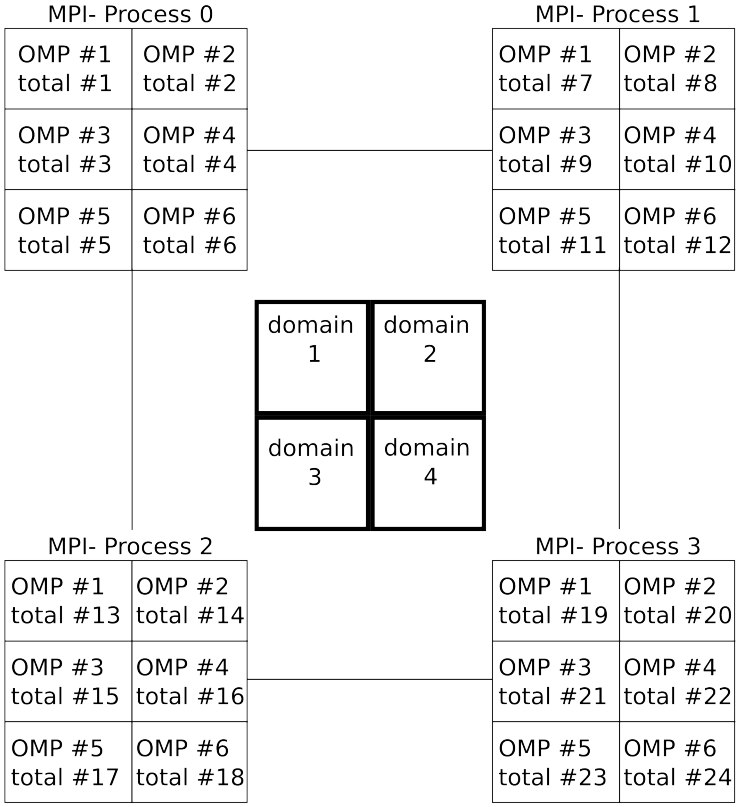

Figure 1.6: The simulated spatial region is divided into 4 domains. Each domain is handled by one MPI- process per node. Within each MPI process the load is shared by 6 openMP (OMP) threads, one for each core. In total 24 threads are executing in parallel. Each MPI process only needs to communicate with its two direct neighbors to minimize communication.

1.2 Summary of scientific articles

In this section I present a short summary of the scientific papers which are part of this work

1.2.1 Return algorithm for a strongly coupled elasto-plastic damage model for rock and concrete

This paper focus on the numerical implementation of a two surface elasto- plastic damage model. In numerical damage mechanics so called effective stress models are common. In these models it is assumed that deformation in a material is independent of the damage state and only stresses depend on the damage operator. The equations are therefore less coupled and can be implemented in almost any elasto- plastic model. In the fully coupled model as derived in part I with a yield and a damage function this is more complex.
We use a classic elastic predictor - plastic corrector scheme as a starting point, separating elastic and plastic deformation. In every time step we test the damage function twice: once after the elastic and again after the plastic deformation. If damage evolves we correct the elastic stresses and recalculate the plastic stresses following the equations derived in part I of these consecutive papers.
This paper also pays attention to a numerical issue which arises whenever functions following the Kuhn- Tucker conditions are used. The damage and the yield function are only defined on the negative half space including zero. Due to floating point arithmetic the zero can not be exactly calculated which leads to a so called 'surface drift'. These drift occurs in every time step and is additive. Therefore it needs to be prevented. In plastic calculations several algorithms exist handling these problems. We show that it is critical to consider such a drift from the damage surface as well and develop algorithms for a two surface model analog to a yield surface drift. To validate our approach we compare simulation results with experimental data as well as with numerical studies of other authors.

1.2.2 A new method to estimate the occurrence and magnitude of simulated rock failure events

In material sciences acoustic emissions are a popular tool to test and observe a solid body. They occur in various materials (metal, ceramic, polymer, concrete, rock) and signal the development a new fracture or the growth of an existing one. In geoscience acoustic emissions have the same source mechanism than seismic wave. They are often used as an analog for seismic waves on laboratory scale. In continuum mechanic there is no dedicated value which describes an acoustic emission. As they are waves the velocity and displacement are natural parameters for the wave but in numerical geotechnical simulations time steps are much larger than the wave frequency and so the waves itself are not captured. This would also be numerically inefficient. There exist other approaches linking acoustic emissions to the yield function, the

damage parameter or other defined properties which all have different advantages and disadvantages.
We propose the deviatoric strain rate as a proxy for acoustic emissions in numerical simulations. The deviatoric strain is the part of the strain which is connected to shear movement. Rapid changes in deviatoric strain can be observed at fracture generation and propagation. This leads to a rapid increase in deviatoric strain and is followed by a drop in the yield function due to stress release after the slip. In this paper we present two algorithms to detect rapid changes in the yield function. One algorithm uses the ratio of short- and long- term moving average of the deviatoric strain rate, the other uses the slope of the deviatoric strain to detect events. With these methods we are able to calculate the seismic moment using the area of slip and the displacement of the event. A method to determine the area of slip and the displacement is given. The seismic moment can be compared with the wave amplitude of an acoustic emission.
We identify several important features of acoustic emissions which occur during various experiments. We test our approach by implementing the developed algorithm in a numerical model and simulate several laboratory experiments in drained and undrained conditions. We achieve a very well agreement between the events detected during numerical simulation and the laboratory results.

1.2.3 Numerical Simulation of the 2008 Bohemian earthquake swarm

Earthquake swarms occur in the Eger Graben system since centuries. In the last decades swarms mainly concentrate around the city Novy Kostel in the german - czech border region. Many mofettes and springs with high CO_2 concentration as well as the mineral decomposition of the gases indicate that swarms are driven by overpressured, supercritical CO_2 emerging from the upper mantle. I simulate the region using the developed THM model outlined before to simulate the 2008 swarm occurring on the southern subcluster of the fault system. I use the algorithm to detect acoustic emission in rock specimens, presented in the scientific paper before, to detect and localize earthquakes in the numerical simulation and determine their magnitude.
With these tools I am able to reproduce the seismic characteristics of the region in general and of the 2008 swarm like the Gutenberg- Richter law, the magnitude change over time as well as the spatial- temporal evolution of the earthquakes. I show that a point source with a pressure of around 10 - 20 MPa above hydrostatic is sufficient to initiate the swarm while thermal effects can be neglected. Also the unequal evolution of earthquakes below and above the source can be reproduced due to the hydrostatic pressure and gravity effects on the permeability. I also show that the adopted algorithm to look for analogs for earthquakes in a numerical simulation is able to reproduce all characteristic patterns of the earthquakes within the modeled region.

Chapter 2

Return algorithm for a strongly coupled elasto-plastic damage model for rock and concrete

Abstract

In this article we present a numerical algorithm for the computation of a strongly-coupled formulation of the poro- elasto- plastic damage model including hardening and softening. We use a yield surface as well as a damage surface to calculate plastic deformation and damage growth. Implementation of such a fully coupled two- surface plastic damage model can be cumbersome. The algorithm we present in this work considers four possible cases: purely elastic deformation, elastic damage, purely plastic deformation and plastic damage. We use an elastic predictor- plastic corrector scheme as a base and divide any predictor step in an elastic and a plastic contribution towards deformation and damage growth. Elastic and plastic damage contributions are then tested separately with the damage surface. While normally in two-surface plastic damage models drift from yield- and damage surfaces is neglected, we show that these drifts are significant and need to be prevented using return algorithms. Our algorithm is based on thermodynamic conjugated forces paying special attention to the damage surface drift.

Our model is implemented into a finite- difference staggered grid. Functionality of model and algorithm is validated through several tests and comparisons with experimental data available in literature. The simulated results show good agreement with experimental data and prevention of numerical surface drift.

2.1 Introduction

There are two different approaches to model damage effects: effective plasticity plus damage and the coupled plastic- damage models. In the first models the plasticity is calculated in the effective stress space, while continuum damage mechanics is used to determine stiffness degradation. This method decouples stiffness degradation and plastic deformation and is therefore straightforward to implement in any working elasto- plastic model. Here the effective stress principle is used which assumes that damaged and undamaged rock deform the same way. Deformation is calculated using the undamaged stresses and elastic parameters. These stress values are corrected using the damage operator but the corrected stresses are not used in the next time step to calculate the deformation and the elastic properties are kept constant during the whole deformation. The damage operator is calculated following different approaches, even two- surface models with decoupled yield and damage function are possible. With the damage operator the stresses are corrected. Thermodynamically consistent models can be derived, (e.g. Voyiadjis and Taqieddin [2009], Wu et al. [2006], Grassl and Jirasek [2006], Bobinski and Tejchman [2006], Marzec and Tejchman [2012], Omidi et al. [2013], Mortazavi and Molladavoodi [2012]). Numerical implementation is described in detail in (e.g. Taqieddin and Voyiadjis [2009], Shao et al. [2006], Bielski et al. [2006], Omidi and Lotfi [2010], Xie et al. [2011]).

On the other hand, combined plastic- damage models result in strongly coupled equations by using the degradation of elastic properties for calculating deformation (e.g. Shao et al. [2006], Salari et al. [2004], Chiarelli et al. [2003]). Then, these models can be calibrated directly using experimental observations. We see the main advantage of these coupled models by avoiding the assumption of effective stresses. While the use of effective stresses is a widely accepted assumption, it rest on considering plastic deformation completely decoupled to damage evolution, which is unreal. However, it is generally preferred over the coupled plastic damage models because coupled models results in complex algorithms which often become unstable (Taqieddin [2008]).

As plastic- damage models result in a complicated numerical scheme, their numerical implementation is often simplified when it comes to numerical yield surface drift (Potts and Gens [1985], Sloan [1987]). This drift occurs in any numerical simulation using continuum elasto- plastic equations independent of the numerical grid, chosen method or yield function. It describes the fact, that calculated values for the yield surface during plastic deformation will always differ slightly from zero. These differences add up in every time step and influence the results dominantly if no return algorithm is used to prevent and limit further drift. Several stable algorithms exist to prevent surface drift with any arbitrary accuracy. An overview about methods and implementation can be found in Potts and Gens [1985] and Abbo [1997].

In coupled plastic- damage models, a double surface approch is used (Carol et al. [2001]), one surface associated to yielding and the other one related to damage evolution from which drifting is also possible. We present an explicit numerical algorithm for a double surface model, considering numerical drift from both surfaces. We follow the evolution of damage, its drifting from the damage surface and its

influence on the stresses. Our model is verified with comparison to experimental data.
In the following section we will derive our rheological model and proceed by presenting the developed overall algorithm considering all possible combinations: purely elastic, elastic damage, purely plastic and plastic damage and describe in detail the surface drift algorithm for the coupled plastic- damage case. In the fourth section the model is tested by simulating various scenarios and experiments. The work is concluded with a discussion of model and algorithm.

2.2 Rheological Model

The behavior of a two dimensional rock in the elastic domain is described by the elastodynamic equations:

$$\frac{\partial V_x}{\partial t} = \frac{1}{\rho}(\frac{\partial \sigma_{xx}}{\partial x} + \frac{\partial \sigma_{xy}}{\partial y}) \tag{2.1}$$

$$\frac{\partial V_y}{\partial t} = \frac{1}{\rho}(\frac{\partial \sigma_{yy}}{\partial y} + \frac{\partial \sigma_{xy}}{\partial x}) \tag{2.2}$$

$$\frac{\partial \sigma_{xx}}{\partial t} = (\lambda + 2\mu)\frac{\partial V_x}{\partial x} + \lambda\frac{\partial V_y}{\partial y} \tag{2.3}$$

$$\frac{\partial \sigma_{yy}}{\partial t} = \lambda\frac{\partial V_x}{\partial x} + (\lambda + 2\mu)\frac{\partial V_y}{\partial y} \tag{2.4}$$

$$\frac{\partial \tau_{xy}}{\partial t} = \mu\left(\frac{\partial V_x}{\partial x} + \frac{\partial V_y}{\partial y}\right) \tag{2.5}$$

where μ and λ are the Lamé constants, ρ is the density, V_x and V_y is the velocity vector and σ_{xx}, σ_{yy}, τ_{xy} is the stress tensor.
Plastic deformation of rocks is modeled using Mohr-Coulomb criteria

$$f^p = \tau - \left(\sigma_m - \frac{C^*}{tan(\varphi^0)}\right) \cdot sin(\varphi^*) \tag{2.6}$$

where f^p is the yield function, C^* is the mobilized cohesion, φ^* is the mobilized internal friction angle,φ^0 is the maximal internal frictional angle, τ is the stress deviator, σ_m is the mean stress.
Cohesion and internal friction angle are mobilized in terms of a cohesion weakening and frictional strengthening model (CWFS) in dependence of the effective plastic strain $\bar{\epsilon}_p$ (Hajiabdolmajid et al. [2002]). The mobilized values for friction angle, cohesion and dilatancy angle are calculated following (Vermeer and de Borst [1984]). The plastic strain rates are given by

$$\dot{\epsilon}_{ij}^{pl} = 0 \text{ for } f^p < 0 \text{ or } f^p = 0 \text{ and } \dot{f}^p < 0 \tag{2.7}$$

$$\dot{\epsilon}_{ij}^{pl} = \lambda^p \frac{\partial q}{\partial \sigma_{ij}} \text{ for } f^p = 0 \text{ and } \dot{f}^p = 0. \tag{2.8}$$

with λ^p is the plastic multiplier and q is the flow rule.
The effective plastic strain $\bar{\epsilon}_p$ follows from there

$$\bar{\epsilon}_p = \sqrt{\frac{2}{3}\dot{\epsilon_p}^T \cdot M \cdot \dot{\epsilon_p}} \tag{2.9}$$

where M is a weighting matrix (Abbo [1997]).
We use non-associative plastic flow rules (Vermeer and de Borst [1984])

$$q = \tau - \sigma_m \cdot sin(\psi^*) \tag{2.10}$$

where ψ^* is the mobilized dilatancy angle.
Using equation 2.7 the hardening parameter $\bar{\epsilon}_p$ can be calculated with a function $l(q, \sigma)$ using λ^p

$$\bar{\epsilon}_p = \lambda^p \cdot l(q, \sigma) \tag{2.11}$$

with

$$l(q, \sigma) = \sqrt{\frac{2}{3}\frac{\partial q}{\partial \sigma}^T M \frac{\partial q}{\partial \sigma}} \tag{2.12}$$

2.2.1 Damage evolution

Propagation of the scalar damage operator D is described by an energy-based damage function f^d and an associated flow rule.

$$f^d(Y_v, D) = Y_v - r(D) \tag{2.13}$$

Following Salari et al. [2004] and Carol et al. [2001] the energy resistance function $r(D)$ can be written as

$$r(D) = r_0(1 - D)^{p-1} \tag{2.14}$$

where r_0 is the modulus of resilience (Mortazavi and Molladavoodi [2012], Salari et al. [2004], Carol et al. [2001]) and p a free parameter. The volumetric part of the thermodynamic damage force Y_v symbols the energy demand with the parameter c depending on tensile or compressive load.

$$Y_v = \frac{1}{2}K^0\langle\epsilon_v^e\rangle^2 + c\int_0^{\epsilon_v^p} |\sigma_m|\langle d\epsilon_v^p\rangle \tag{2.15}$$

Here K^0 is the undamaged bulk modulus, $\epsilon_v^{e,p}$ elastic and plastic volumetric strain and $\langle\ \rangle$ indicate only tensile contributions are considered. Mean stress is σ_m. The time derivative is

$$\dot{Y}_v = K^0\langle\epsilon_v^e\rangle\dot{\epsilon}_v - K^0\langle\epsilon_v^e\rangle\dot{\epsilon}_v^p + c|\sigma_m|\langle\dot{\epsilon}_v^p\rangle \tag{2.16}$$

This results in an equation for the damage evolution considering strain decomposition.

$$\dot{f}^d = \frac{\partial f^d}{\partial Y}\Bigg[K^0\langle\epsilon_v^e\rangle I\dot{\epsilon} - \lambda^p\left(K^0\langle\epsilon_v^e\rangle\left(\frac{\partial q}{\partial\sigma_{xx}}+\frac{\partial q}{\partial\sigma_{yy}}+\frac{\partial q}{\partial\sigma_{zz}}\right) - c|\sigma_m|\langle\frac{\partial q}{\partial\sigma_{xx}}+\frac{\partial q}{\partial\sigma_{yy}}+\frac{\partial q}{\partial\sigma_{zz}}\rangle\right)\Bigg] + \frac{\partial f^d}{\partial D}\dot{D} = 0 \tag{2.17}$$

This can be further simplified using $R_d = \frac{\frac{\partial f^d}{\partial Y_v}}{\frac{\partial f^d}{\partial D}} = \frac{-1}{r_0\,(p-1)\,(1-D)^{p-2}}$ and an appropriate function $m(q,\sigma)$.

$$\dot{D} = -R_d K^0\langle\epsilon_v^e\rangle I\dot{\epsilon} + \lambda^p R_d\left(K^0\langle\epsilon_v^e\rangle m(q,\sigma) - c|\sigma_m|\langle m(q,\sigma)\rangle\right) \tag{2.18}$$

where

$$m(q,\sigma) = \frac{\partial q}{\partial\sigma_{xx}}+\frac{\partial q}{\partial\sigma_{yy}}+\frac{\partial q}{\partial\sigma_{zz}} \tag{2.19}$$

With presence of damage, the elastic relationship with the elasticity tensor E

$$\sigma = E\cdot\epsilon^e \tag{2.20}$$

changes due to stiffness degradation to

$$\sigma = E^d\cdot\epsilon^e = (1-D)E^0\epsilon^e \tag{2.21}$$

with the damaged and undamaged elasticity tensor $E^d = (1-D)E^0$.

2.2.2 Elasto-plastic damage coupling

Based on elasto- plastic and damage equations a system of two linear equations is found for the two parameter λ^p and $\dot{D}$. It can be solved with Cramer's rule for two unknowns with a general plastic denominator

$$P_{denom} = \left(\frac{\partial f^p}{\partial\sigma}^T E^d\frac{\partial q}{\partial\sigma} - \frac{\partial f^p}{\partial\kappa}l(q,\sigma)\right) + R_d\left(K^0\langle\epsilon_v^e\rangle m(q,\sigma) - c|\sigma_m|\langle m(q,\sigma)\rangle\right)\cdot\left(\frac{\partial f^p}{\partial\sigma}^T E^0\epsilon^e\right) \tag{2.22}$$

to

$$\lambda^p = \frac{\frac{\partial f^p}{\partial\sigma}^T E^d\dot{\epsilon} + \left(\frac{\partial f^p}{\partial\sigma}^T E^0\epsilon^e\right)\cdot R_d K^0\langle\epsilon_v^e\rangle I\dot{\epsilon}}{P_{denom}} \tag{2.23}$$

Equation 2.18 can be used to calculate $\dot{D}$ for a known λ^p.

2.3 Numerical Algorithm

In the absence of damage, various numerical integration schemes can be found in literature (e.g. Abbo [1997], Sloan et al. [2001], Crisfield [1991]). The fundamental structure of our algorithm is based on the elastic predictor - plastic corrector scheme. In the elastic predictor - plastic corrector scheme an elastic deformation is assumed at first. If this step causes an illegal stress state $f^p > 0$, only the elastic part below the yield function, $f^p < 0$, is considered. The other part of the predictor step is used to calculate the plastic stress. A detailed description of the algorithm can be found in Abbo [1997] and Sloan et al. [2001].
As we consider damage, each part of the predictor step, elastic and plastic, is determined without any change in damage. The stress and strain values after the elastic deformation, and again after the plastic deformation, are tested with the damage function. If damage evolution takes place, prior stress values are corrected (elastic domain) or re-calculated (plastic domain) considering damage evolution.
In general, 4 cases have to be separated:

- purely elastic $f^p < 0$ and $f^d < 0$
- elastic + damage $f^p < 0$ and $f^d \geq 0$
- purely plastic (elastic content handled extra) $f^p \geq 0$ and $f^d < 0$
- plastic + damage $f^p \geq 0$ and $f^d \geq 0$

The complete overall algorithm is detailed below (see also figure 2.1):

1. Enter with stress σ_n, strain increment $\Delta\epsilon$ and hardening parameter κ_n with n indicating the prior time step.
2. Calculate the elastic stress increment as part of the elastic predictor: $\Delta\sigma^e_{n+1} = E^d_n \Delta\epsilon$.
3. Test the trial stress $\sigma_{trial} = \sigma_n + \Delta\sigma^e_{n+1}$ in the yield function f^p.
   - If $f^p > 0$ calculate the intersection α with the yield surface following Abbo [1997] and set $\sigma_{n+1} = \sigma_n + \alpha\Delta\sigma^e_{n+1}$ and $\Delta\epsilon = (1-\alpha)\Delta\epsilon$.
4. Update $\langle\epsilon^e_v\rangle$.
5. Test the damage function f^d with the updated $\langle\epsilon^e_v\rangle$.
   - If $f^d \geq 0$ update the damage coefficient D_{n+1} using equation 2.18 with $\lambda^p = 0$ and update elastic tangent matrix E^d. Correct recent stress with $\sigma_{n+1} = \sigma_n \cdot \frac{1-D_{n+1}}{1-D_n}$ (Shao et al. [2006], Salari et al. [2004]).
6. Calculate plastic stress, if $f^p \geq 0$ with

$$\lambda^p = \frac{E^0 \frac{\partial g^p}{\partial \sigma} \frac{\partial f^p}{\partial \sigma}^T E^0}{\left(\frac{\partial f^p}{\partial \sigma}^T E^d \frac{\partial g^p}{\partial \sigma} - \frac{\partial f^p}{\partial \kappa} l(g^p, \sigma)\right)} \tag{2.24}$$

   See detailed algorithm e.g. in Sloan et al. [2001].

7. Update the plastic contribution in Y_v and test f^d again.

   - If $f^d \geq 0$ withdraw results from step 6 and use equations 2.18 and 2.23 to calculate coupled plastic stresses and damage evolution. Update elastic tangent matrix E^d. See detailed algorithm below.

In numerical continuum mechanics it is reasonable to let D asymptotically approach 1 (Mortazavi and Molladavoodi [2012]). This can easily achieved by changing the resistance part in f^d to

$$r(D) = r_0(\Gamma - D)^{p-1} \tag{2.25}$$

with $\Gamma \leq 1$.

2.4 Yield- and Damage- surface return algorithm

Potts and Gens [1985] and Crisfield [1991] pointed out that the small numerical inaccuracy at determining $f^p = 0$ is additive at every time step and causes wrong results in the stress space. The standard algorithm to prevent yield- surface drift, if damage is neglected or weakly coupled, contains two mechanisms: consistent and normal correction. The consistent correction conserves plastic strain and modifies the hardening parameter. It is the preferred structure but does not converge unconditionally. If the consistent correction fails, the unconditionally stable normal correction is applied, which corrects the stresses back to the yield surface in the normal direction (Abbo [1997], Crisfield [1991]).
We adopt both correction schemes of the purely plastic case for the coupled plastic-damage model. The surfaces can be approximated using Taylor expansion for first order terms.

$$f^p = f_0^p + \frac{\partial f^p}{\partial \sigma}\delta\sigma + \frac{\partial f^p}{\partial \kappa}\delta\kappa \tag{2.26}$$

$$f^d = f_0^d + \frac{\partial f^d}{\partial Y_v}\delta Y_v + \frac{\partial f^d}{\partial D}\delta D \tag{2.27}$$

We use similar relationships as above while keeping the strain constant ($\delta\epsilon = 0$)

$$\delta\sigma = -\delta\lambda^p E^d \frac{\partial g^p}{\partial \sigma} - \delta D E^0 \epsilon^e \tag{2.28}$$

$$\delta\kappa = \delta\lambda^p \; l(g^p, \sigma) \tag{2.29}$$

$$\delta Y_v = -\delta\lambda^p \left(K^0 \langle \epsilon_v \rangle m(g^p, \sigma) - c|\sigma_m| \langle m(g^p, \sigma) \rangle \right) \tag{2.30}$$

A linear system for the two unknowns $\delta\lambda^p$ and δD can be formulated.

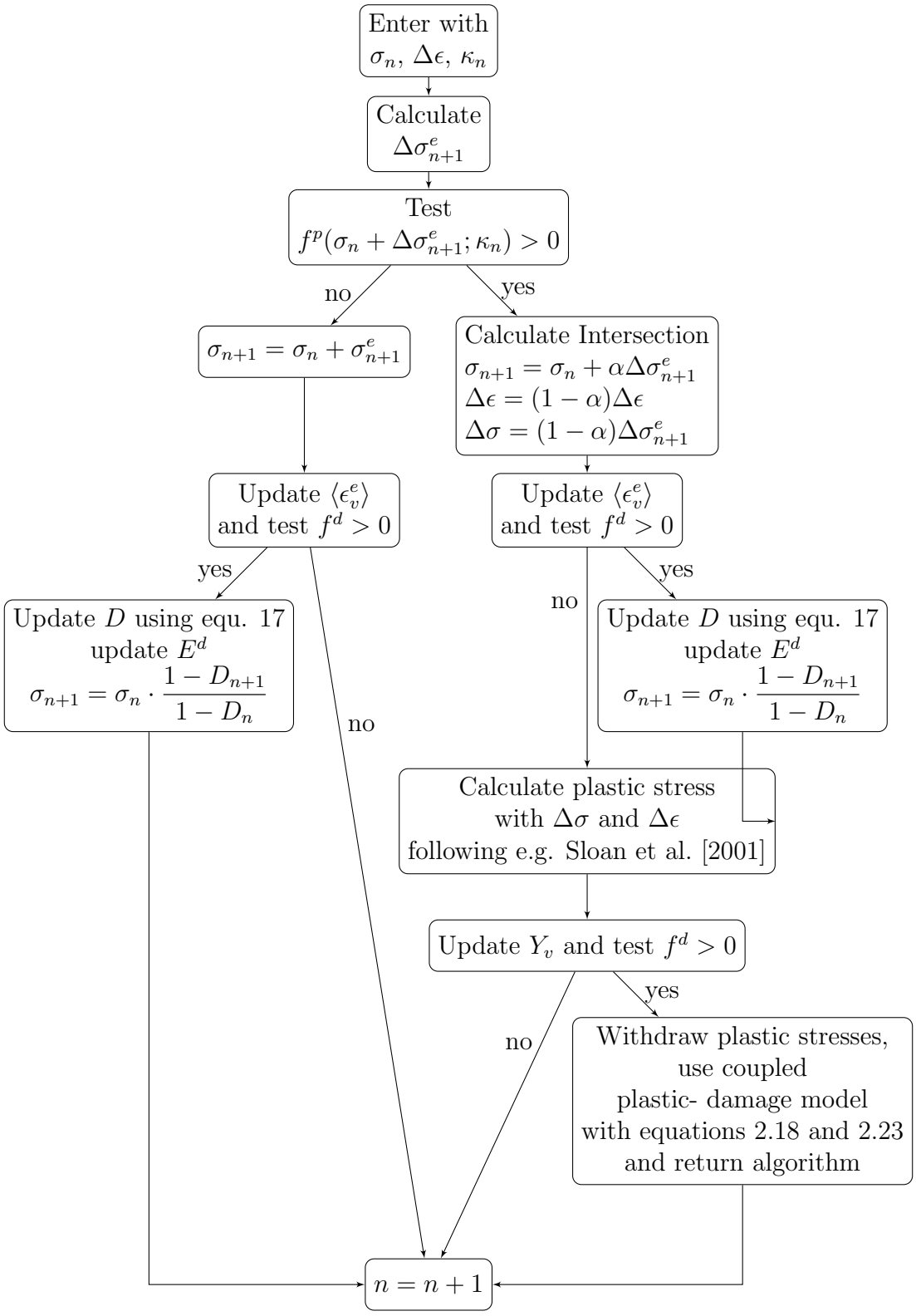

Figure 2.1: Flowchart for the overall algorithm. Considering all four possible cases: purely elastic, elastic- damage, purely damage, coupled plastic- damage. Elastic and plastic steps are separated using an elastic predictor and determing the intersection of it with the yield function. The coupled plastic- damage case is discussed later in the text in detail.

$$f_0^p = \delta\lambda^p \left(\frac{\partial f^p}{\partial \sigma}^T E \frac{\partial g^p}{\partial \sigma} - \frac{\partial f^p}{\partial \kappa} l(g^p, \sigma) \right) + \delta D \left(\frac{\partial f^p}{\partial \sigma}^T E^0 \epsilon^e \right) \tag{2.31}$$

$$\frac{-f_0^d}{\frac{\partial f^d}{\partial D}} = \delta\lambda^p \left(-R_d\right) \left(K^0 \langle \epsilon_v \rangle m(g^p, \sigma) - c|\sigma_m| \langle m(g^p, \sigma) \rangle \right) + \delta D \tag{2.32}$$

The system is solved using Cramer's law.

$$\delta\lambda^p = \frac{f_0^p + \frac{f_0^d}{\frac{\partial f^d}{\partial D}} \left(\frac{\partial f^p}{\partial \sigma}^T E^0 \epsilon^e \right)}{P_{denom}} \tag{2.33}$$

Now we determine stresses, hardening parameter and damage operator.

$$\delta D = \frac{-f_0^d}{\frac{\partial f^d}{\partial D}} + \delta\lambda^p R_d \left(K^0 \langle \epsilon_v \rangle m(g^p, \sigma) - c|\sigma_m| \langle m(g^p, \sigma) \rangle \right) \tag{2.34}$$

$$\delta\sigma = -\delta\lambda^p E^d \frac{\partial g^p}{\partial \sigma} - \delta D E^0 \epsilon^e \tag{2.35}$$

$$\delta\kappa = \delta\lambda^p l(g^p, \sigma) \tag{2.36}$$

Similar to plastic correction without damage, this correction does not converge unconditionally. For this case a normal correction has to be applied for both yield surfaces as well. Again we assume the stress change to be normal to the plastic yield surface while the hardening parameter as well as the damage operator remain unchanged.
We adopt the equation for the correction of the plastic multiplier and the stress:

$$\delta\sigma = -\delta\lambda^p \frac{\partial f^p}{\partial \sigma} \tag{2.37}$$

$$\delta\lambda^p = \frac{f_0^p}{\frac{\partial f^p}{\partial \sigma}^T \frac{\partial f^p}{\partial \sigma}} \tag{2.38}$$

The damage surface is effected because its conjugated thermodynamic force is corrected.

$$\delta Y_v = -\delta\lambda^p \left(K^0 \langle \epsilon_v \rangle m(g^p, \sigma) - c|\sigma_m| \langle m(g^p, \sigma) \rangle \right) \tag{2.39}$$

As mentioned, the damage operator remains unchanged.
The algorithm for the coupled damage- plastic case is detailed below:

1. Chose the parameter c corresponding to ϵ_v^e.
2. Solve iterative or implicit for λ^p and $\dot{D}$ using equations 2.23 and 2.18.
3. Update stresses σ, hardening parameter $\bar{\epsilon_p}$ and Y_v using equations 2.11 and 2.15.

4. Calculate yield- and damage functions f^p and f^d using equations 2.6 and 2.13.

5. While $|f^p| > FTOL$, where $FTOL$ is a tolerance value around 0, use consistent correction.

    - Calculate $\delta\lambda^p$ and δD using equations 2.33 and 2.34. Solve iterative or implicit.
    - Correct σ, $\bar{\epsilon_p}$ and Y_v.
    - Calculate yield- and damage functions f^p and f^d.
    - If $f^p > f^p_{old}$, where f^p_{old} describes the yield function of the stress state prior to the last correction step, use normal correction.
        - Withdraw all results from prior correction step
        - Calculate $\delta\lambda^p$ using equation 2.38.
        - Correct σ, Y_v.
        - Calculate yield- and damage functions f^p and f^d.

This algorithm enables results which are consistent with given conditions for the tolerance regions around damage and yield surface, especially avoiding illegal stress states. The yield surface is the primary variable because this way the coupled plastic-damage case is similar with the purely plastic case and violating the yield surface has found to be more critical for rock behavior.

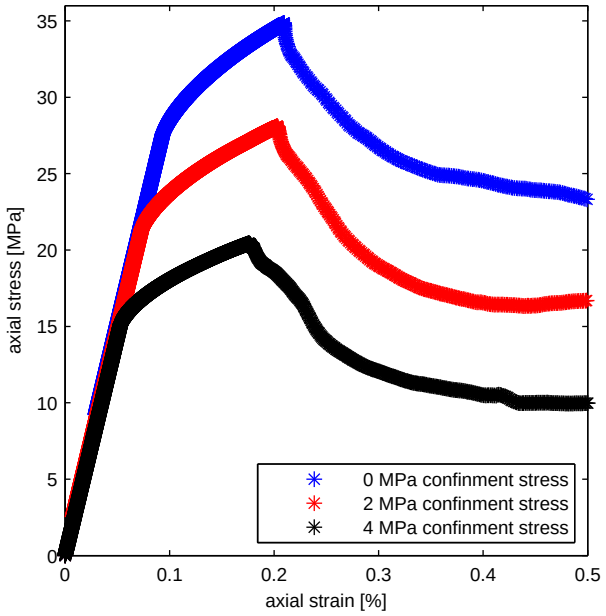

Figure 2.2: Stress- strain curves for compression tests with 0, 2 and 4 MPa confinement stress.

2.5 Results

We compare our simulation to several common experiments with concrete (cf. Wu et al. [2006], Mortazavi and Molladavoodi [2012], Omidi and Lotfi [2010] and others). At first we will present numerical results from confined compression tests and look into more detail of the algorithm.

To study the behavior of geomaterial under confined conditions, tests were simulated with increasing confinement stress of 2MPa and 4MPa on samples with 6cm diameter and 12cm height with a spatial resolution of $1mm^2$. The stress strain response curve is shown in figure 2.2. The material exhibits larger strength with increasing confinement stress, which is in good agreement with experimental observations (e.g. Wawersik and Fairhurst [1970]). We will use these tests to study the behavior of the algorithm in more detail.

Comparing the elastic part with the plastic part of the damage evolution, we see that elastic contributions are negligible as confinement pressure increases (figure 2.3). With larger confinement stress the elastic stresses become less tensile and only tensile volumetric elastic stresses account for damage evolution. The damage operator mainly evolves in the plastic domain, which can also be seen in the two-dimensional distribution of the yield function (figure 2.4). The yield function is within the tolerance region around 0MPa at all points with evolving damage and shows pattern of stress relaxation around the fractures. Looking at a two dimensional distribution of the damage value it can be noticed that the damage operator increases most significantly along fractures and in the surrounding, which are most stressed areas (figure 2.3). The same behavior has been observed in other studies (e.g. Mortazavi and Molladavoodi [2012], Taqieddin and Voyiadjis [2009], Marotti de Sciarra [2012]).

The fracture angle is around 46° following the Roscoe angle (Kaus [2010], Poliakov et al. [1994]).

To evaluate how the algorithm controles drift from the damage surface we focus at the evolution of f^d for a particular grid point (figure 2.5). Two cases are simulated: using the double surface correction algorithm developed in this work and using the same damage model but only applying a correction for the yield surface drift. In early stages, both simulations do not differ as the algorithm is not applied during this period. When the damage function approaches to zero and afterwards the differences become substantial. Without a correction algorithm which considers drift from both surfaces values above the tolerance are computed for the damage function representing an illegal state. This state is hold over a period of several time steps before it reduces. Even in its final stage the damage function is significantly above zero. To decrease computational time we use time scaling.

With double surface correction on the other hand, the damage function remains very close to zero the whole time and only differs significantly from zero for a very short time. Looking at the evolution of the scalar damage operator D in figure 2.6, differences are also visible between both algorithms. Without double surface correction higher values for D are calculated.

We use this algorithm together with the presented rheological model to simulate

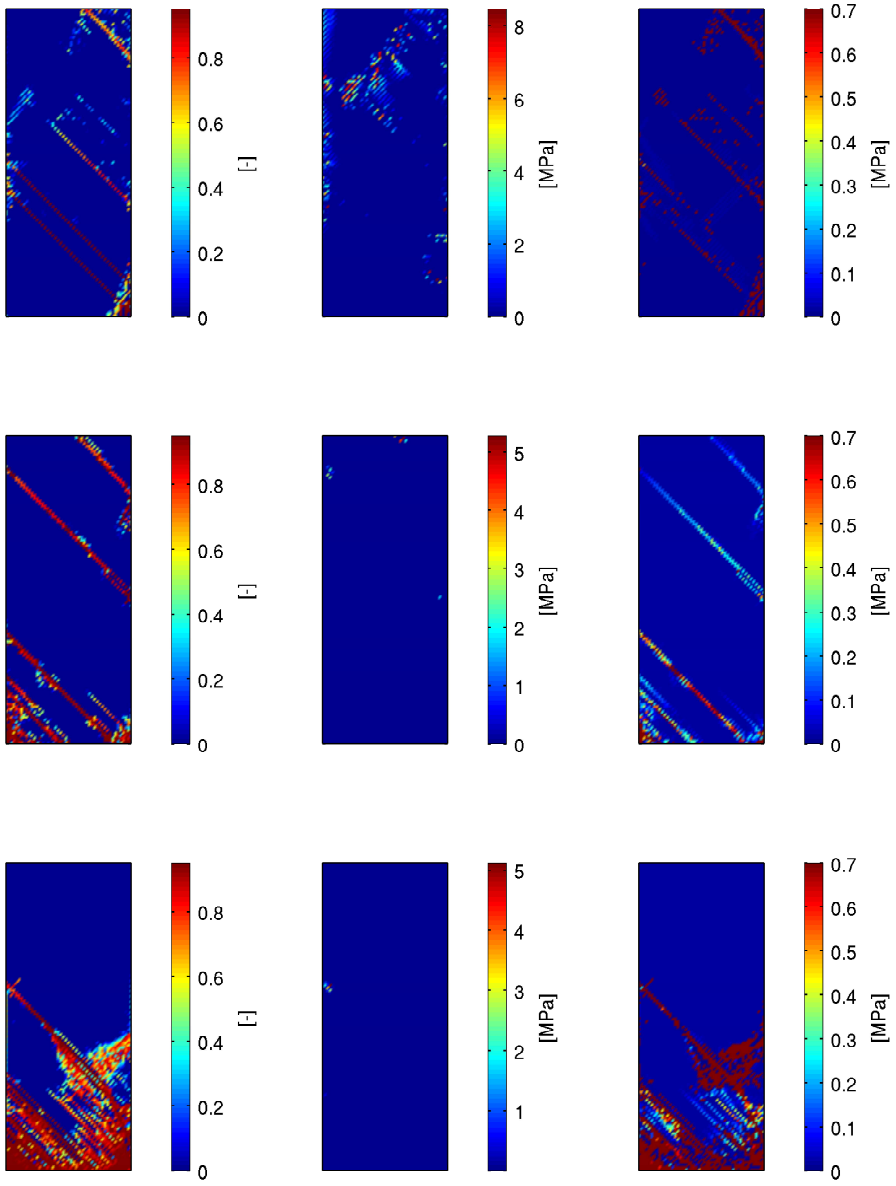

Figure 2.3: Damage growth during a compression test with 0 (top), 2 (center) and 4 MPa confinement stress (bottom). Damage operator (left), elastic and plastic contribution to damage evolution are shown (center and right). The elastic contribution decreases when confining stress increases because the rock exhibits less tensile volumetric elastic strain. The occurrence of the elastic part is arbitrary. The plastic contribution mainly evolves along fractures and their vicinity. Specimen dimensions are 50mm$x$100mm.

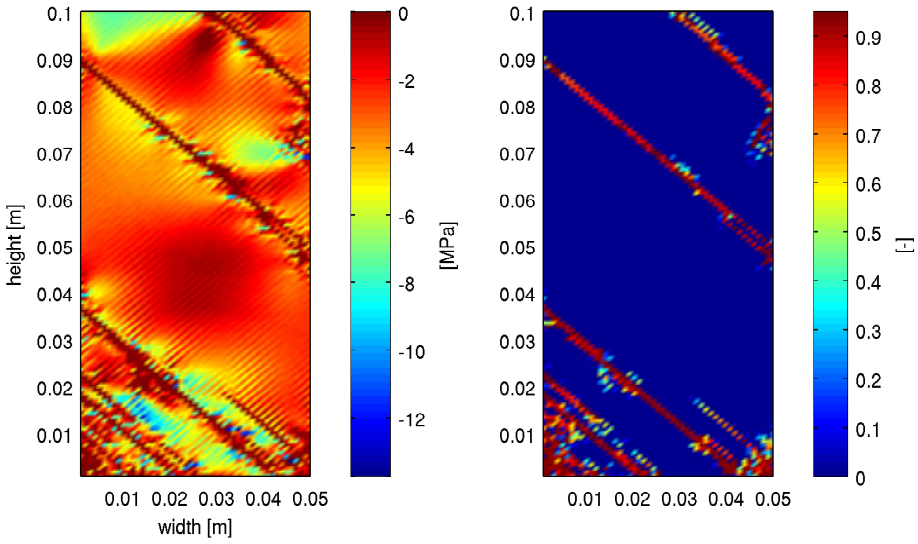

Figure 2.4: Yield and damage function during a compression test with 2 MPa confinement stress. High values of the damage function coincide with a damage operator higher than 0 and strong plastic contributions along the fracture lines and in surrounding areas. Fracture pattern and stress distribution follows the predicted pattern. Stress relaxation can be seen around the fractures which is related to more negative values of the yield function.

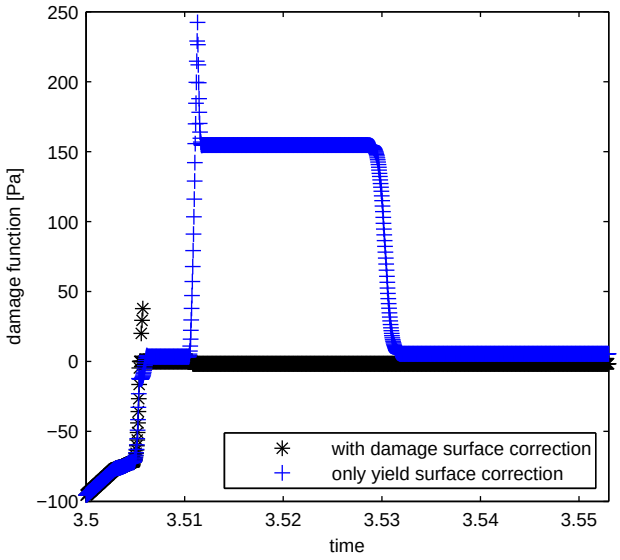

Figure 2.5: Distribution of damage function (in seconds) for one arbitrary grid point with (black line) and without (blue line) applied double- surface correction algorithm. Blue line shows strong divergence from zero over several time steps. For any time step prior to the shown time window both curves are identical. To improve computational time, time scaling is used.

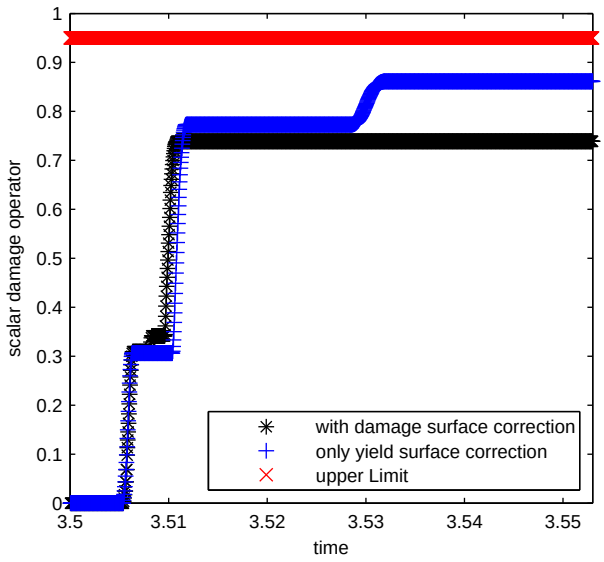

Figure 2.6: Distribution of scalar damage operator over time (in seconds) for one arbitrary grid point with (black line) and without (blue line) applied double- surface correction algorithm. Without double- surface correction significant higher values for the damage operator are computed. Red line indicates damage limit Γ. To improve computational time, time scaling is used.

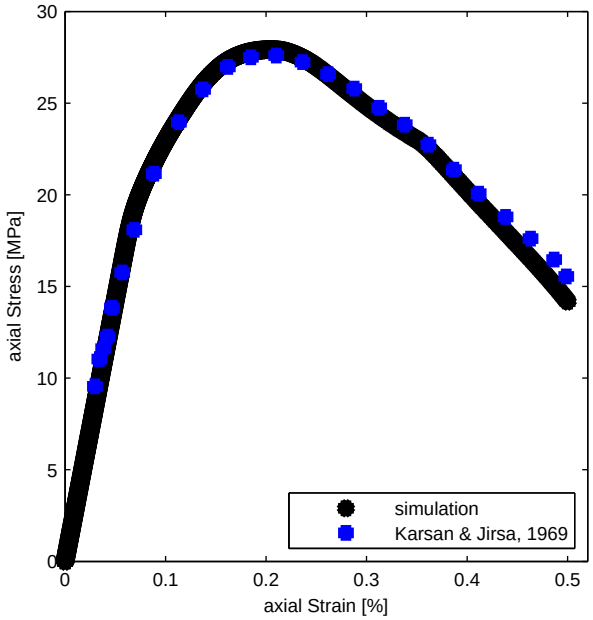

Figure 2.7: Numerical simulation of uniaxial compression of a concrete specimen. Comparison to experimental data from Karson and Jirsa [1969] and numerical model with return algorithm. It can be observed that the results from the numerical model agree with the laboratory ones over hardening and softening regime.

several compresional and extesional experiments on concrete. Our model reproduces the experimental results for a uniaxial compression test on concrete performed by Karson and Jirsa [1969] very well (figure 2.7). The values used as model parameters can be found in table 2.1. The stress- strain response behavior is most complex to model in the non-linear hardening and softening regime after peak stress.

We also test our model with an uniaxial tensional experiment performed by Geopalaeratnam and Shah [1985]. The parameters used are listed in table 2.2. A comparison of the stress strain curves from laboratory measurments and our model can be seen in figure 2.8. For the tensile case an agreement of our numerical model results with the experimental observations can be achieved. Especially the non-linear post- peak behavior is critical for models in the tensile case.

Degradation of elastic properties can be visualized very well during cyclic uniaxial tests. We match our model to the experimental test of Sinha et al. [1964] in which a concrete specimen is uniaxial loaded and unloaded for 9 cycles (figure 2.9). Parameters can be found in table 2.3. As shown in figure 2.9 during loading and unloading the degradation of strength and stiffness as well as the irreversible strains upon unloading, are well reproduced. The strength is slightly underestimated for early stages. We are also able to reproduce the characteristic difference in loading and unloading path for later cycles.

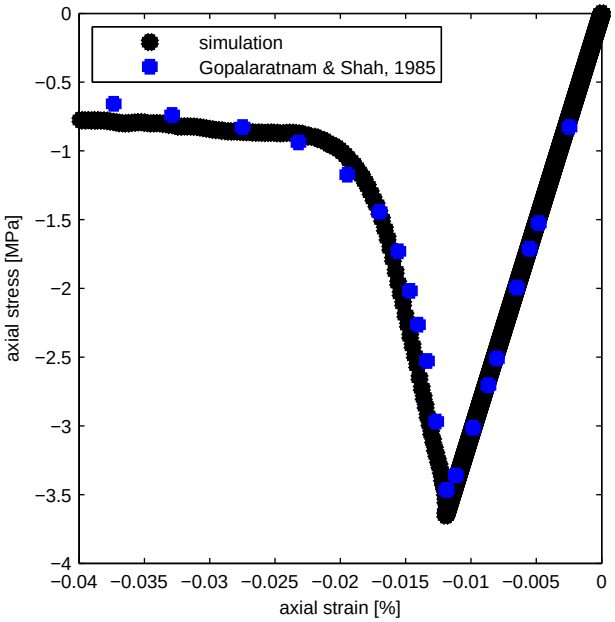

Figure 2.8: Numerical simulation of uniaxial tensile test of a concrete specimen. We achieve a match between experimental data from Geopalaeratnam and Shah [1985] and our numerical model using the return algorithm, especially for post- peak behavior. The experiment is used to test the model behavior in a tensile environment.

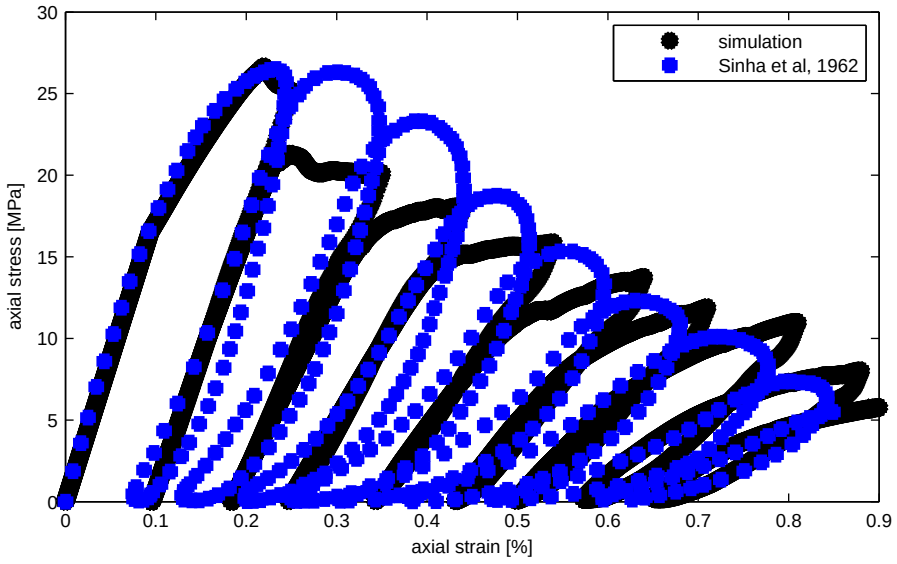

Figure 2.9: Numerical simulation of uniaxial cycling test of a concrete specimen. Match between experimental data from Sinha et al. [1964] and numerical model with return algorithm. Numerical stress strain curve matches experimental one to a high degree. The simulated model slightly underestimates the strength during early cycles. Starting from the second cycle hysteresis in loading and unloadind path can be appreciated and it becomes significant during the last three cycles.

E_0	ν	ϵ_f	ϵ_c	p	c	r_0
29.5GPa	0.19	0.012	0.001	0.01	0.1	2080

Table 2.1: Rock properties used in our numerical simulation for simulating the uniaxial tensile test from Geopalaeratnam and Shah [1985].

E_0	ν	ϵ_f	ϵ_c	p	c	r_0
27.5GPa	0.19	0.0017	0.022	0.01	0.1	3308

Table 2.2: Rock properties used in our numerical simulation for simulating the uniaxial compression test from Karson and Jirsa [1969].

E_0	ν	ϵ_f	ϵ_c	p	c	r_0
17GPa	0.19	0.0005	0.115	0.01	0.1	7000

Table 2.3: Rock properties used in our numerical simulation for simulating the uniaxial cycling test from Sinha et al. [1964].

2.6 Discussion and Conclusion

In this paper we present an explicit algorithm for the computation of elasto plastic damage models. Stress and strain values as well as spatial distribution of the scalar damage operator are in agreement with findings by other authors, numerically and experimentally. We tested our model for various scenarios and achieved a good agreement with experimental data. The uniaxial compression test could be reproduced very well during elastic and plastic domain, especially including the hardening and softening regime. We also simulated a tensile loading test and again model and experimental stress- strain curve matched well. The post- peak behavior is important in these kind of tests and experiment as well as simulation give similar results. We finally test the behavior of our model with a uniaxial cycling test of concrete. In these tests the damage evolution can be observed directly by the slope of the loading and unloading curve. Our model reproduces this test to a high degree. The underestimation of strength at early stages could be overcome by applying a more suitable yield function for concrete (cf. Salari et al. [2004], Wu et al. [2006]). In addition to other models we are also able to simulate the hysteresis in the loading and unloading path during cycles. To the best of our knowledge no other present model is able to reproduce hysteresis. It remains to examine further how this influences results for simulations above laboratory scale.

The two- dimensional analysis shows that the evolution of the damage operator is concentrated around fractures and highly deformed areas. This is in agreement with other numerical simulations (e.g. Taqieddin and Voyiadjis [2009]). Elastic contributions for damage evolution during compression tests vanish with increasing confinement pressure and increased load. Plastic contributions are therefore dominant in all simulated tests, compressive as well as tensile ones.

In this work we derive a consistent return algorithm considering numerical drift from yield- and damage function. While ignoring numerical drift from the damage

yield surface is a common practice in numerical rock mechanics, we show that in strongly coupled double surface models this may lead to an overestimation of the damage variable and a consequent overestimation of the elastic degradation. To avoid this, algorithms that return the values of the stresses and damage variable to the yield functions must be applied. The presented algorithm is able to prevent numerical drift from damage and yield surface and avoids illegal damage states for compressional and tensional cases.

Acknowledgment

We thank the German Research Foundation, Deutsche Forschungsgemeinschaft (DFG), for the financial support through the project no. MI 1237/7-1 and the VW foundation through the grant 'Extreme Events'.

Chapter 3

A new method to estimate the occurrence and magnitude of simulated rock failure events

Abstract

Predicting failure is one of the primary objectives in the mechanical description of geomaterials. Many different methods have been developed on laboratory and field scales to measure, identify and isolate trademarks or characteristics of the failure process. At the laboratory scale, identifying and localizing acoustic emissions (AE) is a common method for the short term prediction of failure. Above average AE typically precedes the failure process and is easily measured. At larger scales, increase in micro-seismic or seismic activity sometimes precedes large earthquakes (e.g. Tohoku, L'Aquilla, oceanic transforms), and can be used to assess seismic risk. The goal of this work is to develop a methodology and numerical algorithms for extracting a measurable quantity analogous to AE arising from the solution of equations governing rock deformation. Since there is no physical quantify of AE derivable from the governing equations, then an appropriate rock-mechanical analog has to be found. In this work, we identify a general behavior of the AE generation process preceding rock failure. This behavior includes an arbitrary localization of low magnitude events during the pre-failure stage, followed by increases in both the number and amplitude, and finally localization around the incipient failure plane during macroscopic failure. We propose deviatoric strain rate as the numerical analog that mimics this behavior, and develop two different algorithms designed to detect rapid increases in deviatoric strain using short-term and long-term moving averages.
The numerical model solves a poro- elasto- plastic continuum model and is coupled to a two- phase flow model using Richards approximation. We test our model by comparing simulation results with experiments of an uniaxial compression and of fluid injection into critically stressed probes. We find for both cases that the occurrence and amplitude of our AE analog mimics the observed general behavior of the AE generation process. Our technique can be extended to the field scale, thus providing a mechanistic basis for seismic hazard assessment.

3.1 Introduction

Understanding failure and rupture processes in geomaterials is one of the primary goals in earth sciences and engineering. Actively inducing seismicity is finding many applications in enhanced geothermal systems and the extraction of hydrocarbons from tight shales, while natural seismicity has long been studied to try and understand the earthquake process and behaviors indicative of impending failure in a large event. A variety of studies at the field scale focused on the interaction between fluid (and fluid pressure) propagation and location of seismic events (e.g. Mayr et al. [2011], Baisch et al. [2010], McClure and Horne [2010]), with acoustic emissions (AE) acting as their laboratory scale equivalent. Acoustic emissions and seismic events have similar source mechanisms, but a different range of frequencies (Mogi [1967], Cai et al. [2007]), while both often precede and accompany plastic deformation and changes of mechanical properties. Observations of seismic and acoustic events are utilized as a predictor of rock failure and rock burst (e.g. Lockner [1993], Pettitt et al. [2002]). Modern laboratory techniques allow the detection and localization of acoustic emissions at very high rates and accuracy, with the rate of recorded signals increasing from hundreds to thousands of events per second over the last few years (e.g. Stanchits et al. [2011], Amitrano [2003]). Acoustic emissions analysis is performed on wide range of materials, including metals (e.g. Farrelly et al. [2004], Marfo et al. [2013], Aggelis et al. [2011], Huang et al. [1998], Sind et al. [2012], Oh and Han [2012]), ceramics (e.g. Mei et al. [2013], Maillet et al. [2014], Aggelis et al. [2013], Yonezu and Chen [2014], Drozdov [2014], Drozdov [2013]), polymers (e.g. Sause et al. [2013],Berdowski et al. [2013], Fu et al. [2014], Hamdi et al. [2013], Njuohvic et al. [2014], Boominathan et al. [2014], Burks and Kumosa [2014]), and concrete (e.g. Zhu et al. [2010], Itturrioz et al. [2013], Elfergani et al. [2013], Ohno et al. [2014], Hu et al. [2013], Kencanawati et al. [2013], Kawasaki et al. [2013], Shahidan et al. [2013], ElBatanouny et al. [2014]).

AE can not be derived directly from physical properties in numerical simulations, so analogs are needed. Some theoretical approaches exist for discrete element modeling (DEM), where the material is represented by discrete bonded particles that interact with each other, and exceeding the bond strength is used as the AE analog (e.g. Kun et al. [2014], Hazzard et al. [2002], Hazzard and Young [2002], Hazzard and Young [2004]). However, DEM are computationally expensive, and have no inherent length scale necessary to quantitatively compare with observations, thus limiting their utility.

Continuum formulation of the underlying mechanics has the advantage that most of the parameters can be obtained form experimental data, however, an appropriate AE analog must still be found. Some methods have been proposed to characterize AE in continuum mechanical models, such as the evolution of a damage function acting on the elastic properties of the rock material (e.g. Amitrano et al. [1999], Amitrano [2003], Fang and Harrison [2002], Lyakhovsky et al. [1997], Tang [1997], Tang and Kaiser [1998], Wang et al. [2012]). For simple fluid-rock interactions, an event is registered if the pore pressure exceeds some predefined critical value (e.g. Parotidis et al. [2003], Parotidis et al. [2005]), while for simple plastic models and

event is registered by reaching the yielding point in a numerical grid cell (e.g. Baisch et al. [2010], McClure and Horne [2010]). However, in more advanced rheological models that include frictional hardening, cohesion softening and damage effects, the yield function is insufficient because it does not reproduce important characteristics of AEs.
In this paper we propose the deviatoric strain rate as an indicator of local failure, and as an analog of acoustic emissions. The deviatoric strain measures distortion with no volumetric change, thus identifying shear movement. Any rapid shear movement is commonly referred to as slip, and in the plastic regime, it indicates fracture generation or growth. This is the mechanistic source for acoustic emissions, so a natural link between deviatoric strain and acoustic emissions is proposed. In addition, since deviatoric strain is a common rock- mechanical value that can be easily calculated, no new ad-hoc rock-mechanical parameter needs to be introduced. We use a continuum mechanical model that includes poro- elasto- plasticity, frictional hardening, cohesion softening and damage effects, and solve the governing equations using a finite difference approximation. The results of the numerical simulation are analyzed and compared with experimental data for dry compression and high pressure fluid injection in a sandstone sample. We identify the location, the evolution over time, and the amplitude of AEs, and show very good comparison with experimental data.

3.2 Rheological Model and Fluid Flow

3.2.1 The poro- elasto- plastic model

Elastodynamic equations in their velocity-stress form describe the elastic response of a rock skeleton in two dimensions

$$\frac{\partial V_x}{\partial t} = \frac{1}{\rho}(\frac{\partial \sigma_{xx}}{\partial x} + \frac{\partial \sigma_{xy}}{\partial y}) \tag{3.1}$$

$$\frac{\partial V_y}{\partial t} = \frac{1}{\rho}(\frac{\partial \sigma_{yy}}{\partial y} + \frac{\partial \sigma_{xy}}{\partial x}) \tag{3.2}$$

$$\frac{\partial \sigma_{xx}}{\partial t} = (\lambda + 2\mu)\frac{\partial V_x}{\partial x} + \lambda \frac{\partial V_y}{\partial y} \tag{3.3}$$

$$\frac{\partial \sigma_{yy}}{\partial t} = \lambda \frac{\partial V_x}{\partial x} + (\lambda + 2\mu)\frac{\partial V_y}{\partial y} \tag{3.4}$$

$$\frac{\partial \tau_{xy}}{\partial t} = \mu \left(\frac{\partial V_x}{\partial x} + \frac{\partial V_y}{\partial y} \right) \tag{3.5}$$

with μ and λ as Lamé constants, ρ as density, V_x and V_y as velocities and σ_{xx}, σ_{yy}, τ_{xy} form the stress tensor.
In saturated porous rock, where pores form a connected network, deformation is controlled by the Terzaghi effective stress

$$\sigma_{ij}^{eff} = \sigma_{ij} - P\delta_{ij}. \tag{3.6}$$

Plastic deformation of rocks is modeled using Mohr-Coulomb criteria

$$F = \tau - \left(\sigma_m - \frac{C^*}{tan(\varphi^0)}\right) \cdot sin(\varphi^*) \tag{3.7}$$

where F is the yield function, C^* is mobilized cohesion, φ^* is mobilized internal frictional angle,φ^0 is maximal internal frictional angle, τ is stress deviator, σ_m is mean stress.
Cohesion and internal friction angle are mobilized in terms of a cohesion weakening and frictional strengthening model dependent on effective plastic strain $\bar{\epsilon}_p$ Hajiabdolmajid et al. [2002]. Mobilized values for friction angle, cohesion and dilatancy angle are calculated following Vermeer and de Borst [1984] and are dependent on effective plastic stress.
Plastic strain rates are given by

$$\dot{\epsilon}_{ij}^{pl} = 0 \text{ for } F < 0 \text{ or } F = 0 \text{ and } \dot{F} < 0 \tag{3.8}$$

$$\dot{\epsilon}_{ij}^{pl} = \lambda^p \frac{\partial q}{\partial \sigma_{ij}} \text{ for } F = 0 \text{ and } \dot{F} = 0. \tag{3.9}$$

with λ^p is the plastic multiplier and q is the flow rule.
Effective plastic strain $\bar{\epsilon}_p$ follows from there

$$\bar{\epsilon}_p = \sqrt{\frac{2}{3}\dot{\epsilon_p}^T \cdot M \cdot \dot{\epsilon_p}} \tag{3.10}$$

where M is a weighting matrix Abbo [1997].
We use non-associative plastic flow rules Vermeer and de Borst [1984]

$$q = \tau - \sigma_m \cdot sin(\psi^*) \tag{3.11}$$

where ψ^* is the mobilized dilatancy angle Vermeer and de Borst [1984].
Degradation of elastic properties dependent on a damage operator D is described by

$$E^d = (1 - D)E^0 \tag{3.12}$$

where E is the elasticity tensor in damaged E^d and undamaged E^0 state. The evolution of D is modeled following the method described in Peerlings et al. [1998].

3.2.2 Two phase flow

Fluid flow is considered as an isothermal water-gas immiscible mixture with no phase transitions and is modeled using Richards approximation. In the context of water intrusion in an unsaturated regime the air reservoir is infinite, so air pressure is the zero reference Richards [1931]. Darcy velocity in a multiphase environment can be generalized for any phase $\alpha = w, a$

$$v_\alpha = \frac{-k_\alpha k_0}{\mu_\alpha} \nabla P_\alpha \tag{3.13}$$

where k_0 is intrinsic permeability, μ_α is phase viscosity, k_α is phase permeability and P is pressure. Phase permeability varies between 0 and 1. It can be linked to the saturation S using vanGenuchten relationships, which show very good agreement with experimental data for water and air mixture (Cropper et al. [2011],vanGenuchten [1980]).

$$\begin{aligned} k_w &= \sqrt{S_w}\left(1-\left(1-S_w^{\frac{1}{m}}\right)^m\right)^2 \\ k_a &= (1-S_w)^2 \cdot \left(1-S_w^{\frac{2+3m}{m}}\right) \end{aligned} \tag{3.14}$$

The Richards equation remains.

$$\frac{\partial P_w}{\partial t} = \frac{1}{\phi\left(S_w \cdot c_w + \frac{\partial S_w}{\partial P_w}\right)} \nabla\left(\frac{k_w k_0}{\mu_w} \nabla P_w\right) \tag{3.15}$$

3.3 Algorithm to detect an analog for AE during continuum numerical simulations

Frictional movement along preexisting cracks or generation of new fractures generate acoustic emissions during plastic deformation in laboratory scales (Fortin et al. [2009], Zang et al. [1996], Lisjak et al. [2013]), while the same processes generate seismic events in field scales. Therefore, acoustic emissions behave similar to seismic events in many characteristics like propagation, energy release and generation mechanisms but differ in frequencies of seismic waves (Cai et al. [2007]).
Seismic wave amplitude is correlated to seismic moment Itturrioz et al. [2013], where the scalar seismic moment is defined as

$$M_0 = G \cdot A \cdot u \tag{3.16}$$

where G is the shear modulus, A the area of the shear plane and u the displacement and seismic moment magnitude is determined by the empirical relation

$$M_w = \frac{2}{3}\log_{10}(M_0) - 6 \tag{3.17}$$

Estimating seismic moment in a numerical simulation requires determining only the area of slip A and displacement u because the shear modulus is known. In a finite difference scheme, the smallest area of slip that can be resolved is the grid cell size $dx \cdot dy$ with an incremental distance dx and dy between nodes in the $x-$ and $y-$ direction. The total area of an event will be given by the combined area of the cells that fail in a common spatial and time window. We make the spatial constraint that only immediate neighbor cells can combine their areas because stress transfer can trigger failure from one cell to the immediate neighborhood. The slipping region can propagate from one cell to the others and generate a cluster of simultaneously failing. We add the area of all cells of this cluster and define a spatial window. We

define an excitation time window as the time span from the initial slipping of one cell of the cluster until the end of the slipping of the last excited cell of the cluster. During this time new areas are combined to one common event (see figure 3.1). Anything outside this time window is counted as a separated event. It is certainly true that slip anywhere transfers stress to the immediate neighborhood and can trigger further slip, but if this new event is not within certain time window, it is registered a separate events the slip do not contribute to the magnitude of the prior event.

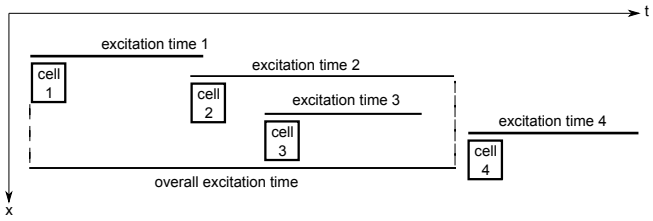

Figure 3.1: Defining the excitation time window for a simplified 1d case. Cell 1 starts to slip, which triggers cells 2 and 3. The excitation time of cell 4 does not overlap with one of its neighboring cells, and is considered a single event, Slip of the cells 1, 2 and 3 are recorded as one joint event.

The essential purpose of our model is to detect of an event and to determine the amount of slip. We propose the deviatoric strain rate as an analog to AE because high deviatoric strain rates indicate shear failure. Deviatoric strain is defined as:

$$\epsilon_{dev} = \sqrt{\frac{(\epsilon_{xx} - \epsilon_{yy})^2}{4} - \epsilon_{xy}^2} \tag{3.18}$$

where ϵ_{ii} are normal strains and ϵ_{ij} are shear strains. We use the deviatoric strain rate to identify rapid changes in the deviatoric strain and to isolate discontinuous events from continuous deformation. Figure 3.2 shows the deviatoric strain, the deviatoric strain rate, and the yield function of one grid point over a time span that we identify as an event (shaded time window). The deviatoric strain rate shows a clear peak, followed by a longer phase of above average rate activity, while simultaneously the deviatoric strain significantly increases. The yield function of the grid point falls well below zero shortly after the event, indicating elastic deformation following a long period of plastic deformation during the event. This decrease in the yield function is due to stress drop in the cell associated with shear displacement. We view this substantial reduction in the yield function as a primary argument that the increase in deviatoric strain signals failure and can thus be used as an AE analog. Other continuum mechanical models that include acoustic emissions do not have this intrinsic feedback between acoustic emission and the stress state.
No measurable change in the yield function is observed at the onset of slip, but rather small variations (figure 3.2). These high frequency oscillations of the yield function around zero are a result of the applied algorithm to prevent a drift from the yield surface (e.g. Abbo [1997], Potts and Gens [1985]). It is not used in the

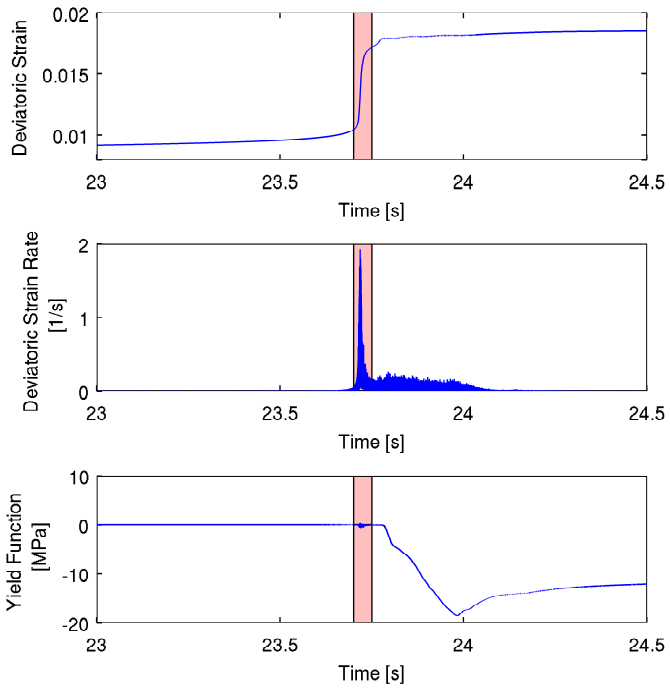

Figure 3.2: Deviatoric strain, deviatoric strain rate and yield function over time of one grid point during a rapid shear movement (marked region).

detection algorithm at any point and does not have any physical meaning. It is purely numerical noise.

We apply an algorithm that uses a moving average to identify periods of high deviatoric strain rate. In this method, a short term average (STA) covers a time span of a part of the length of an expected event, and a long term average (LTA) that is considerably longer than the expected event duration. If the ratio

$$q = \frac{STA}{LTA} \tag{3.19}$$

exceeds a given limit q_{limit}, then an event is detected. With an appropriate choice of the length of STA and LTA, in combination with a value for q_{limit}, events can be detected. This method ensures that the increase in deviatoric strain is rapid and thus signals failure.

To determine the slip, the beginning and the end of the excitation time window needs to be evaluated. After the peak in the q ratio is found, single points before this peak are tested. For this we compute the ratio q_p of the previous point until we find the first point for which the q_p ratio is above a different limit q_{start}. This point in time is chosen as starting point of the slip. When q drops below another limit q_{end}, we set the end of the time window. In many cases we found it sufficient to choose $q_{\text{start}} = q_{\text{end}}$. Any point inside this time window (and belonging to the clusters of immediate neighbors) contributes to the total slip of the event (see figure 3.3),

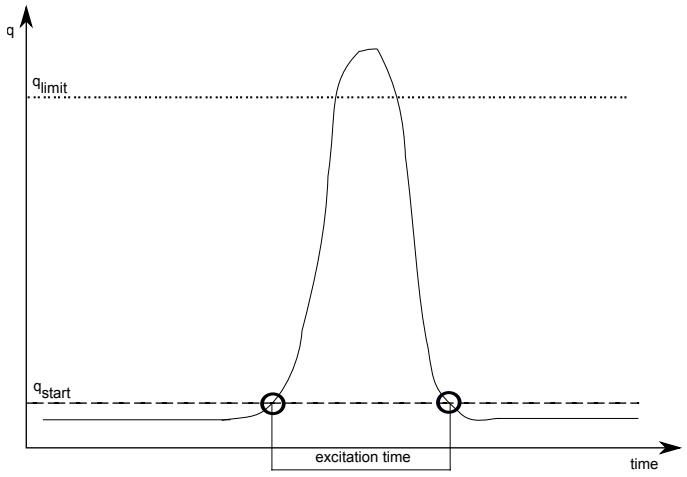

Figure 3.3: Defining the excitation time window for one cell. Initially the peak is detected with the STA / LTA ratio q of the deviatoric strain exceeding a defined limit. The start and end points of the slip are found with a much lower limit value. The time during start- and end point gives the excitation time window during which all displacement is summed up for this slip event.

$$u = \int_{t_{start}}^{t_{end}} v dt \tag{3.20}$$

with displacement u, velocity v and incremental time step dt.
We found this method to be very reliable and robust for detecting rapid changes in deviatoric strain rates. However, the correct setting of the two limits, q_{limit} and $q_{\text{start}} = q_{\text{end}}$, is necessary to achieve good results. A high q_{limit} ensures that only real events are detected as opposed to noise. A low $q_{\text{start}} = q_{\text{end}}$ on the other hand enables proper accounting of the entire slip event. These limits, once determined, are stable against variations of the setup such as changes in boundary conditions. However, this method is computationally expensive in both memory usage and processing because for every cell the LTA and STA values have to be stored with some significant length. The LTA requires significantly more values than the slip itself, and the algorithm is computationally intensive due to many arithmetic operations and conditionals.
A faster method with less consumption is to compare the of values of deviatoric strain at consecutive time steps. It is even possible to compare the values within a suitable time period that reduces computational processing costs even further. Comparing consecutive values of the deviatoric strain is equivalent to the mean deviatoric strain rate. If the difference between the two values at consecutive times exceeds some predefined number, an event is detected. The first time step at which the difference exceeds a predefined value is chosen as the starting point of the excitation time and as soon as the difference drops below the limit the end of excitation time is reached (see figure 3.4). Slip during this event can be determined in a similar way to the first method. This second method is substantially faster with smaller memory demands because for each cell only one additional value, the deviatoric strain of the

previous step, has to be stored. This algorithm is also computationally simple as it contains only one condition to be tested. However as only one condition remains, this algorithm is more sensitive to the chosen limit value as the same value is used for detecting a peak at all and determining the excitation time, which influences the magnitude. The value needs to be high enough so noise is not considered but also low enough to cover the whole peak from start to end point. Both algorithms can be adjusted to give similar results with the limit value of the later algorithm being between the limit values of the more complex algorithm.

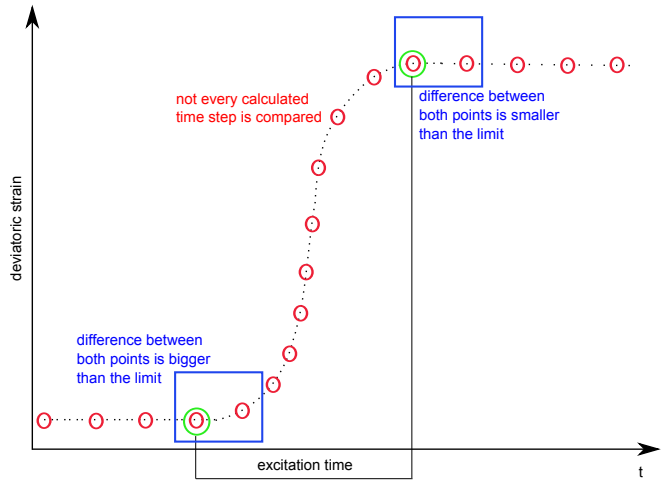

Figure 3.4: Defining the excitation time window for one cell with the faster method. Consecutive values of the deviatoric strain are compared. Not every computed value (black dots) needs to be compared but equally spaced and narrow ones (red circles). The slip event starts when the difference between two values exceeds a given limit. Excitation time continues until the difference between two values again drops below the limit.

Detecting failure of a cell during the computation allows other feedback to be dynamically included, such as permeability increases at the onset of slip, frictional heating, or other slip-dependent processes.

3.4 Numerical experiments and results

We apply our theoretical and numerical model to two high resolution laboratory experiments of hydraulic fracturing of critically stressed rock samples (Stanchits et al. [2011], Mayr et al. [2011]). In these experiments acoustic emissions (AE) were registered and located using high precision ultrasonic tomography to link AE to a propagating fluid front. Such correlations between the fluid front and AE had not previously been achieved in comparable experiments. The tests were performed on samples of Flechtingen Sandstone, which can be assumed to be isotropic. Further details are found in Backers [2004], Stanchits et al. [2011], Blöcher et al. [2009]. For the injection experiments, water was directly applied to the bottom of the specimen, while the top of the specimens was sealed (Mayr et al. [2011]).

We compare our model results with a confined compression experiment and a fluid injection in an undrained, critically stressed specimen.
We numerically solve the governing equations using a two dimensional finite- differences scheme with a staggered grid (Saenger et al. [2000]). The model setup is chosen to match the experimental setup described in Stanchits et al. [2011]. The numerical model has a spatial resolution of 1mm distance between grid points in each direction.

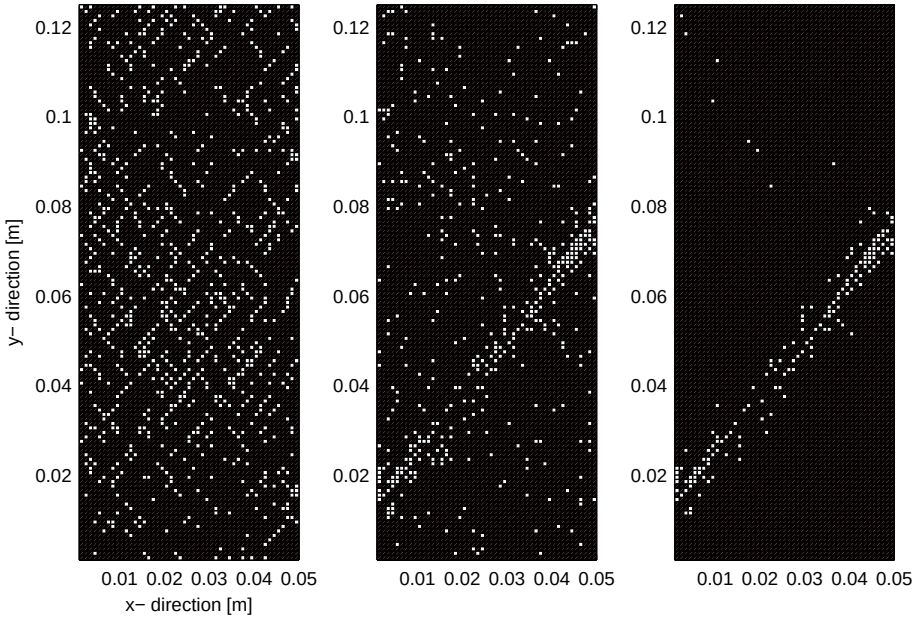

Figure 3.5: Spatial distribution of events over the specimen at different times. The left figure shows events at an early stage that are randomly distributed through the domain. The middle picture shows a localization of events around macroscopic failure, which is clearly visible in the right picture showing events registered in the last stage of the experiment at macroscopic failure. White points indicate cells with at least one event registered during the time span.

3.4.1 Confined compression

In the first part of the experiment, a specimen was compressed with 40MPa confining pressure and a variable axial load until the onset of macroscopic failure, followed by unloading. The simulation results agree with the experimental data in stress-strain path, volumetric and inelastic strain as well as fracture nucleation and propagation (Heinze et al. [2015b]).
Dry compression experiments reveal several features of AE genesis (Stanchits et al. [2011], Fortin et al. [2009], Lyakhovsky et al. [1997], Amitrano et al. [1999]) that must necessarily be reproduced by a numerical simulation analog, including:

- Arbitrary locations in first stages of compression;

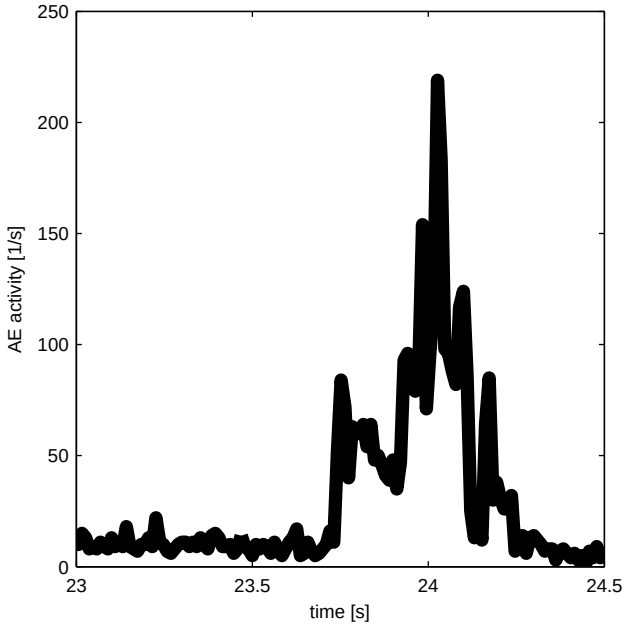

Figure 3.6: Rate of occurrence of acoustic emissions at macroscopic failure. The activity increases suddenly and stays above average during the development of the macroscopic failure plane. This is followed by a decline to normal activity.

- Localization surrounding the incipient macroscopic failure plane;
- A rapid increase in the rate of occurrence during macroscopic failure, followed by a rapid decline;
- A rapid increase in AE amplitude during macroscopic failure, followed by a rapid decline.

We reproduce all four of these features in our numerical simulations. We find that events detected in the early stages of compression are randomly distributed, and followed at later stages by localizing around the failure plane and then predominantly along the failure plane (figure 3.5). The first emissions are triggered at weak points introduced by a heterogeneous distribution of cohesion and internal friction angle. The number and magnitude of events signal the onset of macroscopic failure, with the number of events increasing rapidly and concentrating around the failure plane (figure 3.6). Many events occur because stress concentrates around the fracture plane, so many numerical grid points nearby each other simultaneously reach a critical state. For the same reason, events have a larger magnitude because many grid points are slipping simultaneously resulting in a larger slip event. As neighboring cells reach failure, an event is more likely to trigger failure of its neighbors during its own excitation time so cells combine for one single joint event (figure 3.7).

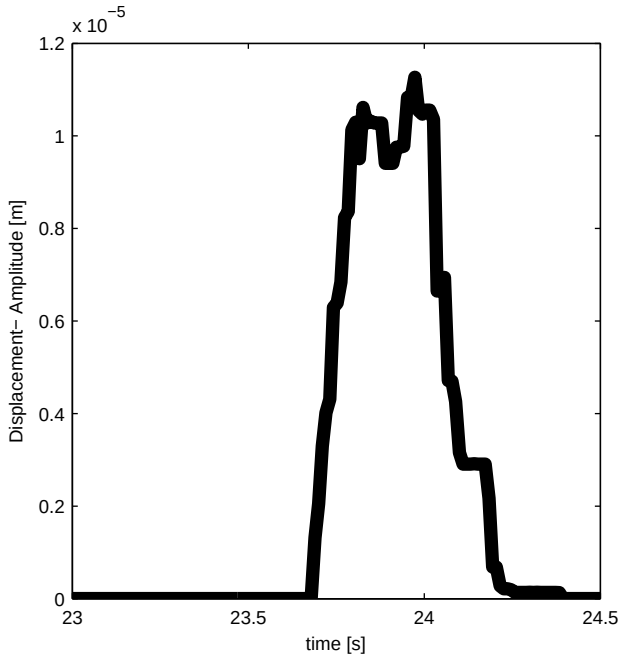

Figure 3.7: Magnitude of detected events over time at the moment of macroscopic failure. The magnitude increases rapidly and stays high while macroscopic failure is ongoing and propagating through the specimen. It declines abruptly after the fracture is completed.

3.4.2 Fluid injection in an undrained rock

Fluid injection into a host rock is widely used in enhanced geothermal systems, waste disposal, CO2 sequestration, and fracking. In each of these processes, acoustic emissions (e.g. seismicity) is used as a measure of fluid front and is thus of great interest. We further test our numerical AE analog with observations from an experiment where a rock specimen was sealed at the top and a fluid pressure boundary of 5MPa was applied to the bottom boundary. The experiments showed a clear correlation between the propagating fluid front and location of acoustic emissions (Stanchits et al. [2011]), with AEs mostly detected below or close to fluid front and very few events in the upper part of the specimen. Field observations show a similar correlation between (micro-) seismic events and estimated fluid front (e.g. Shapiro et al. [2003]).

Realistic fits between numerical simulation and experiments require that the fluid behavior be reproduced. In experiments, the fluid front is estimated from the injected volume and fitting the solution of a linear diffusion equations to the AE (Stanchits et al. [2011], Mayr et al. [2011]). On field observations like at geothermal plants the fluid front is estimated from the occurrence of seismic events (e.g. Shapiro et al. [2003], Parotidis et al. [2003]).In the numerical simulation we determine the fluid front from the saturation equation, and for the simulated experiment the fluid front in the numerical model agrees well with that estimated from the injected volume, and differs a little from the fluid front derived from the linear diffusion equation solution (figure 3.8 and Stanchits et al. [2011]).

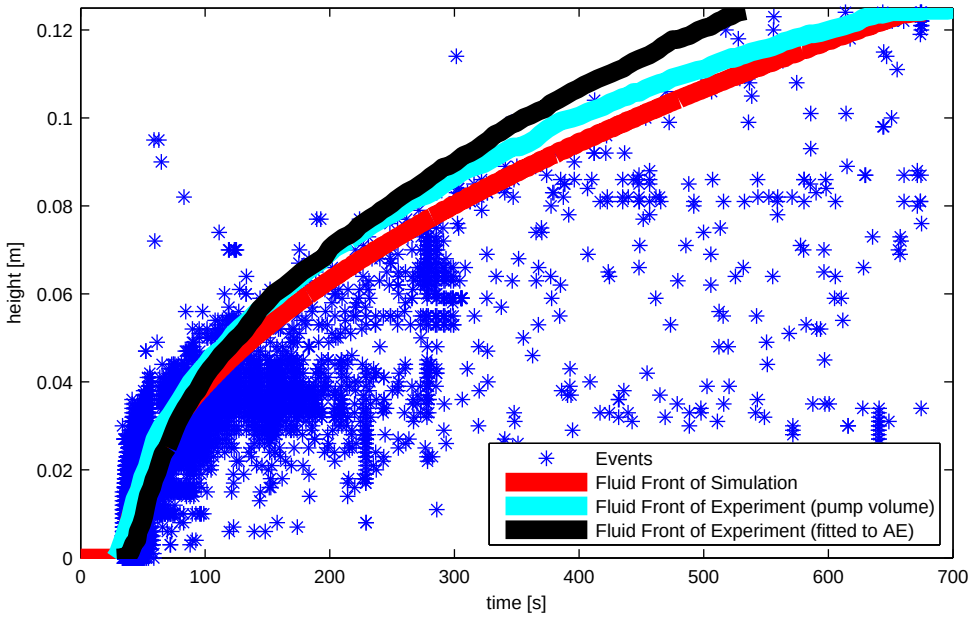

Figure 3.8: Events occurring during fluid injection obtained from the numerical simulation. The behavior agrees very well with the results from laboratory experiments and from field observations (cf. Stanchits et al. [2011], Shapiro et al. [2003]). Many events at the bottom are induced as fluid is injected because the rock is critically stressed and fluids and poro-elasticity redistributes the stresses. Only a few events are registered above the fluid front, and fewer events occur with time. A general stress drop in the specimen due to fluid injection results in a non-critically stressed specimen at later times.

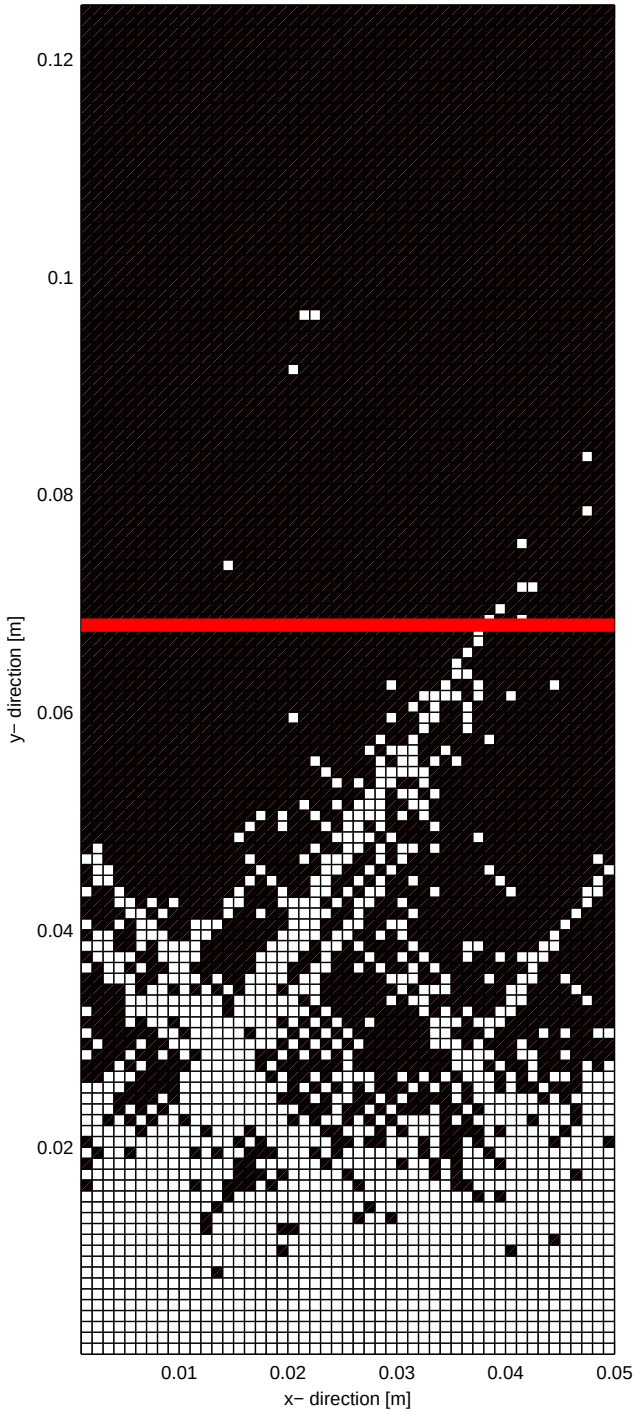

Figure 3.9: Points indicate cells that recorded at least one numerical AE. Micro- fractures below the fluid front (red line) are clearly visible, and only a few events are observed above the fluid front.

A clear correlation between the fluid front and the occurrence of events can be observed in our simulations and in the experimental measurements (figure 3.8). Only few events take place in the upper part of the specimen and also at the bottom for later times. This is identical to field and laboratory data. In figure 3.9 this is also clearly visible. The red line marks the fluid front and micro- fractures can be identified below the fluid front due to the cells which signaled an event. The events are triggered by the fluid pressure propagating through the specimen from bottom to top. Fluid injection leads to a general stress drop inside the specimen, so after some time the specimen is no longer critically stressed and the event rate subsides. Additionally, if the maximum fluid pressure is reached in a spatial region of the specimen, failure is unlikely until higher fluid pressures are applied.

3.5 Discussion and Conclusions

We propose deviatoric strain rate as an AE analog value to detect rapid, plastic deformation along preexisting cracks and the generation of new fractures. With this method, we can locate events and determine their seismic moments during the simulation. We apply this numerical AE detection method to a fully coupled poro- elasto-plastic continuum model that incorporates frictional hardening, cohesion weakening and damage effects. We compare the results of our method with experimental data from a confined compression experiment of an undrained specimen, and with fluid injection in a critically stressed specimen. Both experiments can be reproduced in stress- strain behavior and fluid movement as well as in occurrence and amplitude of AEs (Heinze et al. [2015b]).
We present two different approaches for implementing the method, and both approaches produce similar results when adjusted accordingly.
During dry compression, our numerical AE (e.g. deviatoric strain rate) occur randomly throughout the model early in the loading, followed by localization around the macroscopic failure plane, similar to experimental observations (Lockner [1993]). Both the amplitude and the number of numerically recorded AE increases significantly during macroscopic rupture. AE occur during fluid injection near the fluid front and behind the front, and fade after maximum pressure is reached, results similar to experimental and field observations. (Stanchits et al. [2011], Shapiro et al. [2003]).
These methods are easily adaptable to other simulations and numerical implementations, and we will extend these results to field scale experiments that might allow mechanistic assessment of seismic hazard through a determination of earthquake magnitude.

Acknowledgment

We thank the German Research Foundation, Deutsche Forschungsgemeinschaft (DFG), for the financial support through the project no. MI 1237/7-1 and the VW foundation through the grant 'Extreme Events'.

Chapter 4

Numerical Simulation of the 2008 Bohemian Earthquake Swarm

Abstract

CO_2 has long been suspected of driving the Bohemian earthquake swarms because of the migrating nature of the swarms and expressions of CO_2 degassing at the surface. Modelling to date primarily employed linear diffusion models, but more sophisticated modelling that includes mechanics has been lacking. In this paper, we apply a model that couples mechanics to heat and flow of a super-critical CO_2 through a fracture network. We present a continuum mechanical approach to derive the seismic moment magnitude using the deviatoric strain as an indicator of rupturing processes during individual events. We use a peak- detection algorithm to identify rapid changes in deviatoric strain, indicative of slip events. This method has been shown to work very well in dry and fluid-induced fracturing experiments at the laboratory scale, and in this work we extend the method to the scale of the West Bohemia / Vogtland earthquake swarms. We show very good agreement between model results and observations of the 2008 swarm, further supporting the hypothesis that the Bohemian earthquake swarms are predominately fluid-driven.

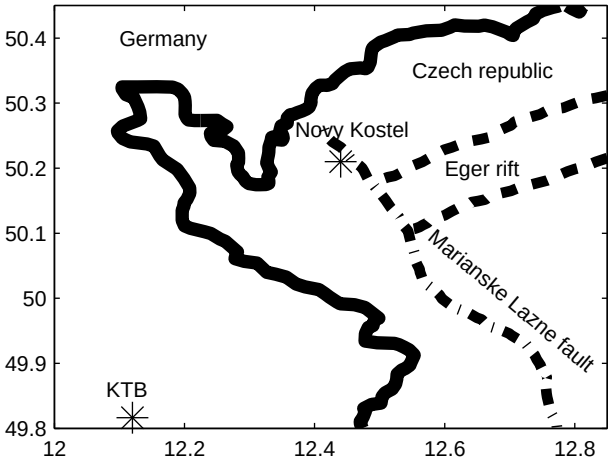

Figure 4.1: Map of the border region of Germany and Czech republic. Most recent earthquake swarms take place around the city Novy Kostel,which is located close to the Marianske Lazne fault and the Eger- rift system. The German continental deep drilling project (KTB) is nearby.

4.1 Introduction

The West Bohemia / Vogtland earthquake swarms coincide with degassing of CO_2 originating from the mantle. Young Quaternary volcanism with a magmatic body associated with a local up-doming of the Moho is the assumed source for the CO_2, which then propagates through a preexisting and re-stimulated fracture network Weinlich et al. [1999]. The fluids are suggested as the primary trigger for earthquake activity in the region (e.g. Spicak and Horalek [2001], Weise et al. [2001], Bräuer et al. [2003]). Most earthquake swarms over the last decades occurred in the Novy Kostel area (Czech Republic, see figure 4.1) within a region of several square kilometers. The maximum earthquake magnitude arising from these swarms is around $M_L = 3.5$, and include several thousands of microseismic events at depths ranging between 6.5 and 11km. Occasionally some deeper events are detected at around 13km depth, and occur along a steeply dipping fault plane (Fischer and Horalek [2003]). Earthquake swarms were recorded in 1985/1986, 1997, 2000, 2008 and 2011, during which pre- fractured areas were reactivated (Fischer et al. [2014]).
Estimating the maximum magnitude of seismic events is of great interest in all aspects of seismic hazard assessment, but has so far been limited to statistical estimates that have a very poor record (Geller [2011]). The maximum expected magnitude is of particular interest in cases of stimulation, such as enhanced geothermal systems (EGS), because this can determine the outcome of public acceptance of the project. Numerical simulations are occasionally used to assess seismic hazard, but existing models are based on simplified rheology and oversimplified mechanics, leading to a wide range of uncertainty (e.g. Baisch et al. [2010], McClure and Horne [2010]).
In this work we apply a method based on the deviatoric strain rate, in a sophisticated

hydro-mechanical model, to estimate seismic activity (Heinze et al. [2015a]), and use the 2008 swarm as a suitable test case.
An earthquake swarm is defined as a sequence without a single, dominant event (Yamashita [1998]). Field observations and numerical simulations suggest that fluid flow is an important component in the generation of earthquake swarms (Hainzl [2004]). Several numerical models have been applied to the West- Bohemian earthquake swarms, including a poro- elasto plastic finite element model to calculate stresses and strains (Kurz et al. [2003]). These studies demonstrated that the regional stress field is insufficient to cause earthquake swarms, but when combined with fluid migration they show reasonable rates of deformation capable to cause earthquake swarms. Statistical approaches can reproduce the seismic pattern of the 2000 earthquake swarm (Hainzl [2004]), where a brittle patch surrounded by an elastic half- space is loaded by fluid migration and stress changes. The spatio- temporal distribution of the seismic events is dominated by stress triggering, with fluid migration acting as the initiator. Linear diffusion models (Parotidis et al. [2005]) focused on a single fluid source to determine overall diffusivity.
Identifying the location and magnitude of numerical seismic events is not straightforward because there is no specific physical value which describes them. Some studies were performed for geothermal systems using a block- spring model approach to estimate seismic events and their magnitude (Baisch et al. [2010], McClure and Horne [2010]). In these models seismic events are calculated using an over-simplified physical model.
In this work we develop and apply a model to simulate the flow of super-critical CO_2 through a fracture network assuming non- linear diffusion with a stress and fluid pressure dependent permeability (Miller et al. [2004]). We solve the diffusion-advection equations for the temperature of the rock and CO_2, considering thermal non-local equilibrium. Stresses are calculated using a full poro-elasto-plastic rheological model that includes hardening, softening and damage. We detect seismic events and estimate their magnitude using the deviatoric strain rate as an indicator for rupture processes. Our theoretical model is implemented in a numerical scheme to simulate the dynamic behavior during an earthquake swarm.
After a short review of the 2008 swarm, we describe our rheological model and the governing equations of the fluid flow followed by their numerical implementation. We then present our numerical results and comparisons with field observations.

4.2 The 2008 Earthquake Swarm

The swarm 2008 stimulated the southern- sub cluster of the fault plane at Novy Kostel, which is separated by a seismic gap from the northern cluster where the 2011 swarm occurred. However, both clusters were shown to be connected in 1985/1986 sequence when the largest swarm on the fault occurred and activated both clusters (Fischer et al. [2014]).
The southern sub- cluster consists of a fault plane steeply dipping around 80 degrees towards the west. Hainzl et al. [2012] studied the 2000 and 2008 swarms in detail

and found that the 2008 swarm can be viewed as an extension of the 2000 swarm. Epicenter locations on the fault plane show that the 2008 swarm not only expended the seismic region but also occurred in places that were already fractured by the 2000 swarm.

Both swarms initiated from a similar spot, which was assumed to be the source of the fluid (Parotidis et al. [2005], Hainzl et al. [2012]). The fluid source is estimated as the mid point of the first 10 observed earthquakes. From this point a diffusion process can be used to estimate the fluid pressure and the fluid front. The results show faster diffusion towards the surface than downwards, further suggesting a diffusion-type process. In addition, downward migration stops after about nine days for the 2008 swarm, while the upward migration continues for several more days, leading to the suggestion (Hainzl et al. [2012]) that fluid injection stops after 9 days.

Relocated earthquakes using an improved velocity model (Ruzek and Horalek [2013]) shows that the main activity occurs along a square patch measuring about 4km on a side.

As is typical for swarm seismicity, the frequency-size statistics shows b-values around 1 for the Gutenberg- Richter law (Fischer et al. [2010]).

$$N = 10^{a-bM} \tag{4.1}$$

where N is the number of earthquakes with a magnitude larger or equal to M, a and b are empirical constants.

The magnitude M can be calculated from its seismic moment M_0 following an empirical relation for the Vogtland region (Hainzl [2004])

$$M = 0.95 \cdot log(M_0) - 10.76 \tag{4.2}$$

Other characteristic values are an inter- event time scaling with $i^{-3.5}$ and cumulative energy release with $i^{1.25}$, where i is the index in the earthquake catalog. The 2008 swarm lasted from the beginning of October until the end of December, 2008, releasing a seismic moment of around $4.1 \cdot 10^{16}$ Nm (Fischer et al. [2010]). The swarm shows periods of inactivity for several days, with the first swarm being the most active and lasting 30 days.

4.3 Mathematical Model

4.3.1 Poro-elasto-plastic Rheology

The elastodynamic equations in 2D in their velocity-stress formulation describe the elastic response of a rock skeleton

$$\frac{\partial V_x}{\partial t} = \frac{1}{\rho}(\frac{\partial \sigma_{xx}}{\partial x} + \frac{\partial \sigma_{xy}}{\partial y}) \tag{4.3}$$

$$\frac{\partial V_y}{\partial t} = \frac{1}{\rho}(\frac{\partial \sigma_{yy}}{\partial y} + \frac{\partial \sigma_{xy}}{\partial x}) - \rho \cdot g \tag{4.4}$$

$$\frac{\partial \sigma_{xx}}{\partial t} = (\lambda + 2\mu)\frac{\partial V_x}{\partial x} + \lambda \frac{\partial V_y}{\partial y} \tag{4.5}$$

$$\frac{\partial \sigma_{yy}}{\partial t} = \lambda \frac{\partial V_x}{\partial x} + (\lambda + 2\mu)\frac{\partial V_y}{\partial y} \tag{4.6}$$

$$\frac{\partial \tau_{xy}}{\partial t} = \mu \left(\frac{\partial V_x}{\partial x} + \frac{\partial V_y}{\partial y} \right) \tag{4.7}$$

where μ is the shear modulus, λ is Lamé constant, ρ is density, V_x and V_y are velocities, σ_{xx}, σ_{yy}, τ_{xy} are the stress tensor, and g gravitational acceleration.
In saturated porous rock, where pores form a connected network, deformation is controlled by the Terzaghi effective stress

$$\sigma_{ij}^{eff} = \sigma_{ij} - P\delta_{ij}. \tag{4.8}$$

We use thermal elasticity for a change of rock temperature $\theta = T - T_0$. Thermal stresses only act in the normal directions with no shear component. Using the vector $I = (1, 1, 0)$ the stresses can be calculated together with the elastic stresses due to load:

$$\sigma = E\epsilon_e + \beta EI\theta \tag{4.9}$$

where E is the elasticity tensor and β the coefficient of thermal expansion.
Plastic deformation of rocks is modeled using the Mohr-Coulomb criteria

$$F = \tau - \left(\sigma_m - \frac{C^*}{tan(\varphi^0)} \right) \cdot sin(\varphi^*) \tag{4.10}$$

where F is the yield function, C^* is mobilised cohesion, φ^* is mobilized internal frictional angle,φ^0 is the maximum internal frictional angle, τ is stress deviator, and σ_m is mean stress (Vermeer and de Borst [1984]).
Cohesion and internal friction angle are mobilized in terms of a cohesion weakening and frictional strengthening model and is dependent on effective plastic strain $\bar{\epsilon}_p$ (Hajiabdolmajid et al. [2002]). Mobilized values for the friction angle, cohesion and dilatancy angle are calculated following (Vermeer and de Borst [1984]).
Plastic strain rates are given by

$$\dot{\epsilon}_{ij}^p = 0 \text{ for } F < 0 \text{ or } F = 0 \text{ and } \dot{F} < 0 \tag{4.11}$$

$$\dot{\epsilon}_{ij}^p = \lambda^p \frac{\partial q}{\partial \sigma_{ij}} \text{ for } F = 0 \text{ and } \dot{F} = 0. \tag{4.12}$$

with λ^p acting as the plastic multiplier and q is the flow rule.

Effective plastic strain $\bar{\epsilon}_p$ then follows

$$\bar{\epsilon}_p = \sqrt{\frac{2}{3}\dot{\epsilon_p}^T \cdot M \cdot \dot{\epsilon_p}} \tag{4.13}$$

where M is a weighting matrix (Abbo [1997]).
We use non-associative plastic flow rules (Vermeer and de Borst [1984])

$$q = \tau - \sigma_m \cdot sin(\psi^*) \tag{4.14}$$

where ψ^* is the mobilized dilatancy angle (Vermeer and de Borst [1984]).
Degradation of elastic properties dependent on damage is describe by the operator D

$$E^d = (1 - D)E^0 \tag{4.15}$$

where E is the elasticity tensor in damaged E^d and undamaged E^0 state. Evolution of D is modeled following the method described in (Peerlings et al. [1998]).

4.3.2 Fluid Flow and Heat Transfer

We model fluid pressure diffusion without sources and sinks

$$\frac{\partial P}{\partial t} = \frac{1}{\phi(\beta_f + \beta_\phi)} \nabla \left(\frac{k}{\eta} \nabla P \right) \tag{4.16}$$

with pore pressure P (above hydrostatic), compressibility for fluid and rock matrix β_f and β_ϕ, permeability k and fluid viscosity η. We assume permeability to be stress and pressure dependent (Miller et al. [2004]):

$$k = k_0 \cdot exp^{\left(-\frac{\sigma_n - P}{\sigma_0}\right)} \tag{4.17}$$

where σ_n is the normal stress and σ_0 a scaling coefficient.
We determine heat transfer Q between rock and fluid as:

$$Q = hA(T_f - T_r) \tag{4.18}$$

where T is temperature of the fluid f and rock r (Shaik et al. [2011]). Heat transport in the solid is described by a diffusion equation.

$$\frac{\partial T_r}{\partial t} = \frac{\kappa_r}{(1 - \phi)\rho_r c_{pr}} \nabla^2 T_r + \frac{1}{(1 - \phi)\rho_r c_{pr}} Q \tag{4.19}$$

where κ_r is thermal conductivity, ρ is density and c_{pr} heat capacity (Bejan [2013]). The heat of the fluid also considers an advection term with Darcy velocity v.

$$\frac{\partial T_f}{\partial t} = \frac{\kappa_f}{\phi\rho_f c_{pf}} \nabla^2 T_f - \frac{1}{\phi\rho_f c_{pf}} Q - \nabla(vT_f) \tag{4.20}$$

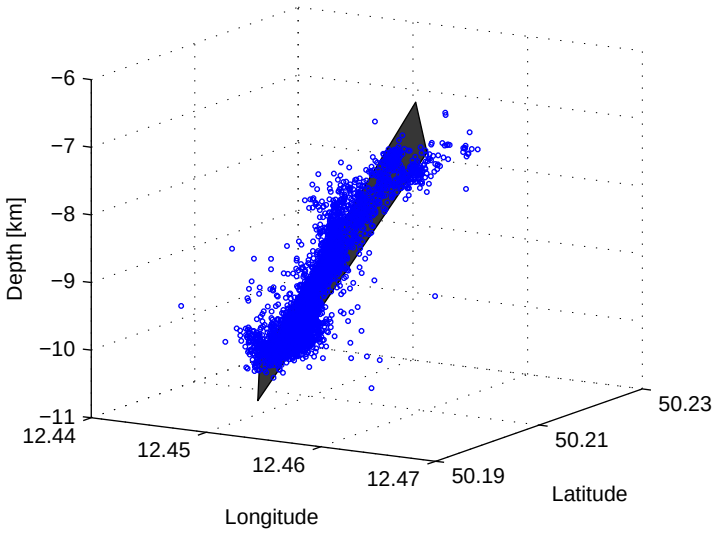

Figure 4.2: Three- dimensional presentation of the observed seismic events and the two dimensional modeled domain with an area of $4 \cdot 4$ km.

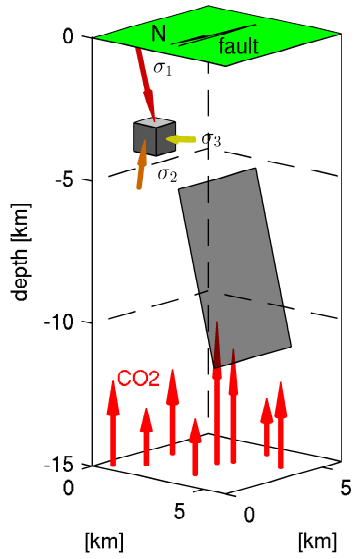

Figure 4.3: Three- dimensional sketch of the modeled domain with orientation of the principal stresses and CO_2 rising from the upper mantle.

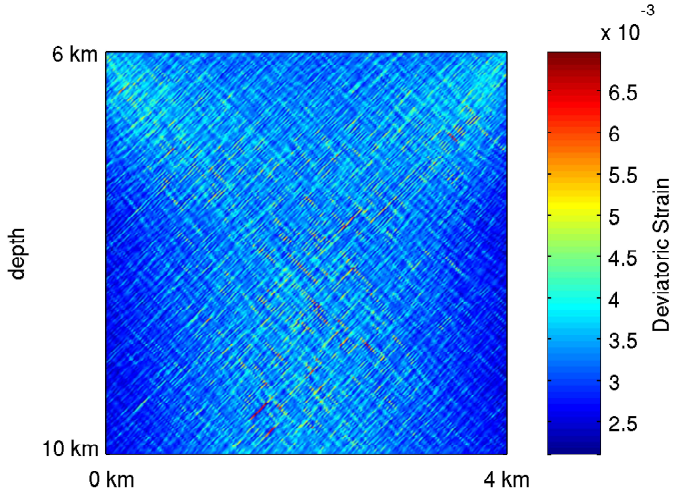

Figure 4.4: Deviatoric strain after the applied pre- fracturing to generate a fracture network in agreement with the local stress field. High deviatoric strain indicates shear movement and local failure.

4.4 Numerical Model and Event Detection

In our numerical model we simulate the intrusion of over-pressurized, hot, super-critical CO_2 as a point of increased pressure in the fault plane indicated by the seismic data (Fischer et al. [2014], Heinicke et al. [2009]). The modeled domain extends from 6 and 10 km depth and has an overall area of $4 \cdot 4$ km (figure 4.2). For a comparison with the observed seismic data, we project the earthquake locations on the two- dimensional plane. The overall structure of the simulation setup is shown in figure 4.3.

We adopt the stress field from Vavrycuk [2002] and Vavrycuk [2011], which is in agreement with values from Brudy and Zoback [1999] obtained at the nearby KTB drill site. Rock properties are taken from Shapiro et al. [1997] and Schön [2011]. Measurements performed at the KTB site shows a temperature gradient of around around 28°C/km. Further thermal parameters are presented in Heinicke et al. [2009] and Safanda and Cermak [2000]. All simulation parameters values are given in table 4.1. We also condition the model by pre- fracturing the system by applying external forces (increasing the maximum principal stress) until fractures were generated in the model in response to these applied stresses. This load was then relaxed so that the observed stress field is recovered before the fluid injection starts (cf. figure 4.4). Following the isotope analysis and considering the fluid pressure and temperature conditions, we assume a saturated environment of super-critical CO_2 in the modeled domain (Bräuer et al. [2003], Kurz et al. [2003]). Static fluid pressure is calculated respectively. The chosen values are given in table 4.2.

We numerically implement the mathematical model in a two dimensional finite-differences scheme using a staggered grid (Galvan and Miller [2013]). The numerical resolution is 20m between grid points in each direction.

E	ν	φ	C_0	ϕ	k	κ_r	c_{pr}
60GPa	0.25	30°	20MPa	0.02	$3 \cdot 10^{-16}\mathrm{m}^2$	$3^{\mathrm{W}}/_{\mathrm{m^2K}}$	$790^{\mathrm{J}}/_{\mathrm{kgK}}$

Table 4.1: Rock properties used in our numerical simulation. Values chosen based on Shapiro et al. [1997],Schön [2011],Brudy et al. [1997],Clauser et al. [1997].

ρ_f	β	κ_f	η	c_{pf}
900kg	$5 \cdot 10^{-9}{}^{1}/_{\mathrm{Pa}}$	$0.04^{\mathrm{W}}/_{\mathrm{m\ K}}$	10^{-4}Pa s	$1440^{\mathrm{J}}/_{\mathrm{kg\ K}}$

Table 4.2: Fluid properties used in our numerical simulation. Values chosen based on Span and Wagner [1996] and Fenghour et al. [1998] for the in situ pressure and temperature conditions.

We determine the magnitude of numerical seismic events using deviatoric strain rate as a proxy. Deviatoric strain rate identifies rapid changes in strain, and thus separates these rapid changes from continuous slow deformation. Figure 4.5 shows and example of deviatoric strain, deviatoric strain rate and the yield function of one grid point over time. The deviatoric strain rate shows a clear peak, followed by a longer phase of above average rate activity. Simultaneously, deviatoric strain increases significantly and the yield function of the grid point falls considerably below zero shortly after the event, indicating stress relaxation after a long period of plastic deformation. This reduction corresponds to the stress drop associated with shear slip accompanying failure.
We identify the peak, as well as start and end point, of the event by examining the deviatoric strain rate. If it exceeds a given limit the time is stored as the starting point and deformation is continually calculated until the deviatoric strain rate drops below the limit that we identify as the end the individual event. We call the time span between start and stop point the excitation time (see figure 4.6). If slip events occur on neighboring cells with overlapping excitation times, the events are combined to one event and the seismic moments are summed, where the seismic moment is

$$M_0 = G \cdot A \cdot u \tag{4.21}$$

where G is the shear modulus, A the area of the shear plane and u the displacement. The area of one grid cell is calculated with incremental distance dx and dy between nodes in the $x-$ and $y-$ direction, and moment magnitude is calculated using equation 4.2.

4.5 Results

For clarity in the comparisons between model and observations, we only consider events with M > 0.5.
Earthquakes triggered by high-pressure fluid from a point source show a characteristic seismic cloud which grows following the fluid front (Shapiro et al. [2003]). We study the radial distance of earthquakes from the injection point over time (figure 4.7). The overall behavior of the numerically simulated event cloud follows the

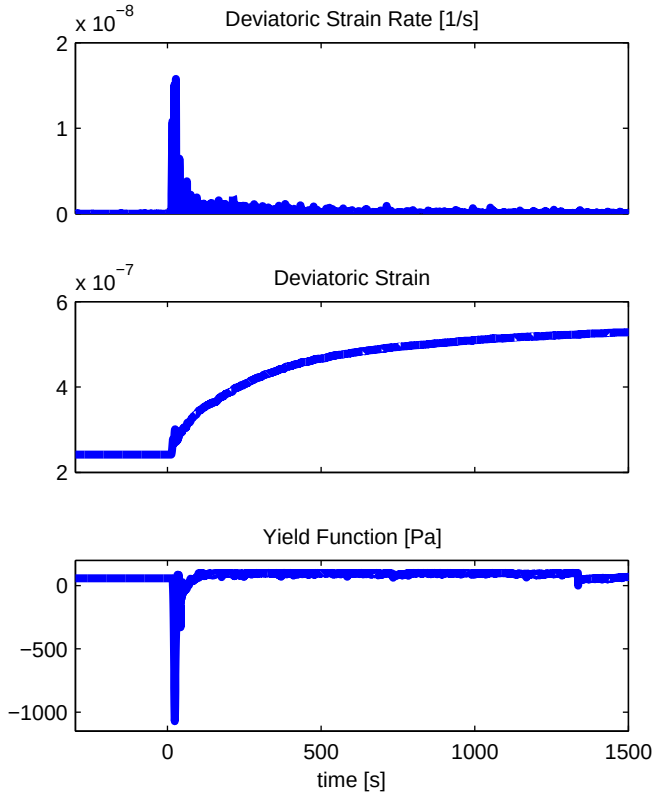

Figure 4.5: Deviatoric strain rate, deviatoric strain and yield function over time of one grid point during a rapid shear movement.

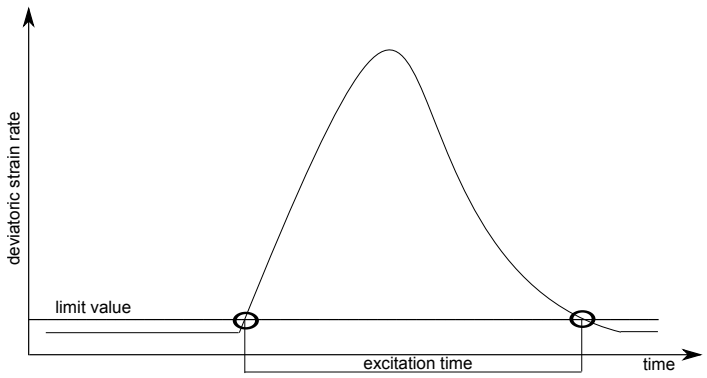

Figure 4.6: Defining the excitation time window for one cell. If deviatoric strain rate exceeds a defined limit,the excitation time starts. As soon as it drops below the limit the event stops. The time during start- and end point gives the excitation time window during which all displacement is summed up for this slip event.

earthquake catalog cloud very closely. In both cases, the downwards movement of the seismic cloud is lower than upwards due to gravity effects on the permeability and the hydrostatic pressure gradient. For both cases, when injection stops, after a week, events are mainly registered along the fluid pressure front and only very few events occur close to the injection point.

The correlation between fluid pressure and earthquake occurrence is also observed by viewing upon the fault plane and modeled domain. Figure 4.8 shows the earthquakes occurring at day 7 and 8 of the 2008 swarm and the calculated pressure distribution at the same times. The diffusing over-pressure propagating from the injection point supposes the static pressure gradient, with most of the earthquakes lying inside, or close to, the pressure front. The chosen injection pressure of around 100 MPa corresponds to an over-pressure of 10 MPa at the injection point.

Figure 4.9 shows the fluid and rock temperature profiles. The temperature change in both the fluid and rock it is very small, which means that thermally-induced stresses are negligible compared to tectonic stresses and fluid pressure. The temperature of the CO_2 is dominated by its advection term, overlapping the geothermal gradient. The rock temperature increases around 20°C assuming an initial temperature of the injected fluid of 500°C (figure 4.9).

Figure 4.10 compares the magnitudes of observed and modeled earthquakes for the first 30 days of the 2008 swarm. Mostly small magnitude events are observed in the early stages, and this is similar to injection of fluid in a geothermal system as a larger area needs to be stimulated to generate higher magnitude earthquakes (Baisch et al. [2010]). During the first 30 days, several events with maximum magnitudes of around M3.5 are observed. At around 20 days, maximum magnitudes decrease because the fluid injection stops after a week. Figure 4.10 shows that magnitudes of numerical earthquakes do not differ significantly from those observed in the earthquake catalog.

The cumulative released seismic moment shows a similar behavior (figure 4.11), with both the simulation and observations roughly following a power law with exponent $i^{1.25}$. The total released seismic moment is around $4 \cdot 10^{16}$ Nm. Figure 4.11 shows the inter-event time. In the simulation, slightly more events are detected than in the seismic catalog, and the inter-event time of the simulation tends to be shorter than the recorded 2008 swarm inter-event time. However, both model and observations produce the same power-law and have similar deviations from the power law for large inter-event times. The absolute difference in inter- event time between seismic catalog and the numerical results is approximately one hour.

The b-value of the Gutenberg-Richter (GR) relationship of 2008 earthquake swarm is around 1 (figure 4.12), which is also be reproduced by the simulation. Small derivations between the earthquake catalog and model results simulation is caused by the larger number of events detected in the simulation. Figure 4.12 also highlights that the maximum magnitude of the simulation is similar to that observed.

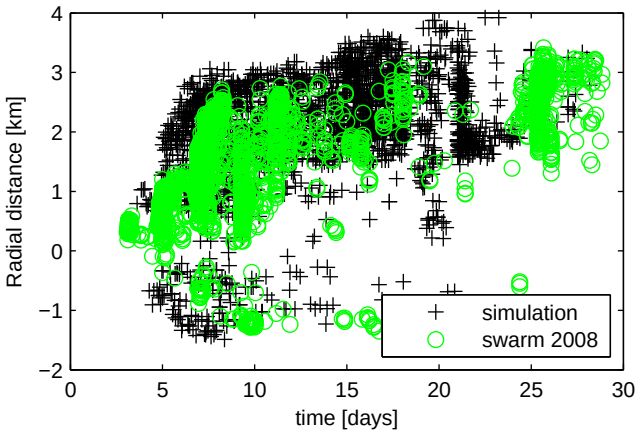

Figure 4.7: Radial distance of earthquakes during the first 30 days of the 2008 swarm and events detected during the simulation from the injection point. Seismic cloud propagates away from the point source over time. Diffusion is faster upwards than downwards. Injection stops after 7 days. Events become less afterwards and mainly occur near the pressure front further away from the source.

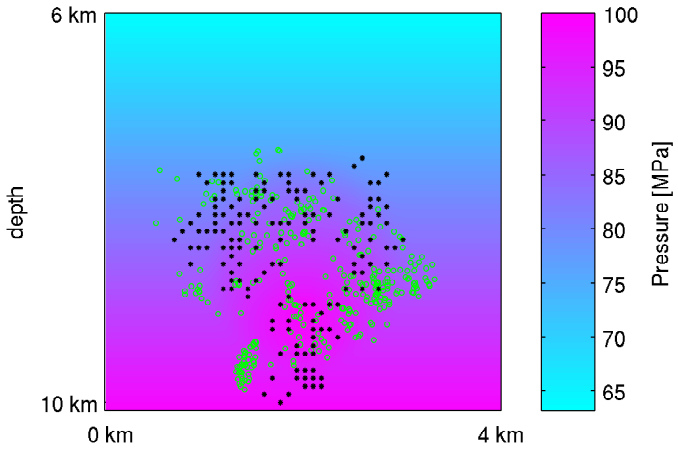

Figure 4.8: Frontal view on the fault plane and modeled domain. Pressure values calculated for day 8 after intrusion started. Background static pressure gradient is overlapped by overpressured fluid source with 10 MPa overpressure. Earthquakes occurring during day 7 and 8 of the 2008 swarm are marked in green circles. Simulated analogs are marked in black. Most of the events lie in or close by the region with increased pressure around the intrusion point.

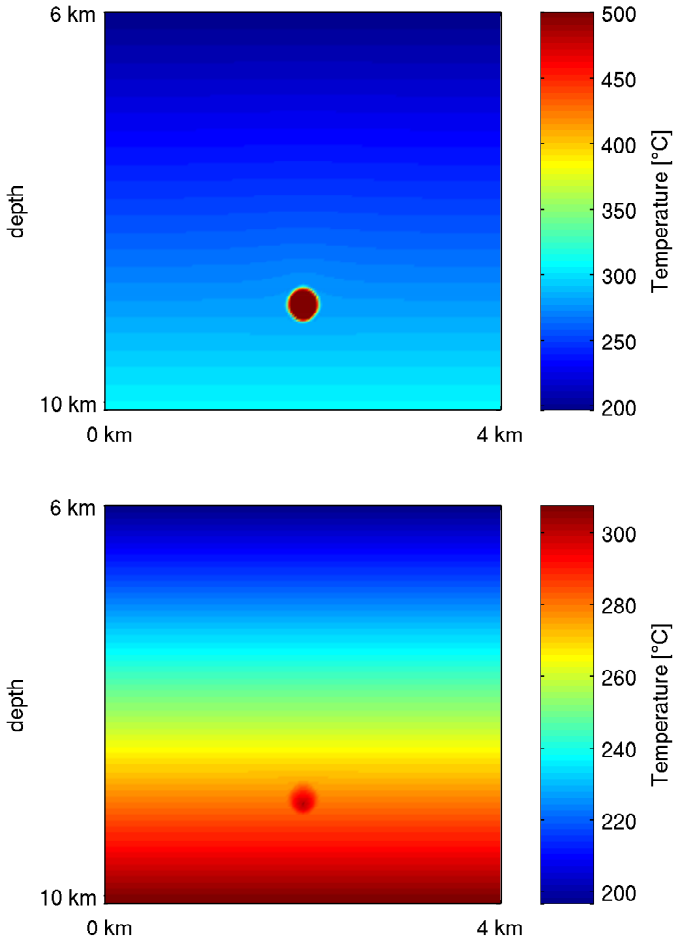

Figure 4.9: Frontal view on the fault plane and modeled domain with Temperature of fluid (top) and rock (bottom) after a week after the injection started. Heat transfer in the fluid is dominated by advection terms. Increase in rock temperature is about 20°C by an assumed fluid temperature of 500°C. Rock temperature changes only visible around intrusion point.

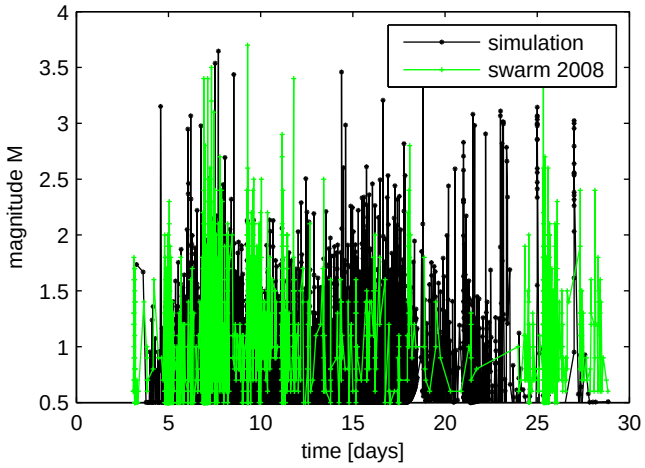

Figure 4.10: Magnitude of earthquakes and events during simulation over time for the first 30 days of the 2008 swarm. First only events with small magnitude are observed in simulation and in the seismic measurements. Maximum magnitudes range around 3.5. Magnitudes decline during later days following Gutenberg- Richter law.

4.6 Discussion and Conclusion

Our model results reinforce the hypothesis that high pressure fluids are the dominant mechanism triggering and driving the Bohemian swarms. Fluid over-pressure in the range of 10 to 20 MPa reproduces well the observations, and this range is in agreement (but at the lower end) of that suggested by Hainzl et al. [2012], and far below the values estimated by Vavrycuk [2002] and Kurz et al. [2003]. Lower over-pressure is required for triggering in the model because the non-linear diffusion formulation allows for much faster fluid pressure propagation behind the rupture front, and therefore more fluid pressure is available to trigger earthquakes.
As found in other studies, temperature has only a minor influence on the behaviour of this system (e.g. Safanda and Cermak [2000], Kurz et al. [2003]). The amount of fluid intruded is insufficient for heat transport to play a dominant role. When the fluid intrusion ceases (around a week after the swarm started), the downward propagation of the seismic cloud also stops and events near the intrusion point begin to fade at around 9 days into the swarm. This in agreement with another study that suggested about a 9 day intrusion process (Hainzl et al. [2012]). Although the intrusion stopped at the source, the system continues to evolve because pressure gradients still persist in the system, and will continue to diffuse and therefore trigger additional events (Miller [2014]).
Our modelling results show very good agreement with observations of the 2008 swarm in the Eger Rift, including the propagation of the seismic cloud away from the injection point, the magnitudes of simulated and observed events, and their temporal evolution. Using deviatoric strain rate as a proxy for the magnitudes associated with numerical earthquakes, we produce GR statistics and inter-event times in good agreement to those observed (albeit with slightly more numerical earthquakes detected). Our model can be improved to model other aspects that we

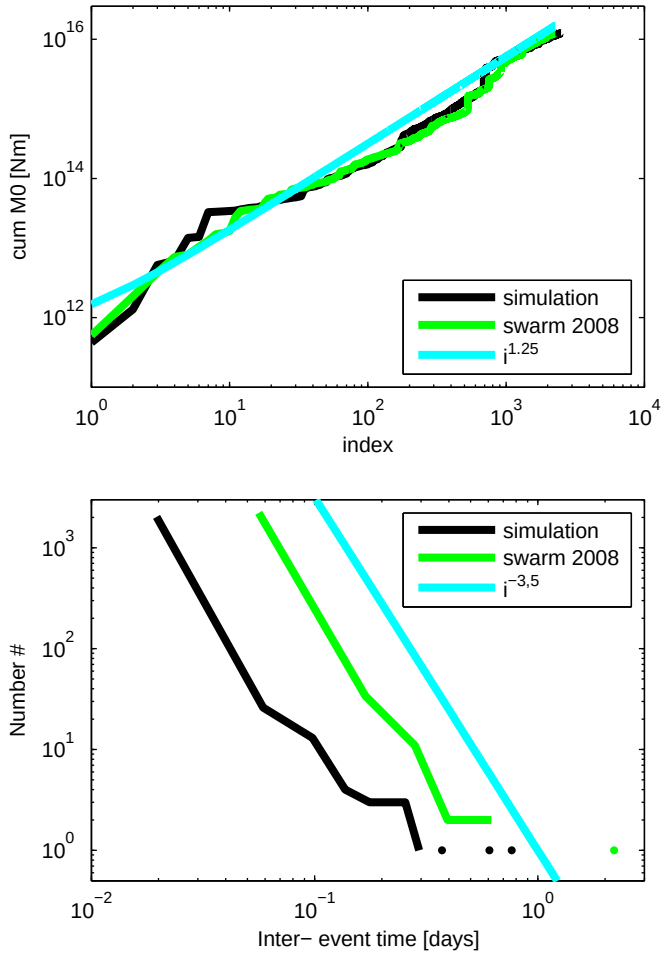

Figure 4.11: Cumulative released seismic moment (top) and time between consecutive events (bottom). Observed earthquakes and detected events of the simulation follow roughly the same power laws and have similar differences from the power laws. Slightly more events are detected during the simulation and earthquakes registered in the catalog. The released seismic moment is slightly higher and the inter-event time shorter in the simulation than with the official earthquake catalog.

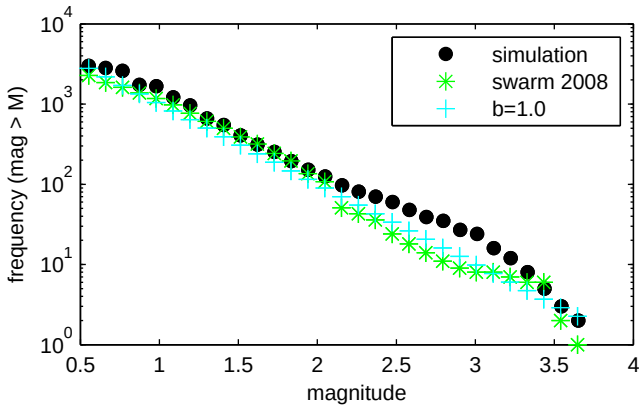

Figure 4.12: Gutenberg- Richter law for the earthquake catalog and the events detected during simulation. Both have a b- value around 1 and equal maximum magnitude. As more events are registered in the simulation, the results are different from catalog and simulation but follow the same b-value.

currently ignore. The most important development would be to allow fractures to nucleate, grow, and coalesce in response the prevailing regional stress field and to perturbations in the stress field associated with the evolving fracture network. This is important because damage that likely developed from previous swarms should be included, as well as the new crack network developed during a new swarm. A more accurate model might also include other major fault planes likely to be imaged in future studies. While our rheological model includes hardening/ softening and damage effects, future developments might also include heterogeneity, anisotropy, or chemical reactions (Heinicke et al. [2009]) that can alter rock properties or seal up flow pathways. Temperature or pressure dependent properties of the fluids might also affect the behaviour, although we suspect that these have a second-order influence. Of particular note, our method for detecting numerical events may provide an important tool for mechanistic seismic hazard assessment. In our study of the 2008 earthquake swarm, we used the deviatoric strain rate analog (and comparison to observations) to estimate the fluid pressure source in a reverse way. However, we envisage an extension of the model to assess seismic risk in a prospective way in cases of a known injection source, such as in Enhanced Geothermal Systesm (EGS) (Miller [2014], Häring et al. [2008]).

Acknowledgment

We thank the German Research Foundation, Deutsche Forschungsgemeinschaft (DFG), for the financial support through the project no. MI 1237/7-1 and the VW foundation through the grant 'Extreme Events'. We thank Dr. T. Fischer for providing us with the earthquake catalog and helpful comments on the manuscript.

Chapter 5

Conclusion and future research perspective

Aim of this thesis is to expand the physical knowledge about fluid- rock interactions in the upper 20 km of the crust and to develop numerical tools for the analysis of natural phenomena. The scientific papers presented in this thesis deal with various physical and numerical aspects where pre-existing models fall short and improvements are necessary.

The first scientific paper in this work deals with the development of a hyper- plastic model which couples plastic flow and damage evolution. We dismiss the hypothesis of effective damage models, which assume that deformation is not influenced by the degradation of elastic properties, and derive a set of fully coupled differential equations. In opposite to similar pre- existing coupled models we use an explicit solution scheme to solve the coupled equations and consider several numerical issues during the computation. We achieve a good match with experimental results of a cycling experiment of concrete and reproduce some characteristics in the dynamic behavior, like the hysteresis during the unloading phase, which other models are not able to reproduce. Hence, the developed model slightly underestimates the necessary stress to progress in damage evolution. Modifications in the theoretical model, for example applying a yield function more suitable for concrete or a different plastic potential, could help to overcome these shortcomings. The developed algorithm and the demonstrated importance of applying a mapping- back algorithm for both, damage and yield- function, are not affected by those modifications. The algorithm can also be transferred to any other two- surface damage model as surface drift is a principal numerical problem evident in any one- bounded problem. We show that realistic results are only achievable considering damage surface drift. otherwise damage may be overestimated. On the other hand, the developed theoretical and numerical model is rather complex and increases computational costs. It remains further to examine how the improved damage model influences results on larger scale and if noticeable improvements can be achieved, which justifies the computational costs.

Degradation of elastic properties becomes evident when rock is close to failure or subjected to various loading and unloading cycles (Kachanov [1958], Taqieddin [2008],

Voyiadjis and Taqieddin [2009], Omidi and Lotfi [2010]). Both is the case in many scenarios with fluid- rock interactions. In hydro- fracturing the fluid pressure is increased till fractures are generated and local failure occurs. These new fractures increase local permeability and cause a short pressure drop. The rock is subjected to cycling pore pressure. Also, often fluid pressure increases and decreases again over time at larger scale, like for example during stimulation processes of reservoirs which are performed over several stages. Earthquake swarms are another example for cycling fluid pressure because swarms occur at similar geological spots distributed over years or even decades. A capable and realistic damage model is therefore essential for any reasonable approach of simulating complex fluid- rock interactions.

Laboratory experiments are essential to validate and benchmark the theoretical and numerical models. Various parameters can be measured and used to compare theoretical and numerical approaches with reality. Stress- strain response curves, volumetric strain, plastic strain, wave velocities etc. are useful numbers and can be observed dynamically during the experiment, like we used it for the damage model (e.g. Stanchits et al. [2011], Mayr et al. [2011], Sinha et al. [1964], Chiarelli et al. [2003]). All these values are bulk measurements and can only be measured for the whole probe. Experimental techniques are not able to resolve local heterogenities.

Other values like permeability and porosity can not even be observed dynamically (Blöcher et al. [2009]). They can only be obtained before and after the experiment itself. To match a complex theoretical and numerical model to the experiment and benchmark it, this is sometimes not enough. A common value to measure on laboratory scale are acoustic emissions (AE). AEs are generated whenever grains break or shear (Lockner [1993]). Therefore, AEs can give information about the very local scale during the experiment and be a helpful tool for the analysis with a theoretical model. There is no decent physical value dedicated to AEs which is a drawback for a theoretical model.

Several models exist to find an analytical substitution for AE. Physical values like yield function and damage operator or newly introduced can be used. We start with defining critical characteristics of AE which need to be fulfilled by a proxy. Based on this analysis I propose the deviatoric strain rate as a proxy, which fits the found criteria and the presented comparisons between laboratory experiments and numerical simulation show reliability of this method. As deviatoric strain rate is a value for shear movement a physical link to AEs is given as the used Mohr- Coulomb failure condition signals shear failure. The found method is physically reasonable and can be derived from the governing equations of solid mechanics without the need of introducing new parameters.

The successful test on laboratory scale for drained and undrained rock enables an expansion of this approach to field scale. This is done with the example of the 2008 earthquake swarm in West Bohemia. I am able to reproduce the original earthquake catalog very well in terms of magnitudes, spatial- temporal evolution of the earthquakes, released seismic energy and other features. The simulation of the Bohemian swarm is done with a fully coupled thermo- hydro- mechanical (THM) model as heat transport and thermal stresses are included besides the already discussed hydro- mechanical parts. Together with the developed picker algorithm

for a numerical analog for earthquakes a new simulator is presented. We also see that developing and benchmarking new methods on laboratory scale with a better foundation of collected data and then transferring it to field scale works well.
Looking at the simulation of the bohemian earthquake swarm in more detail several yet to solve issues remain. Using the developed tool in a kind of prognostic way, for example for industrial applications in geothermal energy, requires a rather complete data set in terms of fluid properties, geology, rock types, heterogenity etc. In the terms of the bohemian earthquake swarm the simulation was used to estimate fluid pressure, permeability and other important, but unknown, properties. The simulation result is therefore a simplified reconstruction of the natural phenomena and can be seen as a proof of concept. For a more realistic approach heterogenity and anisotropy need to be considered. The bohemian earthquake swarm also has a clear two- dimensional geometry due to fluid propagation a long a fault plane. For more complex geometries a three- dimensional approach will need to be applied. While all developed concepts in this work can easily be transported to a three- dimensional model, the spatial clustering to determine the slip- area of an earthquake becomes more complex and needs additional work. Expanding the model to three- dimensions causes also numerical considerations. As long as deformation remains small a finite difference scheme should be efficient and adequate. If necessary markers in cell or adaptive meshes could be introduced (Gerya et al. [2013], Duretz et al. [2011]). Finite element and meshless methods on the other hand can be numerically cumbersome and more complex. These methods are only reasonable to use with an implicit solver which enables larger larger time steps. When applying the developed picker algorithm to detect an analog for an earthquake the time step is physically limited to a fraction of a duration of an earthquake. Computational costs will therefore increase significantly in any three dimensional model. Transporting the developed model to newer technologies like graphical processor units (GPUs) remains challenging (Galvan and Miller [2013]).
On a mechanical perspective the developed model is multifunctional and advanced compared with other models available. Weak points are concentrated in the fluid and heat transport section which is out of scope of this work. Considering gravity flow with salinity, phase change and mass transport would improve the model significantly. With these tools for example the permeability on field scale could be determined more accurate by reproducing standard tracer tests. Also only considered in a rather basic way are thermal influences. Thermal elasticity could be expanded by using dynamic parameters for heat transfer and thermal expansion (Tian [2013]). Thermal plasticity can also be an important part in fluid- rock interactions when the temperature difference between rock and fluid is high. This can for example be the case in geothermal systems or underground storage of carbon dioxide. Also chemical alterations of the minerals due to fluid can change the mechanical response of the rock. Any of these features would improve existing models even further.

Appendix

Chapter 6

Modeling porous rock fracturing induced by fluid injection - Numerical simulation and comparison with laboratory experiments

Abstract

Hydraulic fracturing and hydro-shearing are important processes in engineering applications such as Enhanced Geothermal Systems (EGS) and hydraulic fracturing of tight shales. In this paper, we describe and implement a theoretical model that captures the physical processes occurring during hydraulic fracturing of saturated and unsaturated, porous rock. The model is based on a poro- elastic- plastic rheology with a Mohr-Coulomb yield function and unassociated flow rule, and includes frictional hardening, cohesion weakening, damage and mobilized dilatancy effects. In addition, fluid injection is described as a two-phase flow using the Richard's approximation. We numerically implement the model using a finite difference scheme on a staggered grid, and compare the model results with laboratory experiments. We use three different laboratory configurations for comparing model results and observations: a) triaxial compression of a drained rock sample, b) low pressure fluid injection into a drained, critically stressed rock, and c) high pressure fluid injection into a saturated rock sample. We find excellent agreement between model and observations for all cases, indicating a proper formulation and implementation of the dominant physical mechanisms acting. The model reproduces experimental observations of macroscopic fracture, fluid front localization, and the stress-strain response curves. Matching observations from laboratory scale experiments establishes a benchmark and a calibrated model for numerically simulating experiments performed at the larger, field scale.

6.1 Introduction

Engineering applications for injecting high pressure fluids in geological formations have increased dramatically over the last years. Some examples include enhanced geothermal systems (EGS), energy production of shale gas/oil reservoirs, injection of waste water, and carbon capture and storage (CCS). Fluid injection, however, can increase seismicity and cause a general increase in seismic hazard (Häring et al. [2008], Baisch et al. [2010], dePater and Baisch [2011], Holland [2011]). Sophisticated numerical models are needed to understand the Thermal- Hydraulic- Mechanical-Chemical (THMC) response of the system to optimize the resource extraction (i.e. heat, hydrocarbon) or injection (i.e. CCS and waste water) while minimizing the hazards. There are several models that describe the mechanical response of the rock (Hajiabdolmajid et al. [2002], Poliakov et al. [1994]) and multiphase flow (Richards [1931],Dagger [1997],Cropper et al. [2011]) that can be used to describe hydrofracturing. However, to date there are no adequate quantitative or qualitative comparisons of model results with high resolution laboratory experiments (Baisch et al. [2010],Rutqvist et al. [2002]). Such comparisons are essential if one is to address the reliability of different rock mechanical models to be upscaled for real world applications, particularly in terms of seismic hazard associated with fluid injection.

High resolution laboratory experiments of hydraulic fracturing of critically stressed rock samples (Stanchits et al. [2011], Mayr et al. [2011]) recorded high precision acoustic emissions (AE) using ultrasonic tomography and were used to link AE to propagation of the fluid front. Such correlations between the fluid front and AE (comparable to micro-seismic events) had not previously been achieved. Although AE have a lower frequency than seismic waves, the underlying hydro-mechanical processes that generate them are similar Cai et al. [2007]. Significantly, laboratory and field data show similar behavior during hydraulic stimulation. The occurrence of acoustic or seismic events is dependent on the injection source, with similar behavior over time, and a clear link between propagation of the fluid front and triggering of acoustic and seismic events has been observed (cf. Rutqvist et al. [2002],Stanchits et al. [2011],Shapiro et al. [2003]). Therefore, the behavior at the field scale can be inferred from a detailed understanding of the processes at laboratory scale.

In this paper, we develop a porous rock-mechanical model based on a poro-elastic-plastic rheology with a Mohr-Coulomb yield function and unassociated flow rule. The model includes frictional hardening, cohesion weakening, damage and a mobilized dilatancy effect that achieves a realistic porous rock behavior. The mechanical model is then coupled to a two-phase flow using the Richard's approximation. The model is implemented using a finite difference scheme on a staggered grid (Saenger et al. [2000], Cruz- Atienza and Virieux [2004]) and compared to laboratory measurements.

The simulation framework FLAC also uses a finite difference scheme to calculate stresses and deformations (Itasca consulting group [2012]). As it is commercial software, optimizations and changes on the code are only capable using pre-defined interfaces. Other modeling frameworks like CSMP++ (Matthäi et al. [2007]) or OpenGeosys (Kolditz et al. [2012]) are platforms to simulate physical processes in

environments with a complex geometry based on finite element calculations, but can be numerically cumbersome for simulations with high spatial and temporal resolution. None of these tools have been used to successfully study laboratory rock experiments in detail.
We investigate three different laboratory configurations: a) triaxial compression of a drained rock sample; b) low pressure fluid injection into a drained, critically stressed rock; and c) high pressure fluid injection into a saturated rock sample.

6.2 Theoretical Model

6.2.1 Poro- elastic- plastic rheology

The elastodynamic equations in their velocity-stress formulation describe the elastic response of the rock skeleton for two dimensions

$$\frac{\partial V_x}{\partial t} = \frac{1}{\rho}(\frac{\partial \sigma_{xx}}{\partial x} + \frac{\partial \sigma_{xy}}{\partial y}) \tag{6.1}$$

$$\frac{\partial V_y}{\partial t} = \frac{1}{\rho}(\frac{\partial \sigma_{yy}}{\partial y} + \frac{\partial \sigma_{xy}}{\partial x}) \tag{6.2}$$

$$\frac{\partial \sigma_{xx}}{\partial t} = (\lambda + 2\mu)\frac{\partial V_x}{\partial x} + \lambda\frac{\partial V_y}{\partial y} \tag{6.3}$$

$$\frac{\partial \sigma_{yy}}{\partial t} = \lambda\frac{\partial V_x}{\partial x} + (\lambda + 2\mu)\frac{\partial V_y}{\partial y} \tag{6.4}$$

$$\frac{\partial \tau_{xy}}{\partial t} = \mu\left(\frac{\partial V_x}{\partial x} + \frac{\partial V_y}{\partial y}\right) \tag{6.5}$$

where μ and λ are the Lamé constants, ρ is the density, V_x and V_y is the velocity vector and σ_{xx}, σ_{yy}, τ_{xy} is the stress tensor.
In saturated porous rock, where pores form a connected network, deformation is controlled by the Terzaghi effective stress

$$\sigma_{ij}^{eff} = \sigma_{ij} - P\delta_{ij}. \tag{6.6}$$

Plastic deformation of rocks is modeled using Mohr-Coulomb and Griffith criteria

$$F = \tau - \left(\sigma_m - \frac{C^*}{tan(\varphi^0)}\right) \cdot sin(\varphi^*) \tag{6.7}$$

where F is the yield function, C^* is the mobilized cohesion, φ^* is the mobilized internal frictional angle,φ^0 is the maximal internal frictional angle, τ is the stress deviator, and σ_m is the mean stress.
Cohesion and the internal friction angle are mobilized in terms of a cohesion weakening and frictional strengthening model with dependence on the effective plastic strain $\bar{\epsilon}_p$ Hajiabdolmajid et al. [2002]. Friction and cohesion can be calculated with

Vermeer and de Borst [1984]

$$sin\phi^* = sin\phi_0 \cdot \begin{cases} \left(1+\gamma_f \cdot \frac{2\cdot\sqrt{\epsilon_f \cdot \bar{\epsilon}_p}}{\epsilon_f+\bar{\epsilon}_p}\right) & if\ \bar{\epsilon}_p < \epsilon_f \\ (1+\gamma_f) & if\ \bar{\epsilon}_p \geq \epsilon_f \end{cases} \tag{6.8}$$

$$C^*(\bar{\epsilon}_p) = c_0 \cdot \left(1-\gamma_c \cdot exp\left(-\left(\bar{\epsilon}_p/\epsilon_c\right)^2\right)\right) \tag{6.9}$$

The parameters γ_f and γ_C define portions of cohesion and internal friction angle which are mobilized and ϵ_f and ϵ_C control the hardening and weakening rates.
Plastic strain rates are given by

$$\dot{\epsilon}_{ij}^{pl} = 0 \text{ for } F < 0 \text{ or } F = 0 \text{ and } \dot{F} < 0 \tag{6.10}$$

$$\dot{\epsilon}_{ij}^{pl} = \lambda^p \frac{\partial q}{\partial \sigma_{ij}} \text{ for } F = 0 \text{ and } \dot{F} = 0. \tag{6.11}$$

with λ^p as plastic multiplier and q as flow rule.
Effective plastic strain $\bar{\epsilon}_p$ then follows:

$$\bar{\epsilon}_p = \sqrt{\frac{2}{3}\dot{\epsilon_{pl}}^T \cdot M \cdot \dot{\epsilon_{pl}}} \tag{6.12}$$

where M is a weighting matrix Abbo [1997].
We use non-associated plastic flow rules Vermeer and de Borst [1984]

$$q = \tau - \sigma_m \cdot sin(\psi^*) \tag{6.13}$$

where ψ^* is the mobilized dilatancy angle Vermeer and de Borst [1984].
The Gassmann equations Gassmann [1951] describe changes in poro-elastic properties due to fluid saturation and solid phase bulk moduli change using Reuss [1929] and Voigt [1989].
The water-gas mixture bulk modulus is calculated as dependent on the fluid saturation S_w and the bulk moduli of water K_w and air K_g

$$K_f = S_w {K_w}^{-1} + (1-S_w){K_g}^{-1} \tag{6.14}$$

From the theory of linear poroelasticity, the full strain rate tensor is

$$\dot{\epsilon}_{ij} = \dot{\epsilon}_{ij}^{el} + \dot{\epsilon}_{ij}^{pl} \tag{6.15}$$

where $\dot{\epsilon}_{ij}^{el}$ is the poroelastic strain rate tensor. The poroelastic stress tensor is given by

$$\sigma_{ij} = 2G\epsilon_{ij} + \frac{\nu}{1+\nu}\sigma_{kk}\delta_{ij} - \frac{3(\nu_{undr}-\nu)}{B(1+\nu)(1+\nu_{undr})}p\delta_{ij} \tag{6.16}$$

where B is the Skempton coefficient, G is the shear modulus and ν is Poisson's ratio for drained and undrained casesRice and Cleary [1976].
The damage operator D defines degradation of elastic properties (Kachanov [1958], Chaboche [1987]).

$$E^d = (1-D)E^0 \tag{6.17}$$

where E is the elastic tangent operator in the damaged E^d and undamaged state E^0. In this model it is included as a linear function of the effective plastic strain using the concept of effective stress Xian-lun et al. [2011].

$$D = \frac{\bar{\epsilon}_p - \epsilon_{SD}}{\epsilon_D} \text{ if } \bar{\epsilon}_p \geq \epsilon_{SD} \tag{6.18}$$

where ϵ_{SD} is a starting value, and ϵ_D controls the rate of damage growth. In this concept the damaged stress σ^D can be derived from an undamaged state σ^0 by applying the damage operator to the stress Zhang and Cai [2010].

$$\sigma^D = (1 - D)\sigma^0 \tag{6.19}$$

6.2.2 Two phase flow

Fluid flow is considered as an isothermal water-gas immiscible mixture with no phase transition and is modeled using Richards approximation by assuming the air to be infinitely mobile and setting the air pressure as zero reference (Richards [1931]).
The Darcy velocity in a multiphase environment can be generalized for any phase $\alpha = w, a$

$$v_\alpha = \frac{-k_\alpha k_0}{\mu_\alpha} \nabla P_\alpha \tag{6.20}$$

where k_0 is the intrinsic permeability of the rock, μ_α is phase viscosity, k_α is phase permeability and P is phase pressure. Phase permeability varies between 0 and 1, and is linked to saturation S using the vanGenuchten relationships that show very good agreement with experimental data for mixtures of water and air (Cropper et al. [2011],vanGenuchten [1980]).

$$\begin{aligned} k_w &= \sqrt{S_w}\left(1 - \left(1 - S_w^{\frac{1}{m}}\right)^m\right)^2 \\ k_a &= (1 - S_w)^2 \cdot \left(1 - S_w^{\frac{2+3m}{m}}\right) \end{aligned} \tag{6.21}$$

Water pressure and water saturation are primary variables, so air pressure can be described with capillary pressure P_c vanGenuchten [1980]:

$$P_c = P_a - P_w = (S_w^m - 1)^{-n} \cdot P_r \tag{6.22}$$

The variable n is an experimentally determined parameter that is usually around 3, from which the parameter m can be determined using $m = 1 - \frac{1}{n}$. The parameter P_r is a scaling factor for capillary pressure, which is typically chosen so that $P_c/P_r \approx 10$ Cropper et al. [2011]. In the context of water intrusion in an unsaturated regime, the air reservoir can be assumed to be infinite so air pressure is the zero reference Richards [1931]. With $P_a = 0$ and, followed by that, $P_c = -P_w$ Richards equation is maintained.

$$\frac{\partial P_w}{\partial t} = \frac{1}{\phi\left(S_w \cdot c_w + \frac{\partial S_w}{\partial P_w}\right)} \nabla\left(\frac{k_w k_0}{\mu_w} \nabla P_w\right) \tag{6.23}$$

E	ν_{undr}	ϕ_0	γ_f	ϵ_f	C_0	γ_C	ϵ_C	ϵ_D	ϵ_{SD}
27.5GPa	0.10	30°	1.16	0.035	20MPa	0.75	0.009	0.6	0.0

Table 6.1: Rock properties used in our numerical simulation. Values chosen based on Hajiabdolmajid et al. [2002].Stanchits et al. [2011],Vermeer and de Borst [1984], Mayr et al. [2011].Backers [2004].

ϕ_{res}	ϕ_{in}	a	k_{in}	c
0.085	0.095	$-8 \cdot 10^{-9}$	$3.5 \cdot 10^{-16}\mathrm{m}^2$	4.0

Table 6.2: Rock properties for fluid interaction used in our numerical simulation. Values chosen based on Rutqvist et al. [2002],Stanchits et al. [2011], Mayr et al. [2011].Backers [2004].

6.3 Numerical model

We numerically implemented the model using a two dimensional finite difference scheme. We use a staggered grid Saenger et al. [2000], so the boundary conditions need only be applied for total stresses Cruz- Atienza and Virieux [2004], which are determined from the experimental setup Stanchits et al. [2011]. Experiments were performed using Flechtinger Sandstone, which is assumed to be isotropic. A detailed description of the physical properties of the rock samples is given in Backers [2004], Stanchits et al. [2011] and Blöcher et al. [2009]. Tables 6.1 and 6.2 present rock properties values used in our simulations. Our grid point resolution was 1mm in each direction.
Intrusion of fluid at the bottom boundary is modeled with the boundary condition:

$$p_{f,0} = p_0 + (p_{max} - p_0) \cdot \left(1 - e^{-t/T}\right) \tag{6.24}$$

where p_0 is initial fluid pressure, p_{max} is the maximum pressure achieved, and the time constant T controls the rate to attain the maximum fluid pressureMayr et al. [2011].
We use an explicit time stepping scheme with limitations on the maximum time step Virieux [1986], and the time step for the mechanical model is the lower limit. For plastic calculations we use a Runge- Kutta algorithm to determine the yield surface intersection and a return algorithm for yield surface drift as described in Sloan [1987]. For the elasto- plastic model we apply a second order finite difference approximation to achieve higher accuracy Cruz- Atienza and Virieux [2004].
We discretize the non-linear diffusion equations for fluid and air phase using explicit finite differences with standardized rules of centering.
Compressibility of pores due to pore pressure is of the same order as the compressibility of water, so we consider porosity and permeability as functions of the effective mean stress (Rutqvist et al. [2002],Carcione and Tinivella [2001]) using:

$$\begin{aligned} \phi &= \phi_{res} + (\phi_{in} - \phi_{res}) \cdot exp\left(a \cdot (\sigma_m - P)\right) \\ k &= k_{in} \cdot exp\left(c \cdot (\phi/\phi_{in} - 1)\right) \end{aligned} \tag{6.25}$$

with initial and residual values of permeability and porosity as well as two experimental constants a and c Rutqvist et al. [2002]. Constants and initial values can be derived from experiments. Additionally, we increase intrinsic permeability when failure occurs by a factor of 10 as in sandstone intrinsic permeability is already high in comparison to granite (cf. Miller [2014], Miller and Nur [2000]).
Failure in a grid cell is equivalent to generating a micro-fracture and permeability in fractures is significantly higher than in the porous matrix Mitchell and Faulkner [2008].
To compensate for neglecting pore compressibility in equation 6.23, we correct the saturation Rutqvist et al. [2002]:

$$S_w^* = S_w \cdot \frac{\phi_t}{\phi_{t+1}} \tag{6.26}$$

with t as an index for the discrete time step.

6.4 Results

6.4.1 Triaxial compression of a dry, undrained specimen to failure

In the first experimental configuration using a displacement-controlled aparatus, a confining pressure of 40MPa was applied and followed by an increasing axial load until the onset of macroscopic failure. This was followed by unloading of the specimen.
The stress strain curve for the dry loading case shows behavior typical of triaxial rock mechanics experiments. The behavior is characterized by a linear elastic response, followed by a hardening- softening phase after reaching a yield point at around 0.7 % of axial strain. A decrease in axial strain and stress accompany brittle failure (figure 6.1). Inelastic axial strain reaches a maximum value of 0.9 %, increasing with the onset of hardening (figure 6.2). Volumetric strain initially increases (associated with compaction of the pore space), and reaches a maximum during hardening. This is followed by a substantial decrease until the onset of brittle failure at maximum dilatancy (negative volumetric strain) of -1.15 % (figure 6.3). We achieve excellent agreement between experimental and numerical results throughout the entire load-unload response; the stress - strain response curve, the inelastic stress response, and the volumetric deformation.
In the experiment, volumetric strain was measured with two separate devices that showed differing responses in the later stages of the loading process. This indicates an anisotropy that we do not yet consider at this stage in our numerical model. Our model does, however, capture the differential stress drop at failure, with a similar amplitudes (figure 6.4), and the overall behavior of the specimen from compaction to dilatancy. The origin and propagation of the macroscopic fracture coincides in both the simulation and the laboratory experiment (cf. figures 6.5 and Stanchits et al. [2011]).

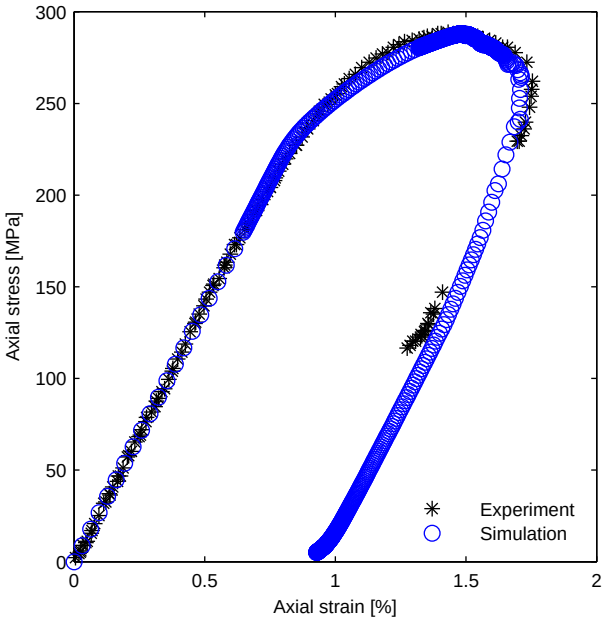

Figure 6.1: Stress- Strain response curve. Characteristic Stress- Strain curve during loading of the dry specimen in experiment and simulation. Linear elastic behavior is followed by hardening-softening and a very small damage region before unloading. The unloading path is similar to the loading path in the limits of measurement accuracy (experimental data from Stanchits et al. [2011]).

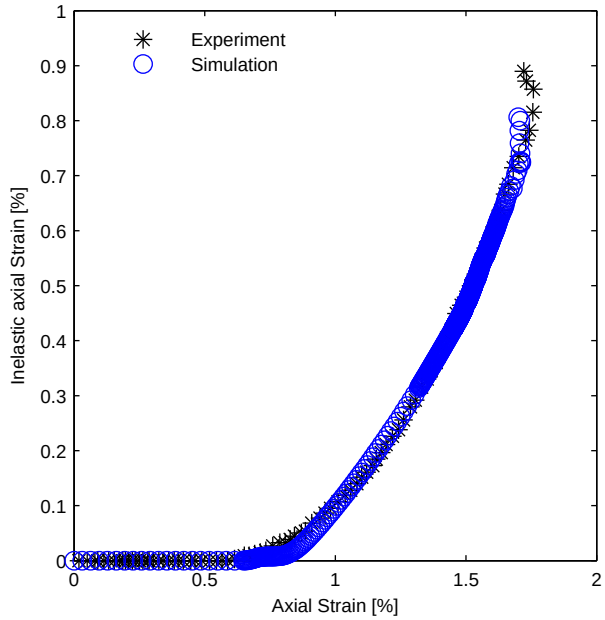

Figure 6.2: Inelastic axial stain during loading of the dry specimen in experiment and simulation. The inelastic axial stress increases rapidly during loading. It reaches the maximum value at almost 1% (experimental data from Stanchits et al. [2011]).

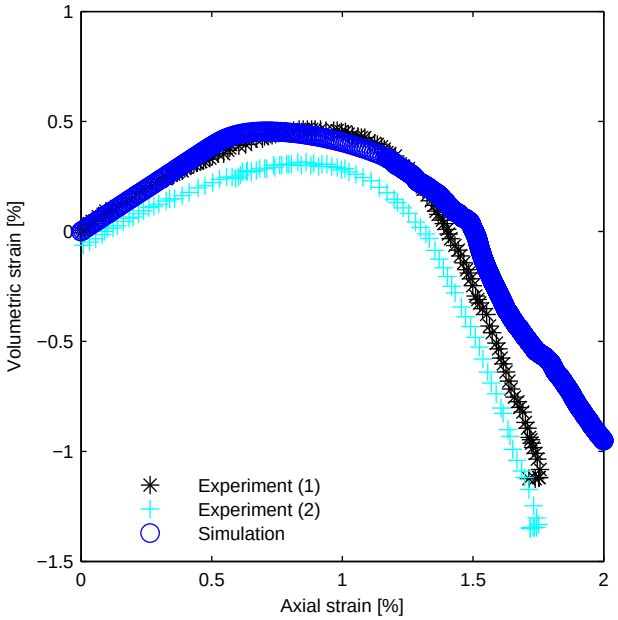

Figure 6.3: Volumetric strain versus axial strain. The volumetric strain indicates compression during the first stage of loading ($dV \geq 0$) but then rapidly show dilatant behavior. The maximum difference between both measurements is lower than 0.2%. The volumetric strain of the simulation is extrapolated from the calculated axial and horizontal dimension (experimental data from Stanchits et al. [2011]).

Acoustic emissions (AE) can not be directly obtained from the numerical results. However, we propose deviatoric strain in the model as an AE analog because deviatoric strain is a measure of shear displacement that is directly related to micro- and macrofracturing. We chose several thresholds of deviatoric strain as AEs indicators (figure 6.5 and Stanchits et al. [2011]). In the first stages of compression our numerical AE shows random behavior and is equally distributed over the whole specimen. Near macroscopic failure, we find that they localize around the ultimate failure plane similar to the experimental observations. This behavior is described in other laboratory experiments as well (e.g. Lockner [1993] and Fortin et al. [2009]). A comparison of experimental AE and values obtained from our deviatoric strain analog shows that both increase rapidly at failure (figure 6.6).
In general, discretized values of deviatoric strain show similar behavior than AEs over the whole compressive stage. A more detailed study of our numerical AE analog is the focus of another paper.

6.4.2 Fracturing of porous rock during water injection

In the second simulation, we compare our fluid rock interaction model with experimental data. In the second experimental setup, a rock specimen (sealed on top) was bi- axially loaded to an initial stress state of around 280MPa with a confinement stress of 40MPa, and then fluid was injected at the bottom with a pressure of 5MPa.

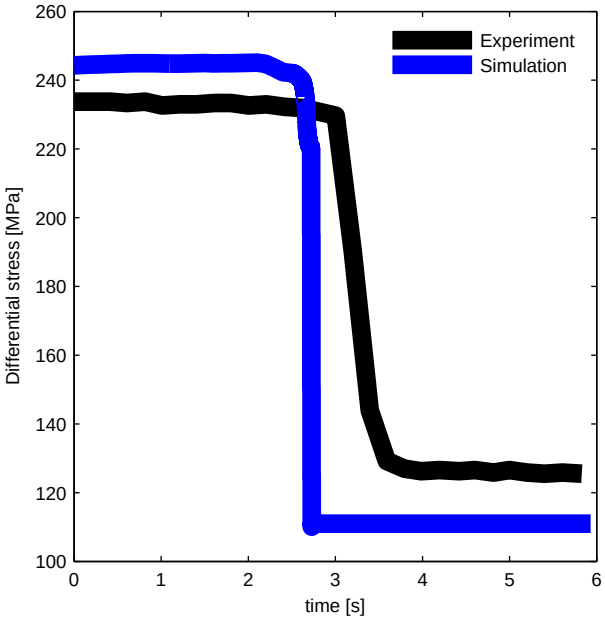

Figure 6.4: Stress drop at macroscopic failure. Change of differential stress at macroscopic failure of the specimen. The differential stress drops rapidly at macroscopic failure. Shown with unified time scale as experiment and simulation act on different time scales (experimental data from Stanchits et al. [2011]).

Upon application of the fluid pressure boundary, the axial stress decreased over the entire fluid intrusion process from its initial state of around 280MPa down to around 210MPa. The largest stress drop takes place during the first 200 seconds of the experiment (figure 6.7). In the laboratory experiment this stress drop occurs because the position of the loading piston is fixed, without reloading after fluid injection. The simulation shows a smaller stress drop when compared to the laboratory experiments, likely due to pore-elastic effects that we model but which does not capture all processes occurring in the experiment.
As in the experiment, we measure fluid pressure at top of the specimen to compare with fluid migration in the specimen, and the fluid pressure at the bottom is an applied boundary condition. The arrival of the fluid pressure front in the model is coincident with that observed, and with the correct amplitude of the fluid pressure pulse (figure 6.8).
In the laboratory experiments, the fluid pressure front can be estimated from the injected fluid volume, or by solving a linear diffusion equation that fits a diffusivity constant constrained by acoustic emission events. The diffusion front technique is widely applied in the field (Shapiro and Dinske [2009], Parotidis et al. [2005]).
In our numerical model, we obtain the fluid front directly from the solution of the fluid saturation equation (figure 6.9). The simulated fluid front compares well with laboratory measured fronts. At the top, the simulated fluid front shows a short rapid increase, which is due to boundary conditions. Also near to the end of the injection stage the simulated fluid front agrees better with the fluid front determined based

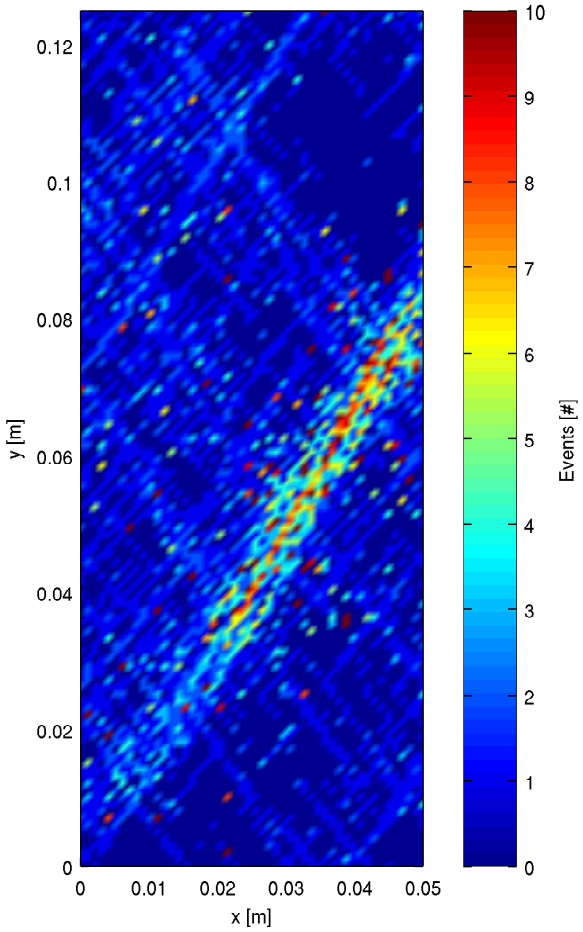

Figure 6.5: Analogons for acoustic emissions. Events which depend on deviatoric strain during loading up to the moment of macroscopic failure of the specimen. Their distribution is analogous to the deviatoric strain and is equally distributed over the specimen. Color indicates number of occurrence per grid cell. Comparison with acoustic emissions in the experiment shows same initiation point and propagation angle of the macroscopic fracture (compare Stanchits et al. [2011]).

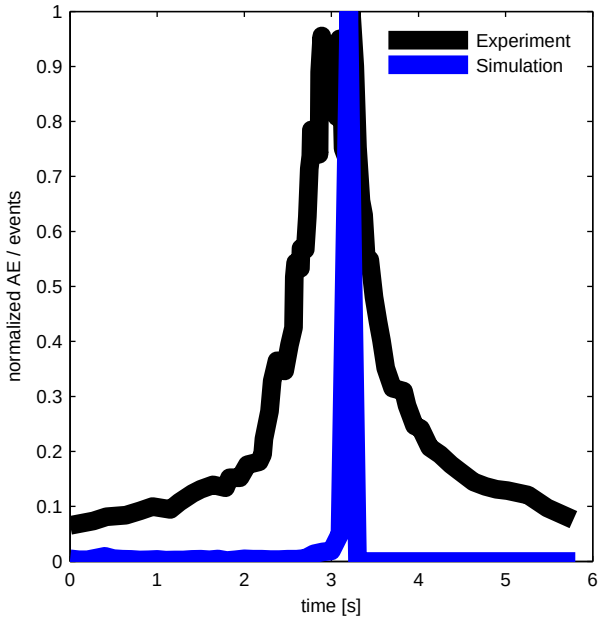

Figure 6.6: Number of acoustic emissions and analogons detected during the simulation (experimental data from Stanchits et al. [2011]), normalized to its peak value. Acoustic emissions as well as events have a clear peak at the moment of macroscopic failure during the hydraulic fracturing experiment.

on injected fluid volume than to that calculated based on observed AE.
Our simulation results show a similar spatio- temporal evolution between discretized values of the deviatoric strain the experimental fluid front (figure 6.10). The simulated fluid front, computed using the saturation equation, envelopes the discretized values of deviatoric strain in the same way as in the experiments where the fluid fronts are calculated from injected fluid volumes or via envelopes resulting from the solution to linear diffusion equations. This demonstrates that our proposed numerical AE analog is valid. Finally, few AE's are observed ahead of the fluid front in either the experiments or the simulations.

6.4.3 Failure of drained rock specimen during high pressure fluid injection

Following the completion of the first fluid injection stage (described previously), the pore pressure was reduced to 1MPa and the specimen remains fully saturated. After a certain time, fluid was injected with an increased pressure of 20MPa until the onset of macroscopic failure. Our simulation matches the flow behavior of the experiment very well for the saturated case (cf. figure 6.11).
In the experiments macroscopic failure in saturated media is characterized by a rapid increase of AE and a sudden stress drop. There are two main differences with respect to the drained macroscopic failure that are also present in our simulations.

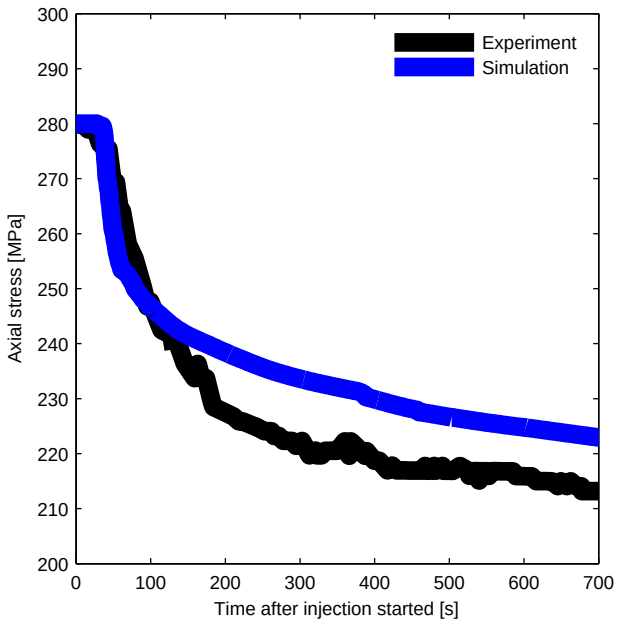

Figure 6.7: Axial stress during fluid injection. The mean axial stress decreases over the entire intrusion process from its initial state of around 280MPa down to around 210MPa. The largest stress drop takes place in the first 200 seconds of the experiment (experimental data from Stanchits et al. [2011]).

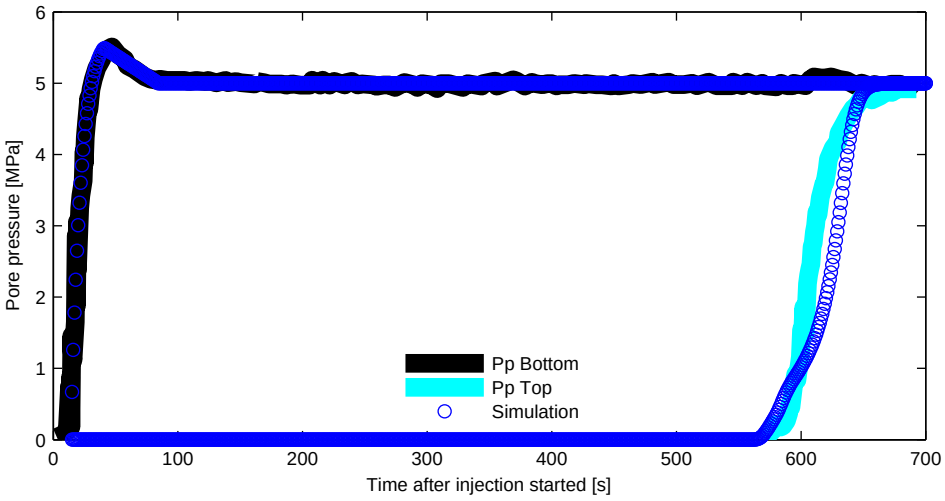

Figure 6.8: Pore pressure during injection. Applied fluid pressure at the bottom and measured fluid pressure at the top of the specimen. Fluid pressure at the bottom is fitted with a piecewise function for the boundary condition in the simulation. The fluid pressure at the top is a result of the simulation. The fluid pressure at the top is measured for the first time after 560 seconds and increases to the same value as the applied pressure at the bottom. The pressure is simulated (dashed lines) with a boundary condition at the bottom and the pressure at the top is a result of solving the pressure and saturation equation (experimental data from Stanchits et al. [2011]).

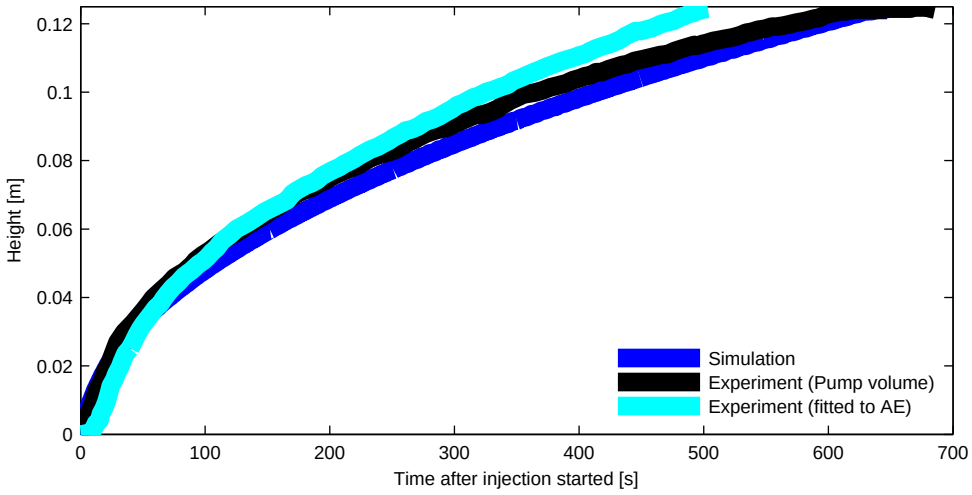

Figure 6.9: Fluid fronts from experiment and simulation. In the experiment one fluid front is estimated from the injected volume, the other front is fitted for a match with the AEs. The fluid front from the simulation is determined with the saturation equation (experimental data from Stanchits et al. [2011]).

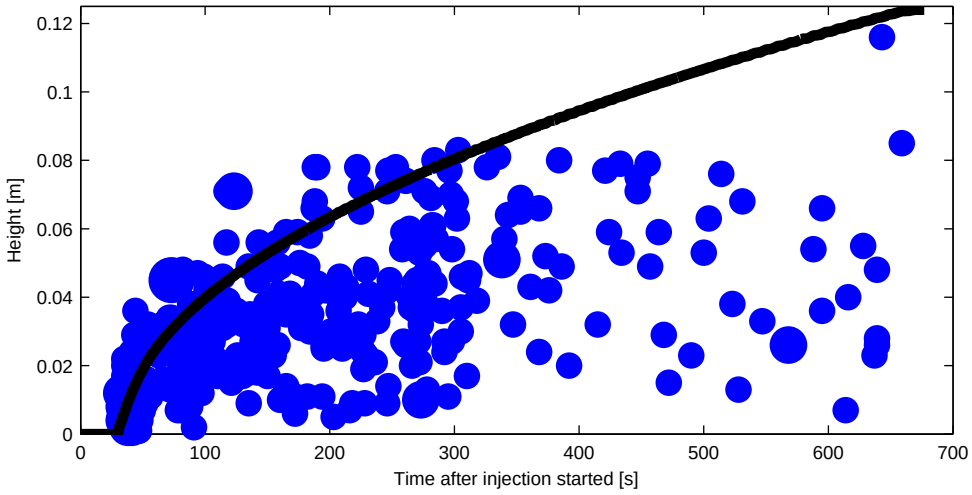

Figure 6.10: Fluid front and events. The fluid front (black line) derived from the saturation equation can be associated with a propagating cloud of events (dots) depending on the deviatoric strain. Almost all events are registered close to or below the fluid front. The diameter of the dots is proportional to the number of registered events.

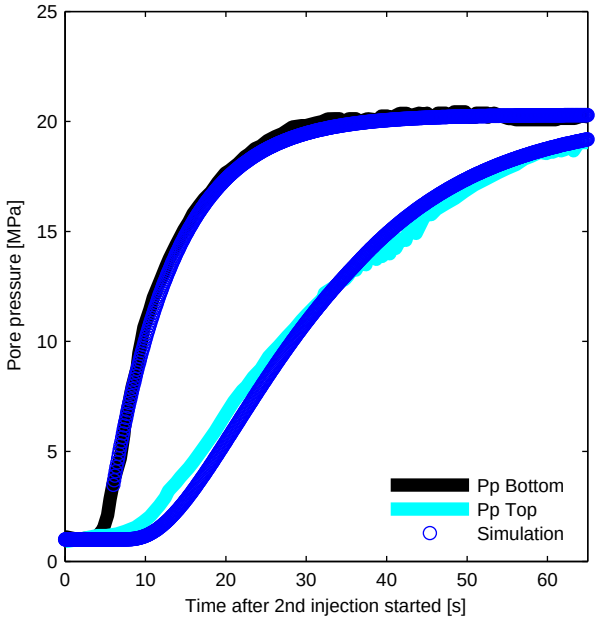

Figure 6.11: Pore pressure during hydraulic fracturing. Applied fluid pressure at the bottom and measured fluid pressure at the top during 2nd injection in the same specimen as above. The dashed line is the simulation result, solid line obtained from experimental data. The behavior is different to the injection process before because this time the fluid is introduced to a saturated specimen. Therefore a response at the top can be seen much earlier than in the prior experiment (experimental data from Stanchits et al. [2011]).

First, there is a stress drop due to fluid injection and, second, the duration of high AE activity is much longer (cf. figure 6.12). Both behaviors are present in our simulation.

6.5 Conclusions

We introduced a numerical model and compared simulation results with a suite of experiments performed on porous rock and fractured due to fluid injection. The model simulates a poroelasto-plastic rheology that includes cohesion weakening and a frictional strengthening that depends on the effective plastic strain with a mobilized dilatancy angle. This model is then coupled with a two phase fluid model. We make both qualitative and quantitative comparison to the high-precision laboratory experiments.

Three main aspects of the laboratory experiment are reproduced in the model; (1) failure under dry loading conditions; (2) Acoustic emissions during hydraulic stimulation; and (3) macroscopic failure due to injection of high pressure fluids into a prestressed rock specimen. We model different aspects of fluid-rock interaction, including stress strain behavior during drained macroscopic failure, and the initiation and propagation of macroscopic fracture. As observed in the experiments, we

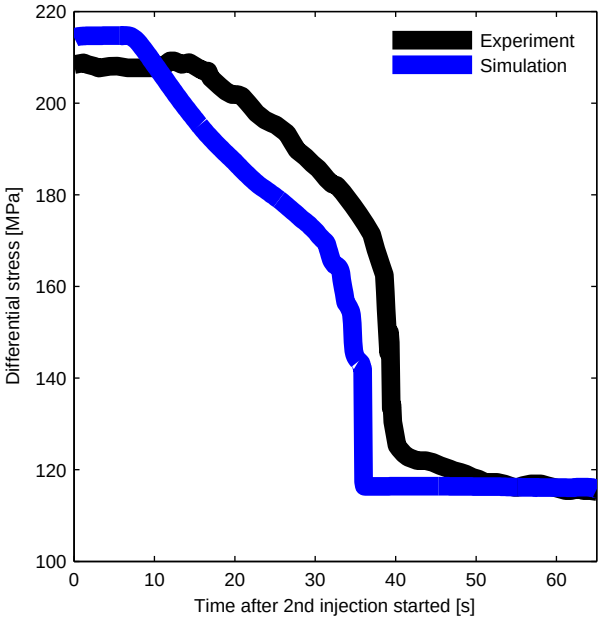

Figure 6.12: Stress drop during high pressure injection. As the fluid pressure increases the differential stress decreases. At macroscopic failure a significant stress drop in a very short time step can be observed. This stress drop is around 50MPa and phase out to a residual value. In total the stress drop is about 100MPa (experimental data from Stanchits et al. [2011]).

also observe in our simulation almost no events near the top boundary during fluid injection.

For all cases numerical experiments reproduce the experimental with a high degree of consistency. In particular, macroscopic fracture and fluid front localization rendered with our model as well as the stress- strain- response curve matches laboratory experiments very well.

Hardening, softening and damage play a crucial role in rock behavior during drained loading and as a result of hydraulic stimulation, while including two phase flow produces realistic modeling of fluid flow and pore pressure. Our results indicate that these processes are necessary to successfully model rock behavior during hydraulic stimulation.

Understanding the relationships between the fluid front and the occurrence of seismic events is essential for investigating field scale applications and experiments. At the laboratory scale, the same physics and underlying processes are in play between acoustic emissions and the fluid front, and we have shown in our simulations that deviatoric strain is a useful analog for quantifying the coupling between the fluid front the the occurrence of acoustic emissions. We will apply this methodology to field scale experiments to determine its applicability to other fluid-controlled or fluid-induced seismicity observations. The results of this investigation will be addressed in a separate study.

Typically, the fluid front is estimated using basic models with linear permeability and

a simple rheology. For example, solutions to the linear diffusion equation (Shapiro et al. [2003]) used to estimate diffusivity from the seismicity front can dramatically overestimate of the diffusivity, while significantly underestimating the fluid pressure at the front. A comparison of the fluid fronts derived from the injected fluid volume and from the propagation of acoustic emissions show several cases in where both curves diverge significantly. Taking the pressure response curves at the top of the specimens in consideration, we observe that the fluid front estimated from the injected volume correlates better with the measured pressure history. Our estimation of the fluid front using the saturation equations agrees very well with the pressure curves on both ends, as well as with the fluid front derived from injected volume. Applying our approach for cases in which the injected volume is not known, or difficult to determine, allows a more realistic estimation of the fluid front.
The experiments demonstrate that even small fluid pressures can generate fractures of different sizes in critically stressed rocks. Our model, using a complex rheology and two phase fluid flow in unsaturated porous media, reproduces very well the experimental results and provides substantial insight into the processes controlling fluid-rock interactions. Applying our model at field scale will enable more realistic scenarios for different cases in real-world applications.

Acknowledgment

We thank the German Research Foundation, Deutsche Forschungsgemeinschaft (DFG), for the financial support through the project no. MI 1237/7-1 and the VW foundation through the grant 'Extreme Events'.

Bibliography

Abbo, A. (1997). *Finite Element Algorithms for Elastoplasticity and Consolidation*. PhD thesis.

Aggelis, D., Dassios, K., Kordatos, E., and Matikas, T. (2013). Damage Accumulation in Cyclically-Loaded Glass-Ceramic Matrix Composites Monitored by Acoustic Emission. *The Scientific World Journal*, 2013.

Aggelis, D., Kordatos, E., and Matikas, T. (2011). Monitoring of metal fatigue damage using acoustic emission and thermography. *J Acoustic Emission*, 29:113–122.

Amitrano, D. (2003). Brittle-ductile transition and associated seismicity: Experimental and numerical studies and relationship with the b value. *J. Geophys. Res.*, 108(B1):2044.

Amitrano, D., Grasso, J., and Hantz, D. (1999). From diffuse to localised damage through elastic interaction. *GRL*, 26(14):2109–2112.

Backers, T. (2004). *Fracture Toughness Determination and Micromechanics of Rock Under Mode I and Mode II Loading*. PhD thesis.

Bai, M., Meng, F., Elsworth, D., Zaman, M., and Roegiers, J.-C. (1997). Numerical modeling of stress-dependent permeability. *Int. J. Rock Mech. Min. Sci. Geomech.*, 34(3-4):paper No. 020.

Baisch, S., Vörös, R., Rothert, E., Stang, H., Jung, R., and Schellschmidt, R. (2010). A numerical model for fluid injection induced seismicity at Soultz-sous-Forêts. *Int. J. Rock Mech. Min. Sci. Geomech.*, (47):405–413.

Bejan, A. (2013). Heat Transfer Through a Porous Medium. In Nield, D. and Bejan, A., editors, *Convection in Porous Media*, chapter 20. Springer, 4th edition.

Berdowski, J., Berdowska, S., and Aubry, F. (2013). Study of Properties of Expanded Graphite – Polymer Porous Composite by Acoustic Emission Method. *Arch. Metall. Mater.*, 58(4):1331–1336.

Bielski, J., Skrzypek, J., and Kuna-Ciskal, H. (2006). Implementation of a Model of Coupled Elastic-Plastic Unilateral Damage Material to Finite Element Code. *Int. J. Damage Mech.*, 15.

Biot, M. A. (1941). General Theory of Three- Dimensional Consolidation. *J. Appl. Phys.*, 12:155–164.

Blöcher, G., Zimmermann, G., and Milsch, H. (2009). Impact of Poroelastic Response of Sandstones on Geothermal Power Production. *Pure Appl. Geophys.*, 166:1107–1123.

Bobinski, J. and Tejchman, J. (2006). Modeling of strain localization in quasi-brittle materials with a coupled elasto-plastic-damage model. *J. Theor. Appl. Mech.*, 44(4):767–782.

Boominathan, R., Arumugam, V., Santulli, C., Sidarth, A., Sankar, R., and Sridhar, B. (2014). Acoustic emission characterization of the temperature effect on falling weight impact damage in carbon/epoxy laminates. *Compos. Part B- Eng.*, 560:591–598.

Bräuer, K., Kämpf, H., Strauch, G., and Weise, S. (2003). Isotopic evidence (3He/4He, of fluid-triggered intraplate seismicity. *J. Geophys. Res.*, 108(B2):2070.

Brudy, M. and Zoback, M. (1999). Drilling-induced tensile wall-fractures: implications for determination of in-situ stress orientation and magnitude. *Int. J. Rock Mech. Min. Sci. Geomech.*, 36:191–215.

Brudy, M., Zoback, M., Fuchs, K., Rummel, F., and Baumgärtner, J. (1997). Estimation of the complete stress tensor to 8 km depth in the KTB scientific drill holes: Implications for crustal strength. *J. Geophys. Res.*, 102(B8):18,453–18,475.

Burks, B. and Kumosa, M. (2014). A modal acoustic emission signal classification scheme derived from finite element simulation. *Int. J. Damage Mech.*, 23(1):43–62.

Cai, M., Kaiser, P., Morioka, H., Minami, M., Maejima, T., Tasaka, Y., and Kurose, H. (2007). FLAC/PFC coupled numerical simulation of AE in large-scale underground excavations. *Int. J. Rock Mech. Min. Sci. Geomech.*, (44):550–564.

Cappa, F., Rutqvist, J., and Yamamoto, K. (2009). Modeling crustal deformation and rupture processes related to upwelling of deep CO2-rich fluids during the 1965-1967 Matsushiro earthquake swarm in Japan. *J. Geophys. Res.*, 114(B10304).

Carcione, J. and Tinivella, U. (2001). The seismic response of overpressure: a modelling study based on laboratory, well and seismic data. *Geophys. Prospect.*, 49:523–539.

Carol, I., Rizzi, E., and Willam, K. (2001). On the formulation of anisotropic elastic degradation. I. Theory based on a pseudo-logarithmic damage tensor rate. *Int. J. Solids Struct.*, (38):491–518.

Chaboche, J. (1987). Continuum Damage Mechanics: Present State and Future Trends. *Nucl. Eng. Des.*, 105:19–31.

Chiarelli, A., Shao, J., and Hoteit, N. (2003). Modeling of elastoplastic damage behavior of a claystone. *Int. J. Plasticity*, 193:23–45.

Clauser, C. (2003). *Numerical Simulation of Reactive Flow in Hot Aquifers*. Springer, ix edition.

Clauser, C., Giese, P., Huenges, E., Kohl, T., Lehmann, H., Rybach, L., Safanda, J., Wilhelm, H., Windloff, K., and Zoth, G. (1997). The thermal regime of the crystalline continental crust: Implications from the KTB. *J. Geophys. Res.*, 102(B8):18,417–18,441.

Crisfield, M. (1991). *Non-linear Finite Element Analysis of Solids and Structures*, volume 1. John Wiley and Sons.

Cropper, S., Perfect, E., van den Berg, E., and Mayes, M. (2011). Comparison of Average and Point Capillary Pressure–Saturation Functions Determined by Steady-State Centrifugation. *Soil Science Soc. America J.*, 75(1).

Cruz- Atienza, V. and Virieux, J. (2004). Dynamic rupture simulation of non-planar faults with a finite- difference approach. *Geophys. J. Int.*, 158(3):939–954.

Dagger, M. (1997). *A fully- coupled two phase flow and rock deformation model for reservoir rock*. PhD thesis, University of Oklahoma.

Davis, R. and Selvadurai, A. (2002). *Plasticity and Geomechanics*. Camebridge University Press.

dePater, C. and Baisch, S. (2011). Geomechanical Study of Bowland Shale Seismicity. *Synthesis Report*.

Drozdov, A. (2013). The Acoustic Emission Method Application for Producing a Growing Sharp Crack and Evaluation of the Fracture Toughness of Ceramic Materials. *Strength Mater.*, 45(3):301–307.

Drozdov, A. (2014). Investigation on the Microcracking of Ceramic Materials Using the Acoustic Emission Method. *Strength Mater.*, 46(1):71–79.

Duretz, T., May, D., Gerya, T., and Tackley, P. (2011). Discretization errors and free surface stabilization in the finite difference and marker in cell method for applied geodynamics: A numerical study. *Geochem. Geophys. Geosys.*, 12(7).

ElBatanouny, M., Ziehl, P., Larosche, A., Mangual, J., Matta, F., and Nanni, A. (2014). Acoustic emission monitoring for assessment of prestressed concrete beams. *Construct. Build. Mat.*, 58:46–53.

Elfergani, H., Pullin, R., and Holford, K. (2013). Damage assessment of corrosion in prestressed concrete by acoustic emission. *Construct. Build. Mater.*, 40:925–933.

Fang, Z. and Harrison, J. (2002). Application of a local degradation model to the analysis of brittle fracture of laboratory scale rock specimens under triaxial conditions. *Int. J. Rock Mech. Min. Sci. Geomech.*, 39:459–476.

Farrelly, F., Petri, A., Pitolli, L., and Pontuale, G. (2004). Statistical properties of acoustic emission signals from metal cutting processes. *Acoust. Soc. America*, 116(981):981–986.

Fenghour, A., Wakeham, W., and Vesovic, V. (1998). The viscosity of Carbon Dioxide. *J. Phys. Chem. Ref. Data*, 27(1).

Fischer, T. and Horalek, J. (2003). Space-time distribution of earthquake swarms in the principal focal zone of the NW Bohemia/Vogtland seismoactive region: period 1985–2001 . *J. Geodyn.*, (35):125–144.

Fischer, T., Horalek, J., Hrubcova, P., Vavrycuk, V., Bräuer, K., and Kämpf, H. (2014). Intra-continental earthquake swarms in West- Bohemia and Vogtland: A review. *Tectonophysics*, (611):1–27.

Fischer, T., Horalek, J., Michalek, J., and Bouskova, A. (2010). The 2008-West Bohemia earthquake swarm in the light of the WEBNET network. *J. Seis.*, 14(4).

Fortin, J., Stanchits, S., Dresen, G., and Gueguen, Y. (2009). Acoustic emissions monitoring during inelastic deformation of porous sandstone: Comparison of three modes of deformation. *Pure Appl. Geophys.*, 166:823–841.

Fu, T., Liu, Y., Lau, K., and Leng, J. (2014). Impact source identification in a carbon fiber reinforced polymer plate by using embedded fiber optic acoustic emission sensors. *Compos. Part B- Eng.*, 66:420–429.

Galvan, B. and Miller, S. (2013). A Full GPU Simulation of Evolving Fracture Networks in a Heterogeneous Poro-Elasto-Plastic Medium with Effective-Stress-Dependent Permeability. In Yuen, D., Wang, L., Chi, X., Johnsson, L., Ge, W., and Shi, Y., editors, *GPU solutions to multi-scale problems in science and engineering*, Lecture Notes in Earth System Sciences, pages 305–319. Springer.

Gassmann, F. (1951). Über die Elastizität poroser Medien. *Vierteljahrsschrift der Naturforschenden Gesellschaft in Zürich*, (96):1–23.

Geller, R. (2011). Shake-up time for Japanese seismology. *Nature*, 472(7344):407–409.

Geopalaeratnam, V. and Shah, S. (1985). Softening response of plain concrete in direct tension. *ACI J*, 85(3):310–323.

Gerya, T., May, D., and Duretz, T. (2013). An Adaptive Staggered Grid Finite Difference Method for Modeling Geodynamic Stokes Flows with Strongly Variable Viscosity. *Geochem. Geophys. Geosys.*, 14(4).

Grassl, P. and Jirasek, M. (2006). Damage-plastic model fro concrete failure. *Int. J. Solids Struct.*, 43:7166–7196.

Hainzl, S. (2004). Seismicity patterns of earthquake swarms due to fluid intrusion and stress triggering. *Geophys. J. Int.*, (159):1090–1096.

Hainzl, S., Fischer, T., and Dahm, T. (2012). Seismicity-based estimation of the driving fluid pressure in the case of swarm activity in Western Bohemia. *Geophys. J. Int.*, 191:271–281.

Hajiabdolmajid, V., Kaiser, P., and Martin, C. (2002). Modelling brittle failure of rock. *Int. J. Rock Mech. Min. Sci. Geomech.*, 39:731–741.

Hamdi, S., Duff, A., Simon, L., Plantier, G., Sourice, A., and Mathieu, F. (2013). Acoustic emission pattern recognition approach based on Hilbert–Huang transform for structural health monitoring in polymer-composite materials. *Appl. Acoustics*, 74(5):746–757.

Häring, M., Schanz, U., Ladner, F., and Dyer, B. (2008). Characterisation of the Basel 1 enhanced geothermal system. *Geothermics*, (37):469–495.

Hazzard, J., Collins, D., Pettitt, W., and Young, P. (2002). Simulation of Unstable Fault Slip in Granite Using a Bonded- particle Model. *Pure Appl. Geophys.*, 159:221–245.

Hazzard, J. and Young, P. (2002). Moment tensors and micromechanical models. *Tectonophysics*, 356:181–197.

Hazzard, J. and Young, P. (2004). Dynamic modelling of induced seismicity. *Int. J. Rock Mech. Min. Sci. Geomech.*, 41:1365–1376.

Heinicke, J., Fischer, T., Gaupp, R., Götze, J., Koch, U., and Konietzky, H. (2009). Hydrothermal alteration as a trigger mechanism for earthquake swarms: the Vogtland/NW Beohemia region as a case study. *Geophys. J. Int.*, (178):1–13.

Heinze, T., Galvan, B., and Miller, S. (2015a). A new method to estimate occurrence and magnitude of failure events in rock deformation simulations. *submitted*.

Heinze, T., Galvan, B., and Miller, S. (2015b). Modeling porous rock fracturing induced by fluid injection - Numerical simulation and comparison with laboratory experiments. *submitted*.

Helmig, R. (1997). *Multiphase Flow and transport Processes in the Subsurface*. Springer.

Holland, A. (2011). Examination of Possibly Induced Seismicity from Hydraulic Fracturing in the Eola Field, Garvin County, Oklahoma. Technical report, Oklahoma Geological Survey.

Hu, S., Lu, J., and Xiao, F. (2013). Evaluation of concrete fracture procedure based on acoustic emission parameters. *Construct. Build. Mater.*, 47:1249–1256.

Huang, M., Jiang, L., Liaw, P., Brooks, C., Seeley, R., and Klarstrom, D. (1998). Using Acoustic Emission in Fatigue and Fracture Materials Research. *JOM*, 50(11).

Itasca consulting group, I. (2012). *FLAC Manual*.

Itturrioz, I., Lacidogna, G., and Carpinteri, A. (2013). Acoustic emission detection in concrete specimens: Experimental analysis and lattice model simulations. *Int. J. Damage Mech.*, 0(0):1–32.

Jaeger, J., Zimmerman, R., and Cook, N. (2007). *Fundamentals of Rock Mechanics*. Blackwell Publishing, 4th edition.

Kachanov, L. (1958). Rupture time under creep conditions. *Otdelenie tekhnicheskich nauk*, (8):26–31.

Karson, I. and Jirsa, J. (1969). Behaviour of concrete under compressive loadings. *J. Struct. Div.*, 95(12):2535–2563.

Kaus, B. (2010). Factors that control the angle of shear bands in geodynamic numerical models of brittle deformation. *Tectonophysics*, 484:36–47.

Kawasaki, Y., Wakuda, T., Kobarai, T., and Ohtsu, M. (2013). Corrosion mechanisms in reinforced concrete by acoustic emission. *Construct. Build. Mater.*, 48:1240–1247.

Kencanawati, N., Iizasa, S., and Shigeishi, M. (2013). Fracture process and reliability of concrete made from high grade recycled aggregate using acoustic emission technique under compression . *Mater. Struc.*, 46(96):1441–1448.

Kolditz, O., Bauer, S., Bilke, L., Böttcher, N., Delfs, J., Fischer, T., Görke, U., Kalbacher, T., Kosakowski, G., McDermott, C., Perk, C., Radu, F., Rink, K., Shao, H., Shao, H., Sun, F., Sun, Y., Singh, A., Taron, J., Walther, M., Wang, W., Watanabe, N., Wu, Y., Xie, M., Xu, W., and Zehner, B. (2012). OpenGeoSys: an open-source initiative for numerical simulation of thermo-hydro-mechanical/chemical (THM/C) processes in porous media. *Env. Earth Sc.*, 67:589–599.

Kun, F., Varga, I., Lennartz-Sassinek, S., and Main, I. (2014). Rupture Cascades in a Discrete Element Model of a Porous Sedimentary Rock. *Phys. Rev. Lett.*, 112(065501):1–5.

Kurz, J., Jahr, T., and Jentzsch, G. (2003). Geodynamic modelling of the recent stress and strain field in the Vogtland swarm earthquake area using the finite element method. *J. Geodyn.*, (35):247–258.

Latham, J., Xiang, J., Belayneh, M., Hamidreza, M., Tsang, C.-F., and Blunt, M. (2013). Modelling stress-dependent permeability in fractured rock including effects of propagating and bending fractures. *Int. J. Rock Mech. Min. Sci. Geomech.*, 57:100–112.

Lichtner, P., Hammond, G., Lu, C., Karra, S., Bisht, G., Andre, B., Mills, R., and Kumar, J. (2013). PFLOTRAN Web page. http://www.pflotran.org.

Lisjak, A., Liu, Q., Zhao, Q., Mahabadi, O., and Grasselli, G. (2013). Numerical simulation of acoustic emission in brittle rocks by two-dimensional finite-discrete element analysis. *Geophys. J. Int.*

Liu, Y., Cai, M., Yang, Z., Wu, W., and Chen, X. (2012). Study on deterioration law of rock strength parameters based on PFC simulation method.

Lockner, D. (1993). The Role of Acoustic Emission in the Study of Rock Fracture. *Int. J. Rock Mech. Min. Sci. Geomech.*, 30(7):883–899.

Lupi, M., Saenger, E., Fuchs, F., and Miller, S. (2013). Lusi mud eruption triggered by geometric focusing of seismic waves. *Nature Geosc.*, 6:642–646.

Lyakhovsky, V., Ben-Zion, Y., and Agnon, A. (1997). Distributed damage, faulting, and friction. *J. Geophy. Res.*, 102(B12):27,635–25,649.

Maillet, E., Godin, N., R'Mili, M., Reynaud, P., Fantozzi, G., and Lamon, J. (2014). Real-time evaluation of energy attenuation: A novel approach to acoustic emission analysis for damage monitoring of ceramic matrix composites. *J. Europ. Ceramic Soc.*, 24(7):1673–1679.

Marfo, A., Chen, Z., and Li, J. (2013). Acoustic emission analysis of fatigue crack growth in steel structure. *J. Civil Eng. Const. Tech.*, 4(7):239–249.

Marotti de Sciarra, F. (2012). Hardening plasticity with nonlocal strain damage. *Int. J. Plasticity*, 34:114–138.

Marzec, I. and Tejchman, J. (2012). Enhanced coupled elasto-plastic-damage models to describe concrete behavior in cyclic laboratory tests: comparison and improvement. *Arch. Mech.*, 64(3):227–259.

Matthäi, S., Mezentsev, A., and Belayneh, M. (2007). Finite element-node-centered finite-volume two-phase-flow experiments with fractured rock represented by unstructured hybrid-element meshes. *SPE reservoir evaluation / engineering*, 10(611):740–756.

Mayr, S., Stanchits, S., Langenbruch, C., Dresen, G., and Shapiro, S. (2011). Acoustic emission induced by pore-pressure changes in sandstone samples. *Geophysics*, 76(03):MA21–MA32.

Mazzini, A., Svensen, H., Akhamanov, G., Aloisi, G., Planke, S., Malte-Sørenssen, A., and Istadi, B. (2007). Triggering and dynamic evolution of the LUSI mud volcano, Indonesia. *Earth Planet. Sc. Lett.*, 261:375–388.

McClure, M. and Horne, R. (2010). Numerical and Analytical Modeling of Mechanisms of Induced Seismicity During Fluid Injection. *GRC Transactions*, 34.

Mei, H., Sun, Y., Zhang, L., Wang, H., and Cheng, L. (2013). Acoustic emission characterization of fracture toughness for fiber reinforced ceramic matrix composites. *Mater. Sc. Eng.: A*, 560:372–376.

Miller, S. (2014). Modeling enhanced geothermal systems and the essential nature of large-scale changes in permeability at the onset of slip. *Geofluids*, in press.

Miller, S., Collettini, C., Chiaraluce, L., Cocco, M., Barachi, M., and Kaus, B. (2004). Aftershocks driven by a highpressure CO2 source at depth. *Nature*, (424):724–727.

Miller, S. and Nur, A. (2000). Permeability as a toggle switch in £uid-controlled crustal processes. *Earth Planet. Sc. Lett.*, 183:133–146.

Min, K.-B., Rutqvist, J., Tsang, C.-F., and Jing, L. (2004). Stress-dependent permeability of fractured rock masses: a numerical study. *Int. J. Rock Mech. Min. Sci. Geomech.*, 41:1191–1210.

Mitchell, T. and Faulkner, D. (2008). Experimental measurements of permeability evolution during triaxial compression of initially intact crystalline rocks and implications for fluid flow in fault zones. *J. Geophy. Res.*, (113).

Mogi, K. (1967). Earthquakes and fractures. *Tectonophysics*, 5:35–55.

Mortazavi, A. and Molladavoodi, H. (2012). A numerical investigation of brittle rock damage model in deep underground openings. *Eng. Frac. Mech.*, 90:101–120.

Njuohvic, ., Bräu, M., Wolff-Fabris, F., Starzynski, K., and Altstädt, V. (2014). Identification of interface failure mechanisms of metallized glass fibre reinforced composites using acoustic emission analysis. *Compos. Part B- Eng.*, 66:443–452.

Oh, K. and Han, K. (2012). Fatigue life modeling of short fiber reinforced metal matrix composites using mechanical and acoustic emission responses. *J. Compos. Mater.*, 47(10):1303–1310.

Ohno, K., Uji, K., Ueno, A., and Ohtsu, M. (2014). Fracture process zone in notched concrete beam under three-point bending by acoustic emission. *Construct. Build. Mater.*

Omidi, O. and Lotfi, V. (2010). Numerical analysis of cyclically loaded concrete under large tensile strains by the plastic- damage model. *Transaction A: Civil Eng.*, 17(3):194–208.

Omidi, O., Valliappan, S., and Lotfi, V. (2013). Seismic cracking of concrete gravity dams by plastic- damage model using different damping mechanisms. *Fin. El. Anal. Des.*, 63:80–97.

Parotidis, M., Rothert, E., and Shapiro, S. (2003). Pore-pressure diffusion: A possible triggering mechanism for the earthquake swarms 2000 in Vogtland/NW-Bohemia, central Europe. *Geophys. Res. Lett.*, 30(20).

Parotidis, M., Shapiro, S., and Rothert, E. (2005). Evidence for triggering of the Vogtland swarms 2000 by pore pressure diffusion. *J. Geophy. Res.*, 110(B05S10).

Peerlings, R., de Borst, R., Brekelmans, W., and Geers, M. (1998). Gradient- enhanced damage modelling of concrete fracture. *Mech. Cohes. Frict. Mat.*, (3):323–342.

Pettitt, W., Baker, C., Young, P., Dahlström, L., and Ramqvist, G. (2002). The Assessment of Damage Around Critical Engineering Structures Using Induced Seismicity and Ultrasonic Techniques. *Pure Appl. Geophys.*, (159):179–195.

Poliakov, A., Herrmann, H., Podladchikov, Y., and Roux, S. (1994). Fractal Plastic Shear Bands. *Fractals*, 2(4).

Popov, A. and Sobolev, S. (2008). SLIM3D: A tool for three-dimensional thermomechanical modeling of lithospheric deformation with elasto-visco-plastic rheology. *Phys. Earth Planet. Inter.*, 171:55–75.

Potts, D. and Gens, A. (1985). A Critical Assessment Of Methods Of Correcting For Drift From The Yield Surface In Elasto- Plastic Finite Element Analysis. *Int. J. Numer. Anal. Meth. Geomech.*, 9:149–159.

Reuss, A. (1929). Berechnung der Fließgrenze von Mischkristallen auf Grund der Plastizitätsbedingung für Einkristalle. *Zeitschrift für Angewandte Mathematik und Mechanik*, 9(1):49–58.

Rice, J. R. and Cleary, M. P. (1976). Some basic stress diffusion solutions for fluid-saturated elastic porous media with compressible constituents. *Rev. Geophys. Space Phys.*, 14(2):227–241.

Richards, L. (1931). Capillary Conduction of liquids through porous mediums. *J. App. Phys.*, (318).

Rozhko, A. (2007). *Role of seepage forces on hydraulic fracturing and failure patterns*. PhD thesis.

Rutqvist, J., Wu, Y.-S., Tsang, C.-F., and Bodvarsson, G. (2002). A modeling approach for analysis of coupled multiphase fluid flow, heat transfer, and deformation in fractured porous rock. *Int. J. Rock Mech. Min. Sci. Geomech.*, 39:429–442.

Ruzek, B. and Horalek, J. (2013). Three-dimensional seismic velocity model of the West Bohemia/Vogtland seismoactive region. *Geophys. J. Int.*

Saenger, E., Gold, N., and Shapiro, S. (2000). Modeling the propagation of elastic waves using a modified finite-difference grid. *Wave Motion*, 31.

Safanda, J. and Cermak, V. (2000). Subsurface temperature changes due to the crustal magmatic activity - numerical simulation. *Stud. Geophys. Geod.*, (44):327–335.

Salari, M., Saeb, S., Willam, K., Patchet, S., and Carrasco, R. (2004). A coupled elastoplastic damage model for geomaterials. *Comput. Methods Appl. Mech. Engrg.*, 193:2625–2643.

Sause, M., Hamstad, M., and Horn, S. (2013). Finite element modeling of lamb wave propagation in anisotropic hybrid materials. *Composites: Part B*, 53:249–257.

Schön, J. (2011). *Physical Properties of Rocks - A Workbook*, volume 8 of *Handbook of Petroleum Exploration and Production*. Elsevier.

Shahidan, S., Pulin, R., Bunnori, N., and Holford, K. (2013). Damage classification in reinforced concrete beam by acoustic emission signal analysis. *Construct. Build. Mater.*, 45:78–86.

Shaik, A., Rahman, S., Tran, N., and Tran, T. (2011). Numerical simulation of Fluid- Rock coupling heat transfer in naturally fractured geothermal systems. *Appl. Ther. Eng.*, 31:1600–1606.

Shao, J., Chiarelli, A., and Hoteit, N. (1998). Modeling of Coupled Elastoplastic Damage in Rock Materials. *Int. J. Rock Mech. Min. Sci. Geomech.*, 35(4/5):444.

Shao, J., Jia, Y., Kondo, D., and Chiarelli, A. (2006). A coupled elastoplastic damage model for semi-brittle materials and extension to unsaturated conditions. *Mech. Mat.*, (38):218–232.

Shapiro, S. and Dinske, C. (2009). Fluid-induced seismicity: Pressure diffusion and hydraulic fracturing. *Geophys. Prosp.*, 57:301–310.

Shapiro, S., Huenges, E., and Borm, G. (1997). Estimating the crust permeability from fluid- injection- induced seismic emission at the KTB site. *Geophys. J. Int.*, (131):F15–F18.

Shapiro, S., Patzig, R., Rothert, E., and Rindschwentner, J. (2003). Triggering of Seismicity by Pore-pressure Perturbations: Permeability-related Signatures of the Phenomenon. *Pure Appl. Geophys.*, 160:1051–1066.

Sind, C., Najafabadi, M., and Salehi, M. (2012). Investigation of surface damages during sheet metal forming using acoustic emission. *J. Eng. Tribology*, 227(3):286–296.

Sinha, B., Kurt, H., Gerstle, and Tulin, L. (1964). Stress- Strain Relations for concrete under cyclic loading. *J. American Conc. Inst.*, 61(2):195–211.

Sloan, S. (1987). Substepping schemes for the numerical Integration of elastoplastic stress-strain relations. *Int. J. Numer. Analy. Met. Eng.*, 24:893–911.

Sloan, S., Abbo, A., and Sheng, D. (2001). Refined explicit integration of elastoplastic models with automatic error control. *Eng. Comp.*, 18(1/2):121–154.

Span, R. and Wagner, W. (1996). A new equation of state for Carbon Dioxide Covering the Fluid Region from the Triple- Point Temperature to 1100 K at Pressures up to 800 MPa. *J. Phys. Chem. Ref. Data*, 25(611).

Spicak, A. and Horalek, J. (2001). Possible role of fluids in the process of earthquake swarm generation in the West Bohemia/Vogtland seismoactive region. *Tectonophysics*, (336):151–161.

Stanchits, S., Mayr, S., Shapiro, S., and Dresen, G. (2011). Fracturing of porous rock induced by fluid injection. *Tectonophysics*, (503):129–145.

Tang, C. (1997). Numerical Simulation of Progressive Failure and Associated Seismicity. *Int. J. Rock Mech. Min. Sci. Geomech.*, 34(2):249–261.

Tang, C. and Kaiser, P. (1998). Numerical Simulation of Cumulative Damage and Seismic Energy Release During Brittle Rock Failure - Part I: Fundamentals. *Int. J. Rock Mech. Min. Sci. Geomech.*, 35(2):113–121.

Taqieddin, Z. (2008). *Elasto-plastic and damage modeling of reinforced concrete.* PhD thesis.

Taqieddin, Z. and Voyiadjis, G. (2009). Elastic Plastic and Damage Model for Concrete Materials: Part II: Implementation and Application to Concrete and Reinforced Concrete. *Int. J. Solids Struc.*, 1(1):187–209.

Tian, H. (2013). *Development of a Thermo-Mechanical Model for Rocks Exposed to High Temperatures during Underground Coal Gasification.* PhD thesis.

vanGenuchten, M. (1980). A closed-form Equation for Predicting the Hydraulic Conductivity of Unsaturated Soils. *Soil Science Soc. America J.*, 44(5).

Vavrycuk, V. (2002). Non-double-couple earthquakes of 1997 January inWest Bohemia, Czech Republic: evidence of tensile faulting. *Geophys. J. Int.*, (149):364–373.

Vavrycuk, V. (2011). Principal earthquakes: Theory and observations from the 2008 West Bohemia swarm. *Earth Planet. Sc. Lett.*, (305):290–296.

Vermeer, P. and de Borst, R. (1984). Non-associated Plasticity For Soils, Concrete and Rock. *Heron*, 29(37).

Virieux, J. (1986). P-SV wave propagation in heterogeneous media: Velocity- stress finite difference method. *Geophysics*, (51).

Voigt, W. (1989). Ueber die Beziehung zwischen den beiden Elasticitätsconstanten isotroper Körper. *Annalen der Physik*, 274(12):573–587.

von Terzaghi, K. (1936). The shearing resistance of saturated soils and the angle between the planes of shear. *First Int. Conf. Soil Mech.*, 1:54–56.

Voyiadjis, G. and Taqieddin, Z. (2009). Elastic Plastic and Damage Model for Concrete Materials: Part I - Theoretical Formulation . *Int. J. Solids Struc.*, 1(1):31–59.

Wang, S., Sloan, S., Sheng, D., and Tang, C. (2012). Numerical analysis of the failure process around a circular opening in rock. *Comp. Geotech.*, 39:8–16.

Wawersik, W. and Fairhurst, C. (1970). A study of brittle rock fracture in laboratory compression experiments. *Int. J. Rock Mech. Min. Sci. Geomech.*, 7:561–575.

Weinlich, F., Bräuer, K., Kämpf, H., Strauch, G., Tesar, J., and Weise, S. (1999). An active subcontinental mantle volatile system in the western Eger rift, Central Europe: Gas flux, isotopic (He, C, and N) and compositional fingerprints. *Geochimica et Cosmochimica Acta*, 63(21):3653–3671.

Weise, S., Bräuer, K., Kämpf, H., Strauch, G., and Koch, U. (2001). Transport of mantle volatiles through the crust traced by seismically released fluids: a natural experiment in the earthquake swarm area Vogtland/NW Bohemia, Central Europe. *Tectonophysics*, (336):137–150.

Wu, J., Li, Y., and Faria, R. (2006). An energy release rate-based plastic-damage model for concrete. *Int. J. Solids Struc.*, 43:583–612.

Xian-lun, L., Qian, S., En-guang, H., Ze-qi, Z., and Yu, Z. (2011). Study of surrounding rock damage induced by tunnel boring machine driving tunnel at West Route of South to North Water Transfer Project. *Rock Soil Mech.*, 32(11).

Xie, N., Zhu, Q., Xu, L., and Shao, J. (2011). A micromechanics-based elastoplastic damage model for quasi-brittle rocks. *Comp. Geotech.*, 38(8):970–977.

Yamashita, T. (1998). Simulation of seismicity due to fluid migration in a fault zone. *Geophys. J. Int.*, (132):674–686.

Yonezu, A. and Chen, X. (2014). Micro-scale damage characterization in porous ceramics by an acoustic emission technique. *Ceramics Int.*, 40(7):9859–9866.

Zang, A., Wagner, C., and Dresen, G. (1996). Acoustic emission, microstructure, and damage model of dry and wet sandstone stressed to failure. *J. Geophy. Res.*, 101(B8):17,507–17,521.

Zhang, W. and Cai, Y. (2010). *Continuum Damage Mechanics and Numerical Applications*. Advanced Topics in Science and Technology in China. Springer.

Zhu, W., Zhao, X., Kang, Y., Wei, C., and Tian, J. (2010). Numerical simulation of acoustic emission activities of concrete. *Mat. Struc.*, 43:633–650.

Zimmerman, R. (1991). *Compressibility of sandstones*, volume 29 of *Developments in petroleum science*. Elsevier.

Acknowledgments

It is a pleasure to express my gratitude to those who have contributed to the completion of this thesis.
First of all, I am very much thankfull to Professor Doctor Stephen A. Miller for his guidance and support through out the project. I also appreciate Professor Doctor Nikolaus Froitzheim willigness to join the committee and his second opinion on this dissertation. Many thanks are given to the remaining members of the examining board, Professor Doctor Andreas Kemna for encouragment during the project and Assistant Professor Doctor Elisabeth Soergel, for her willingness to join the committee.
I further thank all colleagues and students I had the pleasure to work with at the Geodynamics group in Bonn, especially Dr. Boris Galvan for his helpfull comments, Dr. Andreas Dreist for technical support as well as Dr. Shiva Pudasaini, Florian Fuchs, Sahar Hamidi, Cristian Farias and Gunnar Jansen for a great time at work.